



HAL
open science

Conception, modélisation et réalisation de composants inductifs intégrés pour alimentations de faible puissance et microsystemes

Philippe Artillan

► **To cite this version:**

Philippe Artillan. Conception, modélisation et réalisation de composants inductifs intégrés pour alimentations de faible puissance et microsystemes. Micro et nanotechnologies/Microélectronique. INSA de Toulouse, 2008. Français. NNT: . tel-00356385

HAL Id: tel-00356385

<https://theses.hal.science/tel-00356385v1>

Submitted on 27 Jan 2009

HAL is a multi-disciplinary open access archive for the deposit and dissemination of scientific research documents, whether they are published or not. The documents may come from teaching and research institutions in France or abroad, or from public or private research centers.

L'archive ouverte pluridisciplinaire **HAL**, est destinée au dépôt et à la diffusion de documents scientifiques de niveau recherche, publiés ou non, émanant des établissements d'enseignement et de recherche français ou étrangers, des laboratoires publics ou privés.



THÈSE

En vue de l'obtention du

DOCTORAT DE L'UNIVERSITÉ DE TOULOUSE

Délivré par *l'Université de Toulouse - Institut National des Sciences Appliquées (INSA) de Toulouse*
Discipline ou spécialité : *Microélectronique*

Présentée et soutenue par *Philippe Artillan*
Le *27 novembre 2008*

Titre :

*Design, modelization and realization of integrated inductive components
for low power supplies and microsystems*

*Conception, modélisation et réalisation de composants inductifs intégrés pour
alimentations de faible puissance et microsystèmes*

JURY

Pr Jean-Marie Dilhac (Président)
Pr Jean-Pierre Kéradec (Rapporteur)
Pr Pierre Merle (Rapporteur)
Pr Sigmond Singer (Rapporteur)
Pr José Milan (Examineur)

Ecole doctorale : *GEET*
Unité de recherche : *LAAS-CNRS*
Directeur(s) de Thèse : *Pr Corinne Alonso, Dr Bruno Estibals*
Rapporteurs : *Pr Jean-Pierre Kéradec, Pr Pierre Merle et Pr Sigmond Singer*

AUTHOR: Philippe ARTILLAN

TITLE: Design, modelization and realization of integrated inductive components for low power supplies and microsystems

DIRECTORS: Corinne Alonso and Bruno Estibals

PLACE AND DEFENSE DATE: Toulouse, November, 27th, 2008

ABSTRACT:

Full integration of energy conversion devices for compact power supply circuits is still encountering strong technological locks, especially to integrate passive inductive and capacitive components. The increasing working frequency of those devices, which already reaches 1 Megahertz, would enable the size reduction of passive components and then their integration. Nevertheless, losses, which highly depend on frequency and technology, may complicate or even stop this increase.

The objective of this thesis is the systematic study of integrated inductors structures through the developing of precise modeling and simulating methods on the frequency range from 0Hz to 1GHz. First, an analytic model based on PEEC (Partial Element Equivalent Circuit) method has been developed. This modeling approach has been adapted to the studied components: rotational symmetry, not negligible section conductors, inhomogeneous media, etc... The final model splits the physical study of the component into two steps: electromagnetic computations on subparts of the set (partial elements) and global frequency response calculus with the equivalent electrical models of the subparts. A full process for the technological realization of inductive components has also been achieved in order to experimentally verify the modeling. The improvement of design resolution and increase of copper electroplating thickness, as planarization of conductor levels with SU8 resin have been specifically studied. Those overhangs have permitted the realization of multilevel and multiconductor inductors which present good features at high frequency. Finally, the characterization of prototypes at low frequency has been enabled by the realization of an impedance measurement bench we developed for the range from 40Hz to 110MHz and high frequency characterizations have been performed with a network analyzer. This work has been completed by the development of a very fast computing analytical model for the calculus of the magnetic field in integrated inductors. This method has been used to find the repartition of the magnetic field generated by integrated planar magnetic actuators excited by a DC current for a microsystems and microfluidics application.

KEYWORDS: Integration, Inductor, Analytical model, PEEC, Electromagnetic FEM simulation, Electroplating, SU8, Impedance analyzer.

DISCIPLINE: Electrical Engineering

LABORATORY - ADDRESS: LAAS-CNRS, 7 av. Du Colonel Roche, 31077, Toulouse, France

AUTEUR: Philippe ARTILLAN

TITRE: Conception, modélisation et réalisation de composants inductifs intégrés pour alimentations de faible puissance et microsystèmes

DIRECTEURS: Corinne Alonso et Bruno Estibals

DATE ET LIEU DE SOUTENANCE: Toulouse, le 27 novembre 2008

RESUME:

L'intégration complète des dispositifs de conversion d'énergie destinés à créer des circuits d'alimentation compacts se heurte encore aujourd'hui à des contraintes technologiques fortes sur l'intégration des composants passifs inductifs et capacitifs. La fréquence de fonctionnement de ces dispositifs, d'ores et déjà de l'ordre du MHz, en augmentant pourrait réduire la taille de ces composants passifs et donc permettre leur intégration. Cependant, les pertes fortement liées à la fréquence et à la technologie, freinent encore cette augmentation.

Cette thèse a pour objectif l'étude systématique de structures d'inductances intégrées à travers le développement d'une modélisation accompagnée de simulations précises pour le développement d'une méthodologie de simulation valable sur la plage de fréquence de 0Hz à 1GHz. Pour cela, un modèle analytique basé sur la méthode PEEC (Partial Element Equivalent Circuit) a d'abord été développé. Ce type de modèle a du être adapté aux topologies des composants étudiés : symétrie cylindrique, conducteurs de section non négligeable, milieux non homogènes... Ce modèle décompose l'étude du composant en deux étapes : calculs électromagnétiques menés sur des sous-parties du composant (éléments partiels) et calcul de la réponse fréquentielle globale à partir de modèles électriques des éléments partiels. Un procédé complet de réalisation technologique des composants inductifs a également été mis au point en parallèle afin de valider expérimentalement la modélisation. L'amélioration de la résolution des motifs et l'augmentation de l'épaisseur des dépôts lors des étapes de croissance électrolytique du cuivre, ainsi que la planarisation des niveaux de conducteurs avec de la résine SU8 ont fait l'objet d'études spécifiques. Ces avancées ont permis la réalisation de selfs multibrin et multiniveau qui présentent des caractéristiques électriques intéressantes en haute fréquence. Enfin, la caractérisation des prototypes en basse fréquence a été rendue possible par la mise en œuvre d'un banc de mesure d'impédance pour la gamme de fréquence de 40 Hz à 110MHz et des caractérisations en haute fréquence effectuées à l'aide d'un analyseur de réseau. Ces travaux ont été complétés par la mise au point d'une méthode analytique de calcul du champ magnétique. Les calculs permettent de prédire la répartition du champ magnétique généré par des actionneurs magnétiques planaires intégrés excités en courant continu.

KEYWORDS: Integration, Inductance, Modèle analytique, PEEC, Simulation électromagnétique FEM, Croissance électrolytique, SU8, Analyseur d'impédance.

DISCIPLINE: Génie électrique

LABORATORY - ADDRESS: LAAS-CNRS, 7 av. Du Colonel Roche, 31077, Toulouse, France

Acknowledgments

The cover page may have only one author, but both this dissertation and the author himself have benefited of the contributions of many over the years.

Foremost, I thank the successive heads of the LAAS-CNRS¹, Malik Ghallab and Raja Chatila, who welcomed me during those three years of research.

The support and guidance of my advisors, Corinne Alonso and Bruno Estibals, has been an integral part of my experience at LAAS-CNRS. I especially want to acknowledge their constant will to provide me the best scientific and human environment.

I am also very grateful to the people I worked with, who have been very pleasant colleagues to me, Amine Benazzi, Magali Brunet, Christophe Escriba, David Jugieu, Alain Salles and I especially thank the “trainees” who helped me so much Jean Abboud, Vincent Delavergne and Marcos Orellana.

Thanks to Damienne Bajon, Hervé Aubert and Pierre Bidan for teaching great courses, respectively in RF electromagnetic and power converters modeling. I am also grateful for the kind support of many particularly skilled people: thanks to Denis Arzelier, Carine Jauberthie-Salsmann, Gérard Montseny and Joan Sola for their help in mathematics, to Vincent Mahout, Hikmat Hachkar, David Peyrou and Mokhtar Gharbi for giving me useful programming hints, to Thierry Parra, Christophe Viallon and Etienne Sicard for their advices concerning electromagnetic problems and to Henri Tranduc for sharing his great insight of electric measurement techniques.

I feel glad to have the opportunity to thank the technical and administrative staff whose outstanding devotion and competence make working with them a real pleasure: Nicolas Mauran,

¹ LAAS-CNRS : Laboratoire d'Analyse et d'Architecture des Systèmes – Centre National de la Recherche Scientifique. 7, avenue du Colonel Roche - 31077 Toulouse cedex 4 - France.

Sandrine Assie-Souleille, Laurent Bary and Alexandre Rumeau for characterizations, David Bourrier, David Colin, Monique Dilhan, Laurent Mazenc, Sébastien Pinaud, Ludovic Salvagnac and Laurent Bouscayrol for clean room process, Marie-Dominique Cabane, Julien Libourel for system administration, Anne Bergez, Arlette Evrard, Emilie Marchand, and Michèle Powell for documentation, Christian Berty and the Daurats for edition and “our beloved secretaries” Cathy Courret, Claude Laffore , Isabelle Nohlier and Michèle Plana.

During those three years, I also had the chance to work at INSAT² as a « moniteur » with interesting teachers Jean-Marie Dorkel, Patrick Tounsi, Jean-Marie Dilhac, Jean-Yves Fourniols, Martin Aimé, Thierry Rocacher, Pascal Acco, Ludovic Ménager, Michel Bonnet, Pascal Gérard. Thanks for a wonderful and fulfilling experience. I have learned a great deal from all of you and enjoyed your friendship.

My stay in LAAS-CNRS was enhanced by many colleagues. I am grateful to Pierre Aloïsi, Sylvain Bonhomme, Cédric Cabal, Angel Cid-Pastor, Youssef Elbasri, Hicham Kotb, Stéphane Petibon, Jaume Roig-Guitar, Lionel Séguier, Adan Simon for their pleasant friendship.

And my fondest gratitude goes to my source of greatest support, my family and my friends.



² INSAT : Institut National des Sciences Appliquées de Toulouse. 135, avenue de Rangueil - 31077 Toulouse cedex 4 – France.

To my father

“A peine a-t-on commencé à s'instruire un peu
que la mort arrive avant qu'on ait de l'expérience”

Micromégas. Voltaire

Table of contents

List of symbols	1
Introduction	3
Chapter 1 Integrated inductive components and applications.....	5
1 - Power supplies in electronic systems	5
A - Evolution of power supply demand	5
B - Evolution of power supplies structures	7
a - Linear regulator power supplies	7
b - Switching mode power supplies.....	7
c - Comparison between linear regulation and switching mode power supplies	8
C - Constitution of switching mode power supplies	9
2 - Functional approach of inductors and transformers	10
A - Definition of the ideal inductor.....	10
B - Definition of the ideal transformer	12
3 - Integrated inductive components and associated models.....	13
A - Technological improvements in inductors integration	13
B - Spiral inductive components modeling and simulation tools	17
a - Analytical models.....	17
b - Simulation with electromagnetic solvers	20
<i>Classes of electromagnetic devices and problems.....</i>	<i>20</i>
<i>Specific features to software tools.....</i>	<i>21</i>
4 - Conclusion / Contribution of this thesis	23
Chapter 2 Physical phenomena in integrated inductors and associated models	25

1 - Introduction.....	25
2 - Preamble	26
3 - One-port models.....	28
A - Serial resistance	28
B - Leakage inductance.....	28
C - RLC lumped model	29
D - Skin and proximity effects.....	30
E - Eddy currents	32
F - Hysteresis losses.....	33
4 - Two-port model	34
5 - Conclusion	36
Chapter 3 Circular spiral inductors PEEC modelization and FEM simulation.....	37
1 - Introduction.....	37
2 - SPIRALC approach for circular spiral inductors: cylindrical PEEC + quasistatic FEM simulations or analytic formulas	38
A - Fundamentals and hypotheses	38
a - Maxwell's equations	38
b - Magnetic and electric potentials.....	39
<i>Magnetic vector potential.....</i>	<i>39</i>
<i>Electric scalar potential.....</i>	<i>39</i>
c - Solving vector and scalar potentials	40
<i>Definition of Green's functions</i>	<i>40</i>
<i>Use of Green's functions</i>	<i>41</i>
d - General hypotheses and domain of application of the model.....	42
<i>Concentric rings approximation.....</i>	<i>42</i>
<i>Negligible propagation time</i>	<i>42</i>
B - Magnetic, quasi-static approach	43
a - Hypotheses over the current density	43
<i>Azimuthal current density.....</i>	<i>43</i>
<i>Low frequency approximation</i>	<i>44</i>
b - Magnetostatic general formulation	44
c - Volume discretizing and equivalent impedance definition	44

d - Properties and identifications	46
<i>Impedance matrix identification</i>	46
<i>Admittance matrix</i>	47
C - Electric, quasi-static approach	47
a - Charge density	47
<i>Surface charge density hypothesis</i>	47
b - Electrostatic general formulation.....	48
c - Surface discretizing and equivalent capacitance definition	49
D - Linear circuit model	51
a - Incidence matrices definition	51
<i>Dipoles to nodes (D2N)</i>	51
<i>Panels to nodes (P2N)</i>	51
<i>Terminals to nodes (T2N)</i>	51
b - Linear circuit representation	52
E - Partial elements calculus by analytical method	53
a - Resistance	54
b - Inductance	55
<i>Self inductance</i>	56
<i>Mutual inductance</i>	56
<i>Lyle's method for close conductors</i>	59
c - Capacitance	60
<i>Capacitances from the potential coefficient matrix P</i>	60
<i>Lateral capacitance formula</i>	60
<i>Vertical face-to-face capacitance formula</i>	61
F - Partial elements calculus by FEA method	62
a - Admittance matrix computation	62
b - Capacitance matrix computation	64
3 - The software tool: SPIRALC	67
A - The environment software: Matlab and Comsol Multiphysics.....	67
B - Presentation of the graphical interface	67
4 - Inductor simulation with finite element method.....	71
A - Evaluated FEM solvers	72

B - Preliminary simulations: air box dimensioning and ground ring influence	74
a - Air box dimensioning problem	74
b - The influence of a ground ring	76
C - Simulation of the impedance frequency response of an inductor prototype.....	77
a - Presentation of the simulated component.....	77
b - Computation of impedance frequency response with both quasistatic and full wave solvers	77
c - Comparison between simulated and analytical results	79
5 - Conclusion	83
Chapter 4 Realizations and characterizations	85
1 - Introduction.....	85
2 - Developed processes for integrated inductive components	85
3 - Inductor prototypes	91
4 - Characterization of passive components.....	94
A - Low frequency measurement	94
a - The auto balancing bridge measurement method	95
b - Probe station measurements	96
c - Bonded components.....	97
d - Test fixture compensation.....	97
e - Accuracy evaluation.....	98
B - High frequency measurement.....	101
C - Comparison between measurement methods.....	103
D - Experimental validation of theoretical study.....	104
5 - Conclusion	106
Chapter 5 Applications and perspectives	107
1 - Introduction.....	107
2 - Multiconductor	107
3 - Paramagnetic microbeads actuator	109
A - Magnetic actuators for microbeads handling in microfluidics devices	109
B - Magnetic field calculus in a spiral inductor actuator	111
a - Description of the coil.....	112

b - Expression of the magnetic field generated by a single segment in the coordinate system \mathfrak{R}'	112
c - Application of the method for changing coordinate systems to the evaluation of the total magnetic field.	115
d - Comparison of the computed magnetic fields using the analytic calculation and the finite element method	116
C - Prototypes of microfluidics device with magnetic actuator and perspectives	118
4 - Conclusion	119
Conclusion	121
References	123
Appendix - Real transformer.....	131



List of symbols

E	Electric field
B	Magnetic flux density (also called magnetic field)
H	Magnetizing field
J_c	Conduction current density
J_d	Displacement current density
J	Total current density
D	Electric displacement field
ρ	Volume charge density
ρ_s	Surface charge density
ϵ	Electric permittivity
μ	Magnetic permeability
σ	Electric conductivity
∇	Differential operator Nabla
∇f	Gradient of f
$\nabla \cdot \mathbf{a}$	Divergence of a
$\nabla \times \mathbf{a}$	Rotational of a
∇^2	Laplace operator
s	Generalized Laplace variable
Re[z]	Real part of complex variable z
Im[z]	Imaginary part of complex variable z
Φ	Electric scalar potential
A	Magnetic vector potential

V	Volume domain of the space ($V \subset \mathbb{R}^3$)
S	Surface domain of the space ($V \subset \mathbb{R}^3$)
$\mathcal{G}(\mathbf{r} \mathbf{r}'), \mathcal{K}(\mathbf{r} \mathbf{r}')$	Green's functions
\mathbf{r}	Space position vector
$\delta(\mathbf{r})$	Dirac delta function
δ_{ik}	Kronecker delta function
t	Variable time
c	Speed of light
\mathbf{e}_θ	Unit vector in θ direction
J_θ	θ component of vector \mathbf{J}
f	Frequency
ω	Angular pulsation
\mathbf{Z}	Impedance matrix
\mathbf{Y}	Admittance matrix
$d, \overset{d}{\square}$	Number of dipoles, any value related to dipoles
$p, \overset{p}{\square}$	Number of panels, any value related to panels
$n, \overset{n}{\square}$	Number of nodes, any value related to nodes
\mathbf{P}	Potential coefficient square matrix
\mathbf{C}	Capacitance square matrix
D2N	Dipoles to nodes incidence matrix
P2N	Panels to nodes incidence matrix
T2N	Terminals to nodes incidence matrix
\mathbf{Q}	Charge matrix
\mathbf{I}	Current matrix
\mathbf{U}	Voltage matrix

Introduction

In recent years, power supply miniaturization and reliability concerns are being increasingly addressed by semiconductor companies through their ability to deliver advanced processing and functional integration in the form of system-in-package (*SiP*) and system-on-chip (*SoC*) platforms. This proliferation of functionally-integrated hardware solutions can be seen as an inflection point in the power supply industry which is seeing a dramatic move away from traditional power supply manufacturing (with a focus on the assembly of power supply modules or bricks from discrete components) to an increasing emphasis on integrated power supply products deriving directly from semiconductor and microelectronics products and technologies.

A major challenge to the further miniaturization of DC-DC converters is the inability to integrate passive components on silicon due to their relatively large size at today's operating frequencies of 0.5 to 5 Megahertz. Increasing the switching frequencies into the 10's of MHz region offers the potential for the reduction of passive component values to the point where, with the right technology, their size becomes compatible with silicon device dimensions. Currently, significant R&D activity is evident in both academia and industry into advances in semiconductor, magnetic, capacitor and packaging materials and technologies that will deliver products operating at multimegahertz frequencies. The ultimate target is to develop new miniaturized product formats that can be referred to as power supply-in-package (PSiP) and power supply-on-chip (PwrSoC).

Full integration of energy conversion devices for compact power supply circuits is still encountering strong technological locks, especially the integration of passive inductive and capacitive components. Indeed, those components are involved in various internal power supply functionalities for temporary energy storage during a switching period: filters, snubbers, damping, decoupling or clipping circuits, galvanic insulation stages, sensors, amplifiers... The increasing working frequency of those devices, which already reaches 1 Megahertz, would enable the size reduction of passive components and then their integration. Nevertheless, losses, which highly depend on frequency and technology, may complicate or even stop this increase. Actually, an integrated inductor always has an active behavior, which comes with the reactive one, due to its DC resistance, skin and proximity

effects in the conductors, eddy currents in the substrate and in the magnetic core, hysteretic losses in magnetic materials, etc... Various compromises are inevitable and that leads us to a necessary further study of physical phenomena occurring inside new prototypes of passive devices.

The objective of this work is a systematic study of integrated inductors structures through the developing of precise modeling and simulating methods on the frequency range from 1Hz to 1GHz. First, an analytic model based on PEEC (Partial Element Equivalent Circuit) method has been developed. This modeling approach has been adapted to the studied components: rotational symmetry, not negligible section conductors, thus taking all geometrical parameters (*width, thickness, etc.*) into account, inhomogeneous media, etc... The final model splits the physical study of the component into two steps: electromagnetic computations on subparts of the set (partial elements) and global frequency response calculus with the equivalent electrical models of the subparts.

A full process for the technological realization of inductive components has also been achieved in order to experimentally verify the modeling. In this way, several different processes, based on former studies carried out in LAAS-CNRS, have been improved and technological bricks have been adapted to concepts to be validated and to take the evolution of photoresists into account. The improvement of design resolution and increase of copper electroplating thickness, as planarization of conductor levels with SU8 resin have been specifically studied. Those overhangs have permitted the realization of multilevel and multiconductor inductors which present good features at high frequency.

Finally, the characterization of prototypes at low frequency has been enabled by the realization of an impedance measurement bench we developed for the range from 40Hz to 110MHz and high frequency characterizations have been performed with a network analyzer.

This work has been completed by the development of a very fast computing analytical model for the calculus of the magnetic field in integrated inductors. This method has been used to find the repartition of the magnetic field generated by integrated planar magnetic actuators excited by a DC current for a microsystems and microfluidics application.



Chapter 1

Integrated inductive components and applications

1 - Power supplies in electronic systems

A power supply aims at delivering direct voltages to electronic systems from a direct or alternative source (*the power grid, a battery, a photovoltaic panel, any DC source, etc.*). Furthermore, these power supplies must often provide galvanic insulation and regulation of the output voltage to compensate the variations of the input voltage and the load. They also need to perform high efficiency, to be soft and compact, and sometimes to deliver several isolated voltages. Since 1975, switch mode power supplies are commonly used instead of linear ones when efficiency is critical and when cost allows their use. The amelioration of this type of power supply is due to the evolution of the components they involve, their realization and integration techniques. The next part attempts to give an overview of the power supply problematic and the technological locks they encounter nowadays.

A - Evolution of power supply demand

Power supply is a generic term involving a large amount of electronic devices. We will focus on power supplies of embedded and autonomous systems which represent a fast growing market nowadays. Actually, one can observe simultaneously the apparition of new portable electronic devices (*cell phones, GPS, PDAs or MP4*), and the increase of the amount of energy needed due to

the increasing number of transistors inside the constitutive components of these devices (*microprocessors, microcontrollers, FPGA, ASICs, etc...*).

The tendency for power management in boards is the increase of conversion stages, thus allowing the energy transport with relatively high voltages and the functioning of devices at low voltages. This way, assuming that the efficiency of power conversion stages is good enough, line losses are reduced as well as the commutation losses in chips. One then talks about distributed power architectures (*cf. Fig. 1.1*).

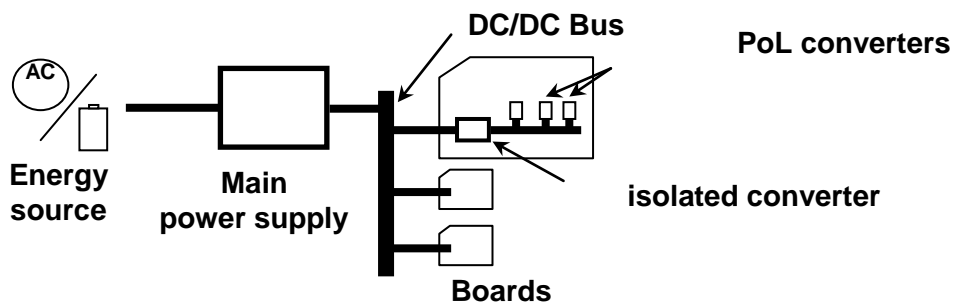


Fig. 1.1 - Distributed power architecture

At the end of energy distribution chain, Point of Load (*PoL*) converters are dedicated DC/DC converters which adapt power level according to the supply requirements of each load [Helie2004]. When this block is especially conceived to supply devices like embedded microprocessors, it is known as Voltage Regulator (*VR*). Hence, a VR is a high-efficiency power converter which can deliver the most advantageous power level depending on the conditions required by the load (*in steady and also during transient states*). Consequently, VRs allow a tight and fast regulation of their output variables. The efficiency of such devices is actually very sensitive about their packaging and many solutions are proposed and further investigated. Their design can vary from a part of the motherboard schematic, a standard fingerprint which authorizes the use of specific boards from various vendors, one main chip and some discrete components, a hybrid package that is close to a monolithic component or even in newest solutions a single full integrated component. The different packaging solutions have a consequent influence on **efficiency**, **cost** and **design easiness**. Furthermore, each innovation in that domain lead to a need for new command laws, as the active and passive components features differ notably from a system assembly type to another.

B - Evolution of power supplies structures

a - Linear regulator power supplies

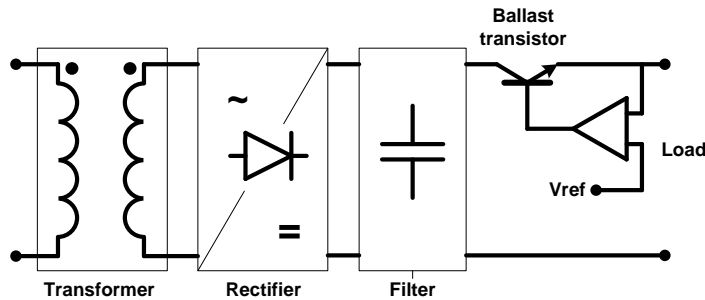


Fig. 1.2 - A linear regulator power supply connected to power grid [Ferrieux_book]

The most common use for these power supplies concerns non embedded systems which energy comes from the power grid. They are then composed of a transformer working at the grid frequency. This transformer provides galvanic insulation and adapts the voltage level. Its secondary is connected to a rectifier and a filter (*cf. Fig. 1.2*). The regulation is obtained thanks to a linear regime transistor (*called ballast*). Its collector to emitter voltage (V_{CE}) varies to maintain a constant voltage at the output, despite the variations of the input voltage.

b - Switching mode power supplies

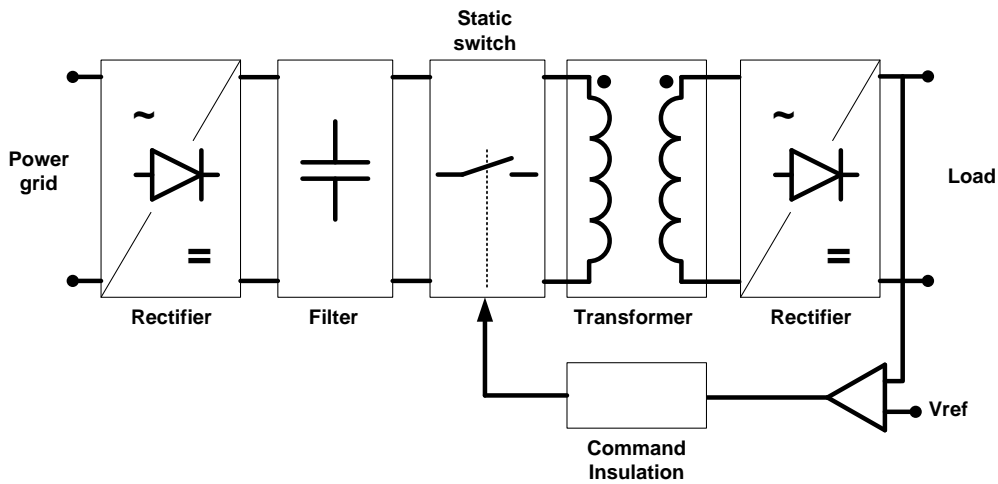


Fig. 1.3 - A switching mode power supply connected to power grid [Ferrieux_book]

In order to compare this type of power supplies with linear power supplies studied above, we propose on Fig. 1.3 the schematic of a standard switching mode power supply with galvanic insulation connected to the power grid. The power grid alternative voltage is first rectified and filtered. The direct voltage obtained is then “chopped” by a static switch (*i.e. a semiconductor device in switching regime*) which is commonly a MOSFET transistor in nowadays applications. The switching

frequency is always more than the limit of audible frequencies 20kHz. A high frequency transformer is thus used to perform the galvanic insulation of the power circuit and the direct output voltage is obtained by rectifying and filtering the secondary voltage of the transformer. The regulation variable is the ratio of the conducting time of the switch over the switching period, or duty cycle.

c - Comparison between linear regulation and switching mode power supplies

Characteristic	Linear regulation power supply	Switching mode power supply
Efficiency	35 to 55%	65 to 99% ☺
Specific power	10 to 30 W.kg ⁻¹	30 to 300W.kg ⁻¹ ☺
Power density	20 to 50W.dm ⁻³	50 to 300W.dm ⁻³ ☺
Input voltage range	0.9 to 1.1 Un	0.85 to 1.2 Un ☺
Dynamic regulation: Overshoot - Time constant	1% - 50µs ☺	5% - 1ms
Peak to peak ripple	0.1% ☺	1%
CEM disturbances	Low ☺	High

Fig. 1.4 – Comparison of typical characteristics of linear regulation and switching mode power supplies [Ferrieux_book]

Both linear and switching systems present advantages and disadvantages in their functioning (cf. Fig. 1.4). Switching mode power supplies have good efficiency and high specific power and power density. On the contrary, this method induces parasitic signals in and around the boards and there is still a non negligible ripple output voltage. However, switching mode power supplies tend to replace linear regulation especially in embedded systems like mobile phones, laptops, etc. since efficiency and then size are the main criteria for designers.

C - Constitution of switching mode power supplies

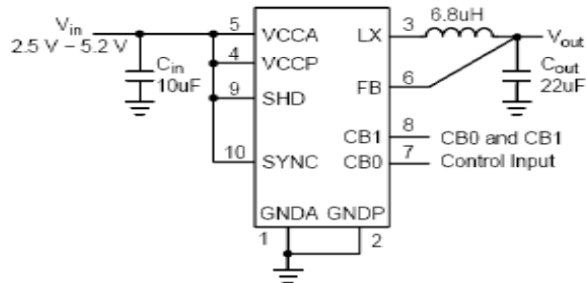
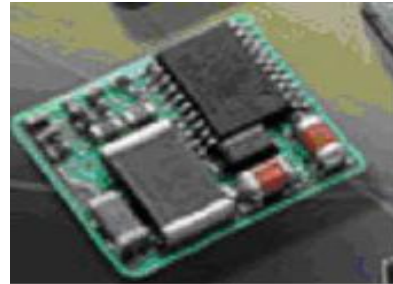


Figure 1. Typical Application Circuit



(a)

(b)

Fig. 1.5 - On Semiconductor step-down DC-DC Converter [NCP1508] 3mm x 3mm. Schematics (a) and photography (b)

As we saw before, the main stage of a switching mode power supply is always a DC-DC power converter (*chopper*). This kind of device can perform various functions, in addition to the voltage elevation or drop, as galvanic insulation and several more or less complex structures exist, depending on the requirements of the problem. The common point of any power stage of a power converter structure is that it is composed on one hand of semi-conductor devices for switches and on the other hand of passive components, namely inductors, transformers and capacitors (*cf. Fig. 1.5*).

The semiconductor devices, diodes, bipolar or MOSFET transistors, *etc.* are used as switches. Losses are thus low and they are due to conduction time (*on state resistance*) and to raising and falling voltages and currents during switches (*non zero power consumption*). The second important advantage of switching mode is that much higher frequencies can be used than the grid power frequency, leading to a much smaller insulating transformer. The switching frequency mainly depends on the switches characteristics: 1 to 5 MHz is a strict maximum in nowadays applications, except in very specific ones, involving very low power.

Passive components provide many functions in power converters, like filtering, insulating, *etc.* Their role can be understood as energy tanks or relays. Actually, the chopping implies some discontinuities in the energy transfer which must be smoothed to be delivered to the load. During each switching period, when permanent regime is reached, every passive device has a definite

behavior or cycle during which it stores and releases some energy. Capacitors store electrical energy and imply a voltage delay. Dually inductors store magnetic energy and imply a current delay, and finally transformers take advantage of the magnetic coupling phenomena to transfer energy from a primary coil to a secondary with galvanic insulation. Furthermore, they provide an easy way to adjust current or voltage level. The functional approach of inductive components (*inductors and transformers*) is developed in next section.

2 - Functional approach of inductors and transformers

Inductors and transformers belong to passive components family and they are used in every domain of electronics: high power distribution, microelectronics, radio-frequency systems, *etc.* They play a fundamental role in the functioning of converters, filters and galvanic insulation.

A - Definition of the ideal inductor

The realization of coils is generally considered as a difficult and expensive exercise by electronics designers, however, some applications does not allow the alternative. This especially true in energy conversion problems where the use of active components is prohibited because of efficiency considerations. Some signal applications also require inductive components in specific cases like RF filtering and impedance matching.

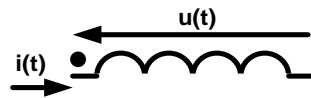


Fig. 1.6 - Receptive inductive dipole or ideal inductor

An inductor is a component that satisfies the relation (*with the receiver convention of Fig. 1.6*):

$$u(t) = L \frac{di(t)}{dt} \quad (1.1)$$

From an electrical point of view, the **inductance**, or inductor value, so called L , is the proportionality coefficient between the inductor voltage $u(t)$ and the derivative of its intensity $i(t)$. The only passive component that satisfies this relation is a coil. Actually, a coil is composed of conductor loops carrying a current intensity $i(t)$ inducing a proportional magnetic flux $\phi(t) = Li(t)$, which variation is responsible, in turn, of a back electromotive force $u(t) = \frac{d\phi(t)}{dt}$ with receiver convention. Obviously, some active components exist that copy this electrical function: one talk about simulated inductors.

Another approach of the inductor is to consider the energetic behavior of such a component. From a physical point of view, the magnetic energy density $w_m(\mathbf{r})$ at each point of space defined by the position vector \mathbf{r} can be expressed as:

$$w_m(\mathbf{r}) = \frac{1}{2} \mathbf{B} \cdot \mathbf{H} \quad (1.2)$$

where \mathbf{H} is the magnetic excitation vector representing the action of the source current and \mathbf{B} is the magnetic flux density vector representing the reaction of the medium to the excitation. The common expression of \mathbf{B} as a function of \mathbf{H} is:

$$\mathbf{B} = \mu_0(\mathbf{H} + \mathbf{M}) = \mu_0\mu_r\mathbf{H} = \mu\mathbf{H} \quad (1.3)$$

where \mathbf{M} is the magnetization of the medium and μ_0 is the permeability of the vacuum. One can see that the magnetic flux density can be decomposed into two components: $\mu_0\mathbf{H}$ and $\mu_0\mathbf{M}$. The $\mu_0\mathbf{H}$ component exists in any medium, even in vacuum, and corresponds to the “distributed” energy of the source current. The $\mu_0\mathbf{M}$ component only exists in magnetic materials and corresponds to the energy stored by the reorganization of its elementary particles. This sum of behaviors is generally confounded by defining the global permeability of the medium μ or its relative permeability μ_r . This description is sufficient for the modeling of the inductive component; however, the two physical phenomena responsible for energy storage must be clearly understood for the preliminary design considerations.

Actually, one can realize inductors without magnetic material, which is advantageous when a perfect linearity between the magnetic excitation and the magnetic flux density is needed (*no saturation effect*), or when relatively small values of inductance compared to the available size of the device are required. On the contrary, the use of magnetic materials enables large values of inductances in a small amount of space dedicated to the component, as the relative permeability can be about 2000 or more. Magnetic materials, however, generally present constraints about magnetic fields such as saturation, hysteretic behavior, etc. These losses sources will be further developed in chapter 2. Finally, an intermediate solution to the design of inductor can be the use of a magnetic circuit made with high relative permeability materials which present a small air gap that globally reduces the relative permeability and then increases the allowed excitation before saturating the magnetic material. Another technique consists in using hybrid materials that present a distributed air gap (*inhomogeneous material*).

Whatever the design is, a component of inductance L with intensity $i(t)$ going through stores magnetic energy $w(t)$:

$$w(t) = \frac{1}{2} Li(t)^2 \quad (1.4)$$

This relation is fundamental for the design of an inductor since the dimensioning of its magnetic circuit will depend on the quantity of energy stored.

Many physical phenomena, most relevant from electromagnetism, take place in a real inductive device, so that it is impossible to realize an ideal one. The various losses causes are extensively developed in chapter 2 and associated models are proposed.

B - Definition of the ideal transformer

The same physical phenomenon of magnetic induction is used in transformers. This two-port (or n -port) device is composed of two (or n) coupled inductors as shown on Fig. 1.7 (a). When it is used to store energy from various points of an electronic circuit, one talk about coupled inductors (e. g. in flyback converter), but the particularity of magnetic coupling is that energy can be transferred from one port to the other (e.g. in forward converter). In this case, the component is called transformer. Fig. 1.7 (b) shows the schematic of an ideal transformer.

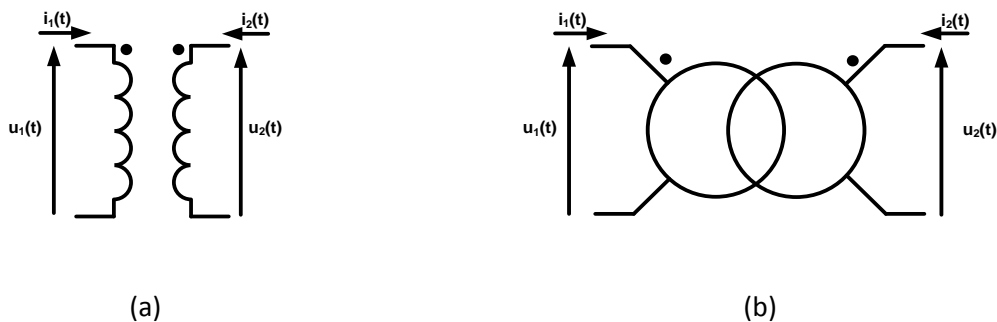


Fig. 1.7 - Ideal transformer. Coupled inductors representation (b) and two-port schematic (a)

By definition, a two-port is a transformer if the following relations are simultaneously verified:

$$\frac{u_1(t)}{u_2(t)} = \ddot{u} \quad (1.5)$$

$$\frac{i_1(t)}{i_2(t)} = \frac{1}{\ddot{u}} \quad (1.6)$$

where \ddot{u} is called the transformer-turns ratio. One can then easily verify that an ideal transformer presents the same power (product of i and u) at each port, i.e. the energy is transferred without losses. The real transformer obviously presents losses due to flux losses, magnetizing consumption, ohmic losses in conductor, etc. This can be interpreted in terms of structural lumped elements (resistors and inductors). Chapter 2 gives the physical interpretation of losses in inductive

components and appendix 1 presents the standard model of a real transformer and defined the electrical parameters used.

3 - Integrated inductive components and associated models

We have demonstrated in section 1 that a power supply for an embedded or autonomous system is no more a separate board; on the contrary, energy management is enhanced thanks to a complex distribution network including disseminated power conversion stages. Design considerations thus systematically include conversion blocks and, therefore, applicative market is eager to propose “turnkey” components providing such electronic functions. Actually, the integration of switching mode power supplies, generally basic conversion structures like buck or boost converters, seems to be the answer to this need of size decrease (*referred to as “footprint reduction”*), design simplification and noise reduction.

Passive components are usually blamed for being too much space consuming since they are energy tanks of conversion structures. Actually, designers deal with compromises: the faster switching active components, the smaller passive components needed; the bigger the capacitor, the smaller the inductor; the smaller the component, the bigger the losses, etc... It is then quite impossible to give a strict comparison of previous works found in literature since they are never presented “all things being equal”. We can notice, however, that technological improvements for five years (*since 2003*) have globally lead to the increase of switching frequencies, maximum admissible powers and finally efficiencies and performances.

Next part tries to point out some interesting improvements or innovations in technology of integrated inductors and to provide an “order of magnitude” of today potential of integrated or semi-integrated structures. The following part is, in turn, dedicated to the modeling software tools which cannot be ignored in integrated inductors design considerations today, partly because of the previously mentioned improvements and resulting complexity.

A - Technological improvements in inductors integration

Three kinds of integrated power inductors can found in literature: serpentine, meander and spiral. Even if all of them can be realized with planar technology, spiral inductors are the easiest to realize since there is no intersections between conductor and magnetic core layers (*sandwich structure*). The low complexity of the structure seems to determine its use in most applications.

integration of power inductors which provide good efficiency converters. Technological improvements lead to hopeful results anyway, directly and indirectly. Indeed, resistance amelioration can be achieved by increasing the thickness of the conductors (*direct amelioration*) or by reducing the inductance value (*indirect amelioration*). Those two goals are pursued simultaneously by researchers who propose both “exotic technologies” for the inductance design and solutions to increase the switching frequency.

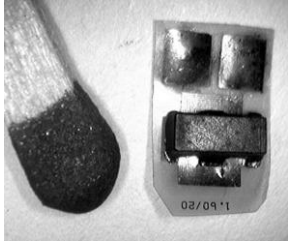
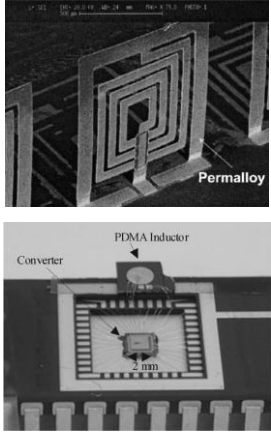
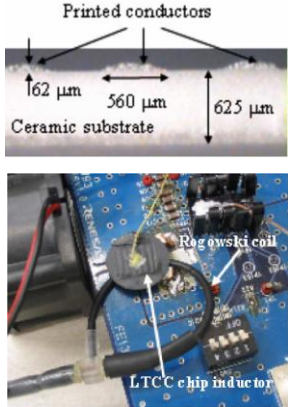
 <p>Process:</p> <ul style="list-style-type: none"> • Electroplated copper • Polyimide substrate • Ferrite magnetic core. <p>Dimensions (μm): 4000x1000x130</p> <p>Electrical characteristics:</p> <ul style="list-style-type: none"> • $L_s=8.5\mu H$ • $R_s>10\Omega$ • $SRF>10MHz$ 	 <p>Process:</p> <ul style="list-style-type: none"> • Electroplated copper • Permalloy Plastic Deformation Magnetic Assembly <p>Dimensions (μm): 1000x1000x6</p> <p>Electrical characteristics:</p> <ul style="list-style-type: none"> • $L_s=1\mu H$ • $R_s=750m\Omega$ <p>Application: Buck converter</p> <ul style="list-style-type: none"> • $V_{in}=4V$ • $V_{out}=2V$ • $f=10MHz$ • $R_{load}=100\Omega$ 	 <p>Process:</p> <ul style="list-style-type: none"> • LTCC (<i>Low Temperature Co-fired Ceramics</i>) <p>Electrical characteristics:</p> <ul style="list-style-type: none"> • $L_s=14nH$ • $R_s=20m\Omega$ • $SRF>5MHz$ • $I_{MAX}=1A$ <p>Application: Multiphase buck converter @5MHz</p>
(a)	(b)	(c)

Fig. 1.10 - Examples of solution for integrating power inductors and implementation in power converters. Thin film substrate (a) [Saidani2003]. Vertical implementation (b) [Munusuri2005, Munusuri2005a]. Ceramic substrate (c) [Lim2007].

Fig. 1.10 shows three examples of solutions available at present for the integration of inductors. The common point of these three realizations is the use of non conventional technology which leads

to solutions that are hard to industrialize. Authors propose interesting solutions for footprint size reduction or losses reduction (*the two main problems*). Actually, substrate losses are reduced by using dielectric substrates [Saidani2003, Lim2007] or magnetic verticalization of the component [Munusuri2005]. Another way to achieve very low DC resistance is given by [Pan2005] where very thick electroplated copper is realized inside silicon substrate by DRIE etching, thermal oxidation, copper electroplating and backside KOH etching (*Inductor performances are good: $L_s=2\mu H$, $R_s=150m\Omega$, $SRF=150MHz$*). Converter switching frequencies appear to be in the range 500kHz-5MHz nowadays and multiphase converters (*interleaving*) also take an increasing part of proposed solutions.

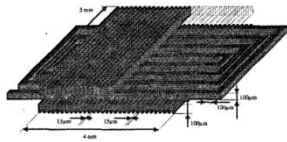
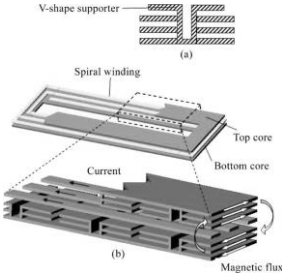
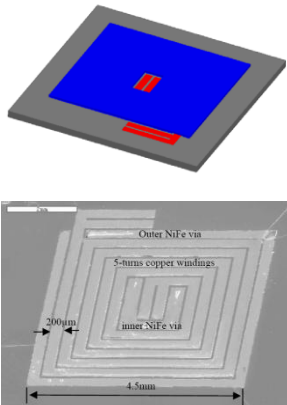
 <p>Process:</p> <ul style="list-style-type: none"> • Electroplated copper • Laminated NiFe layers core <p>Dimensions (μm): 4000x3000x500</p> <p>Electrical characteristics:</p> <ul style="list-style-type: none"> • $L_s=1.27\mu H$ • $R_s=200m\Omega$ • $I_{MAX}=1.33A$ <p>Application: Buck converter</p> <ul style="list-style-type: none"> • $V_{in}=3.3V$ • $V_{out}=1.5V$ • $f=500kHz$ 	 <p>Process:</p> <ul style="list-style-type: none"> • Electroplated copper • Micron-scale laminated NiFe core (<i>72 laminations</i>) <p>Dimensions (μm): 11500x5700x700</p> <p>Electrical characteristics:</p> <ul style="list-style-type: none"> • $L_s=2.3\mu H$ • $R_s=150m\Omega$ • $I_{DCsat}=200mA$ <p>Application: Boost converter</p> <ul style="list-style-type: none"> • $V_{in}=7V$ • $V_{out}=12V$ • $f=2.2MHz$ • $\eta=71\%$ • $P_{out}=1.9W$ 	 <p>Process:</p> <ul style="list-style-type: none"> • Electroplated copper in DRIE trenches in silicon (<i>idem [Pan2005]</i>) • Powder permalloy core <p>Electrical characteristics:</p> <ul style="list-style-type: none"> • $L_s=179nH$ • $R_s=23m\Omega$ • $I_{DCsat}=5A$
(a)	(b)	(c)

Fig. 1.11 - Examples of “standard process” power inductors with magnetic core and implementation in power converters. Single layer laminated core (a) [Bogetto2002, Bogetto-thesis]. Multilayer laminated core (b) [Park2003, Park2004]. Distributed air gap core (c) [Wang2007].

Magnetic core realization is also a very important issue for the integration of inductors. Fig. 1.11 presents, through examples, the three kinds of electroplated cores: simple core, laminated or not, multilayer laminated core and distributed air gap core. Simple cores are the easier to realize since only two process steps are needed for a sandwich structure [Bogeto2002]. Multilayer laminated core is much complex to realize but seems to present very good results (*high inductance value with low resistance in high frequency too*) [Park2004]. Finally, distributed air gap cores, generally made of Permalloy, avoid lamination steps and present good results too; Permalloy deposit is newly available in standard processes and tends to be more and more used [Wang2007].

As the working frequency of applications increases, the inductance value needed is decreased and so is the DC resistance, but associated high frequency losses increase. Compromises are made between standard design consideration and new RF techniques design consideration. On this basis, we believe that circular spiral inductors (actually omnipresent in RF microsystems) will be used more and more as they present the less lossy topology in high frequency (*avoiding large amount of energy storing in tiny places*).

Finally, one must notice that inductor integration is generally top end process, i.e. the inductor is realized after the circuitry and on the substrate surface. This directly addresses the point of electromagnetic compatibility: the influence of the field generated by the inductor over the active circuitry. Nastos especially studied the coupling effects between an integrated inductor and a CMOS transistor placed at various places under the inductor [Nastos2006].

In conclusion, noticing that similar researches are pursued for capacitor integration, fully integrated power converters begin to be reality as some providers propose solutions with integrated inductor [Enpirion_url] and recent literature gives examples of integrated buck converters including LC filter (*cf. Chapter 5*) [Abedinpour2006]. However, efficiencies are low (*64% for last reference*), because compromises between working frequency, inductor and capacitor size and losses are still hard to deal with. Solutions are becoming available thanks to technological improvements (*conductor thickness, high quality magnetic cores, etc.*) and next generation of integrated devices will probably have interesting performances. The design of such structures becomes more and more complex and specific computer aided design tools are inevitable.

B - Spiral inductive components modeling and simulation tools

a - Analytical models

Physical modeling of spiral inductive components requires the solving of electromagnetic equations. Numerous analytical solutions exist for simple problems. Unfortunately, magnetic field

produced by the full spiral (*rectangular, octagonal, circular...*) cannot be calculated at once. Furthermore, the inhomogeneous medium surrounding the components bring some more difficulties in the calculus.

First, inductance of spiral components has thus been calculated in “free space”, *i.e.* in a homogeneous medium presenting vacuum properties like air. The conductors of the spiral can be decomposed into two kinds of elementary elements which field solution is known: straight segments or circular loops. They can also be modeled as filiform conductors or volume conductors depending on the calculus. F.W. Grover gives numerous approximated formulae for the calculus of self and mutual inductances of various conductors shapes combining Cartesian or Axisymmetric geometries and filiform or volume conductors [Grover_book].

The issue of integrated inductors calculation has been first addressed by Greenhouse who proposes a method for the calculus of rectangular spiral inductors based on the summing of the contribution of each segment [Greenhouse1974]. Several papers propose similar methods, with the evident will to simplify calculus by allowing the neglecting of the contribution of some terms (*e.g. perpendicular segments...*). This preoccupation corresponded to the lack of computation power of that time. These fast computing formulae are very useful in today approaches, however, because more precise modeling can lead to the meshing of a structure into a big amount of elementary segments, leading to the same need of computing power. Furthermore, these “old” formulae are often basis of new works [Chan2003] and offer more precision and easiness of implementation [Artillan2008a].

The decomposition of the structure into segments relies on the subjacent concept of partial inductance, *i.e.* the inductance of loop segments. This concept has been formally exposed by A. E. Ruehli [Ruehli1972]. The major work of A.E. Ruehli is the formalization of the Partial Element Equivalent Circuit (PEEC) method. This method synthesizes the principle of lumped elements circuits and the calculation of the parameters values from electromagnetic equations [Ruehli1973]. He has extensively developed this method in Cartesian coordinates so that any structure of conductors can be meshed into equivalent resistive, inductive and capacitive dipoles. The computation is based on an integral formulation of electromagnetic equations (*cf. Chapter 4*) so that the whole volume of conductors is dealt with in the same calculus, contrary to finite elements methods or others. The advantage of this method is the separation of electromagnetic calculus of the partial elements values and the classic electrical study of their interconnections. Many works have been performed since, leading to the taking into account of non rectangular parallelepiped structures, non homogeneous medias, time domain analysis [Ruehli1996]...

The PEEC method has been implemented in several software tools, thus allowing the computer aided design (*CAD*) of package connections or components:

- FastHenry, FastCap and FastModel are three compatible software packages, developed at Massachusetts Institute of Technology, USA, for package interconnections design in radio-frequency applications. It computes equivalent models to chip access wires in order to calculate signal integrity parameters. Capacitive effects are taken into account and a reduction order algorithm leads to very fast computing time [Kamon1994, Kamon1998, Kamon_thesis].
- Asitic, developed at University of Berkeley, California, USA, is especially dedicated to RF inductor design. This tool proposes a good environment for the design of components and can generate technological compatible files (*.gds or .cif*). It includes layer substrate modeling, and volume conductors with skin effect approximation. It is not able to model circular conductors however and is then very time consuming for the calculus of circular loops as it divides them into numerous segments [Niknejad1998, Niknejad_thesis].
- Numerous other tools are proposed in literature, based on the same PEEC formulation, but proposing approximated formulae to fasten the computing time. INCA (*Inductance Calculation*), developed at Laboratoire d'Electrotechnique de Grenoble, France, proposes a full software tool dedicated to the computation of inductive effects of interconnections by PEEC method applied to conductors approximated by filiform straight wires [Clavel_tech]. Escovar also developed a tool for Mentor Graphics [Escovar_thesis]. These tools are generally compared to FastHenry or Asitic in terms of performances.

PEEC method can also be extended to RF domain [Ruehli1996]. This feature has not been deeply investigated; however, the use of Green's functions in the formulation appears to be the key to adapt this method to propagation domain. Actually, the formalism is then conserved, while propagation delay, as well as layers interfaces reflection coefficients, are included in the Green's function replacing the standard kernel of integral formulae. B. Rejaei proposes an interesting work about RF circular spiral inductors modeling [Rejaei1998, Rejaei2004]. M. Kamon proposes an investigation of Quasistatic versus full-wave PEEC analysis which concludes that for conductors of length about a wavelength and closer than a wave length one from another, quasistatic approach is generally about one percent accurate [Kamon_thesis, appendix A].

Many other lumped element models based on structural decomposing of integrated inductive components or even on curve fitting techniques are available, depending on electromagnetic effects taken into account (*cf Chapter 2*) [Hurley1999]. The most common model is exposed in [Yue2000] or [Vanhese2002] which parameters can be both computed from structural approach (*each lumped element is calculated with a simple formula*) or from frequency response curve fitting. These latter

approach are advantageous to provide very fast order of magnitude of the component behavior, but do not allow the precise computation of every kind of losses. Next part will develop the simulation method that is much more computing time consuming but gives very precise results.

b - Simulation with electromagnetic solvers

The most common method to simulate electromagnetic components is the finite elements method (FEM), or finite element analysis method (FEA), which is a mathematical scheme for the resolution of potentially any partial differential equation set applied to a meshed structure. For electromagnetic problems, various sets of equations derived from Maxwell's can be used depending on the type of the problem. This method offers great precision for the computation of impedance response versus frequency for inductive devices. This section gives us an overview about the existing electromagnetic software in order to justify our choice for inductors simulation. It attempts to sort the electromagnetic design concerns into three classes: quasistatic, signal integrity and full-wave problems. It also enhances the many specific features to be taken into account when choosing one of the numerous different packages available on market. It refers to the type of implemented computing method, the topology limitations and the computer resources needed (*speed and type*).

Classes of electromagnetic devices and problems

It is impossible to classify all electromagnetic devices and problems that one may wish to solve with Finite Element Method (*FEM*). Still, three broad classes of applications can be identified for which electromagnetic (*EM*) software tools are available:

- **Low-frequency devices** such as electric motors, transformers, and actuators. Here a variety of two- and three-dimensional FEM packages are used to predict electric and magnetic fields, torques, forces and impedances. Planar 2-D, axisymmetric 2-D and 3-D circuit simulators are available such as Ansoft (*Maxwell2D/3D*), Cedrat (*Flux2D/3D*), etc.
- **Broadband electronic circuits**, such as computers or any complex signal processing board. Here, these programs are used to predict signal integrity, cross-talk, or ElectroMagnetic Interference (*EMI*). Planar 2-D and 3-D circuit simulators are available from vendors like Ansoft (*Simplorer*), Sonnet Software, etc.
- **Microwave components, antennas and radar systems**. In this case, electromagnetic simulators, performing high-frequency electromagnetic analysis, serve to predict S-parameters, radar cross sections, and radiation patterns. Recent advances in computationally efficient high-frequency algorithms have been implemented into several products from Ansoft (*HFSS*), Agilent (*Momentum*), etc.

Another less applicative but more physical classification could be **quasistatic** and **full-wave** problems:

- **Quasistatic problems** are solved with simplified Maxwell's equations, where the propagating time of potentials is neglected, leading to non coupled equations for the magnetic and the electric field,
- whereas **full-wave problems** need to be solved with the full Maxwell's equations, leading to propagating electromagnetic waves simulation.

The frontier between those two domains of electromagnetism is blurred as the quasistatic approach is a particular case of the full-wave approach but which leads to specific equations and interpretations of physical phenomena like voltage and intensity concepts. Furthermore, the concepts of voltage and intensity have then been generalized for hyper frequencies devices working in transverse electromagnetic mode (*TEM mode*) like coaxial cables or quasi-TEM mode like microstrip lines, RF passive devices, etc.

The key quantity allowing determining whether either the quasistatic approach or the full wave one should be used is the largest dimension of the system which must be compared to the wavelength at the working frequency. In the case of spiral inductors, the largest dimension is given by the length of the spiral since the propagation occurs along the conductor [Mirotznik_url].

Specific features to software tools

Some specific features must be looked at when choosing electromagnetic software. The following part tries to highlight some important ones.

First, an EM package must be general enough for different applications yet with enough special features to adapt it to one particular application. **Modularity** lends itself well to the solution of EM problems, since the process itself can be broken down into several steps: the geometrical modeling of the physical object; the creation of an analytical mesh, the analysis proper, and finally the postprocessing, plus, when needed, the graphic representation. The geometrical modeler, the first step, can be a common module used for nearly any application. The same cannot be said for the others. The analysis and postprocessing modules are very application specific. One module apiece is required for electrostatics, magnetostatics, radiation, scattering, and more. Some solutions have been developed in a common interface where various modules can be executed and bought separately.

In a second time, if EM simulators are to predict electromagnetic behavior as accurately as possible, they should be able to **model all the structural and material properties** of a device. Most

modern EM simulators do so by incorporating a graphically based preprocessor into the simulation package. Through the preprocessor, users can define the geometry, using modeling tools similar to those found in common computer-aided design (CAD) software, and can assign boundary conditions, material properties, and energy sources. In addition, many solutions include the capability to automatically translate geometrical models imported from popular CAD programs.

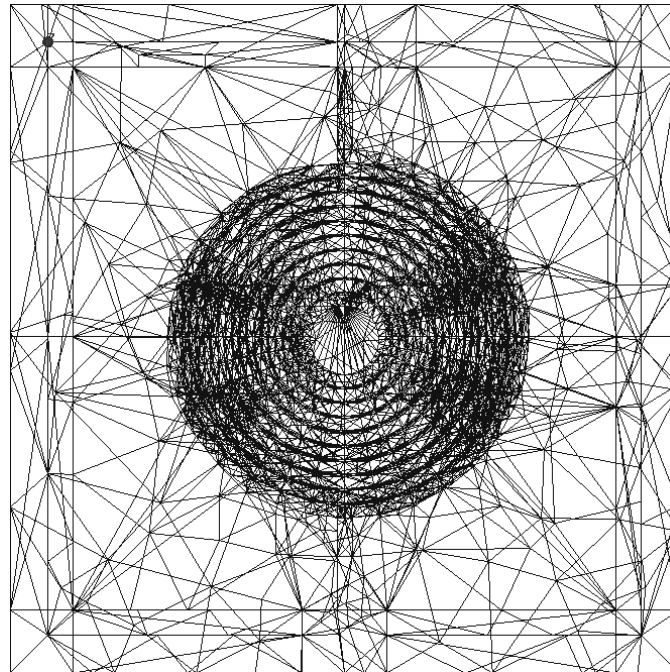


Fig. 1.12 - An example of automatically refined mesh based on magnetic energy calculus by Ansoft software HFSS

Once the device has been geometrically modeled, a so-called solution space must be created to exactly relate to that model: a **mesh** of small computational elements needed for the analysis. Finite-element solvers, for example, require a mesh of non overlapping 2-D or 3-D elements, like triangles or tetrahedrons, respectively. Many finite-difference solvers, on the other hand, use a grid of rectangular cells, which results in a staircase-like approximation to curved surfaces. Constructing the mesh is a critical step on the way to a solution. A well-designed mesh produces results that are both accurate and computationally efficient. A perfect mesh, of course, does not exist: trade-offs are always made among accuracy, computation time, and memory requirements. Some packages, such as Ansoft Corp. software suite, use an advanced **adaptive mesh-generation** method that simplifies the process even further (*cf. Fig. 1.12*). These programs adaptively adjust the mesh- refining elements only where needed, *i.e.* near regions of rapidly varying fields or sharp discontinuities. The program will iteratively adapt the mesh until some prescribed criteria of maximum error are satisfied. Nonadaptive codes can require many hours of experimentation by the user in finding a mesh that yields an accurate solution.

Once the geometry is at hand, the next step is the analysis. Recent theoretical advances in computational electromagnetics have resulted in a host of **new algorithms for EM analysis**, many of which have entered commercial software. These include finite-element and boundary-element method (*FEM and BEM*), moment method (*MM*), transmission-line matrix method (*TLM*), finite-difference method (*FDM*), finite-element and finite-difference time-domain (*FETM and FDTD*), as well as combinations of these methods. Each method offers advantages and disadvantages that fit it more to a certain class of problems than to the others. The finite-element method shines at modeling complex structures with curved boundaries, but may balk at problems that are electrically large (*many wavelengths in size*) because so much memory is required. On the other hand, methods such as finite-difference time-domain can tackle larger problems, but may have difficulty conforming to curved surfaces.

In the final step, sense must be made of the megabytes of data spawned during a typical EM simulation. One obvious approach is to assemble field results graphically. Modern EM software, capitalizing on the power of graphics workstations, can generate some truly extraordinary-looking plots thanks **graphical visualization tools**. Some EM simulators can display fields in an assortment of graphical formats, including 2-D and 3-D arrow, contour, and shaded plots. Some programs can even generate animated movies of EM fields propagating through space, rebounding off objects, or radiating from antennas.

In addition to displaying results graphically, EM simulators must be capable of **calculating a wide range of parameters**: impedances, parameters, ohmic losses, and radar cross sections are just a few. Since no one can anticipate every output quantity a user may wish to generate, **field calculators** are now part and parcel of some packages. The calculators permit the user to choose from assorted vector and scalar operators to manipulate field data into whatever form he or she may wish [Mirotznik_url].

4 - Conclusion / Contribution of this thesis

We have seen in this chapter that power supply of embedded and autonomous systems tend to be distributed on circuit boards, resulting in many conversion stages with high efficiency. The actual challenge is the realization of fully integrated power conversion devices based on switch mode power supply principle. Common conversion structures are buck, boost or interleaved power converters, which all require passive components in addition to the active switch and command circuitry. Their integration is considered today as a technological lock since high values of inductance and capacitance cannot be achieved in small footprints and without important losses. The case of inductive components has been further studied and demonstrates that, nevertheless, literature

proposes several technological solutions. The most promising topology seems to be spiral integrated inductors, with or without magnetic core, depending on the switching frequency of the power supply application and we foresee that circular spiral inductors will occupy a more and more important place in these applications as increasing the working frequency implies new problematic which look like radio-frequency problematic.

The integration of inductors seems to be feasible thanks to technological improvements and computer aided design becomes a need for that kind of device. General electromagnetic solvers can be used and a global approach of the available software in this domain has been proposed. Analytical approaches, however, are useful for designers, as they are much faster than finite element simulations, either to quickly give an order of magnitude of the performances of the component or to perform design optimization.

Integrated inductors can also be used as magnetic actuators and a presentation of lab on chip applications has been proposed. Here again, modelization appears to be fundamental for the design of optimized components.

The contribution of this thesis consists, first, in proposing modeling tools for spiral integrated inductors, as well as technological improvements for their realization and characterization. Next chapter is dedicated to the detailed presentation of losses and associated models of integrated inductors. In following chapter, we will present the methodology we used to simulate our components with finite element solvers. Software evaluations have been performed that justify our choice. Several key concepts for efficient simulation are investigated and simulation results are presented. After this simulation approach, a full semi analytical model based on Partial Equivalent Element Method (PEEC) for circular spiral inductors is proposed. This formulation leads to fast and accurate way to model axisymmetric inductive components (*inductors and transformers*). Then, technological realization with process optimization is then described and, finally characterization of prototypes is also studied. This experimental approach has been the way to validate the latter model. Finally, in addition to the electrical model for inductors, we propose an analytical method for the magnetic field calculation that has been used in microfluidics actuators application.

To summarize, this thesis is then essentially devolved to modelization, but technological realization and experimental characterization have also been an important part of the work, leading to models validation.

Chapter 2

Physical phenomena in integrated inductors and associated models

1 - Introduction

The modeling of integrated spiral inductors requires, after the precise definition of the application, the identification of physical phenomena inside the component, which can be useful or parasitic. As we studied in chapter 1, the primary function of an inductor is magnetic energy storage. However, realistic devices demonstrate experimentally that a parasitic serial resistance is always associated to the component, which compromises its functioning. This phenomenon, which can even be shown in static regime, tends to be increased at higher frequencies. A capacitive behavior can also be observed from a certain frequency called serial resonance frequency. Finally, it can be demonstrated that spiral inductors are very dependant of their environment, especially on the properties of their magnetic core and the substrate they lay on.

Depending on the needs of designers, various inductor models are available. Each application requires different dimensioning of elements constituting the inductor and some of the losses mentioned above can be neglected. Finally, the designer must choose the right model among a set of more or less complex ones. This chapter aims at presenting some common models sorted by the kind of losses they take into account.

2 - Preamble

The electrical model of a component consists in a formal representation of its behavior from the electrical point of view. Several questions must be answered before choosing a representation kind:

- How many electrodes does the system have, or, from a circuit theory point of view, how many ports are useful to take every kind of excitation into account?
- Is the system behavior fully controlled by linear equations and, consequently, is the frequency approach relevant or not?
- Is the system in quasi-stationary regime approximation or are propagation time non negligible? If propagation-time are consequent, is the wave propagation in Transverse ElectroMagnetic (*TEM*) or quasi-TEM mode?

One-port or two-port?

We will first present one-port approach which is analogous to differential mode approach of the inductor, and then the two-port approach which also considers common mode. Indeed, by defining the ground as a supplementary electrical node representing the environment limit of the system, one can model the impact of phenomena occurring even if only one electrode is excited, which is close to common mode concept. Obviously, common mode is not always useful to model and the designer chooses to take it into account or not.

Linear or not?

The linearity of the system is generally verified as we consider only electromagnetic phenomena which are described by Maxwell's equations:

$$\left\{ \begin{array}{l} \nabla \times \mathbf{E} = -\frac{\partial \mathbf{B}}{\partial t} \\ \nabla \times \mathbf{B} = \mu \mathbf{J}_c + \mu \varepsilon \frac{\partial \mathbf{E}}{\partial t} \\ \nabla \cdot \mathbf{E} = \rho / \varepsilon \\ \nabla \cdot \mathbf{B} = 0 \end{array} \right. \quad (2.1)$$

These equations are further detailed in chapter 4. Nevertheless, one can observe that electric and magnetic fields \mathbf{E} and \mathbf{B} are related by linear differential operators, time derivatives and constant parameters. In general, these equations are then linear and the electrical behavior of the system is necessarily described by a linear model. An exception to this assertion we will encounter, however, is the case of a hysteretic magnetic material. In that case, the magnetic permeability μ is no more a scalar constant, but a non linear function of the magnetic excitation.

Quasi-stationary regime or full-wave?

Voltage and intensity of current concepts have been introduced to simplify the study of electrical circuits. The principle on which those concepts rely on is that the propagating time of potentials is negligible:

$$\left\{ \begin{array}{l} \vec{\phi}(\vec{r}, t) = \frac{1}{4\pi\epsilon_0} \iiint_{r' \in V} \frac{\rho\left(\vec{r}', t - \frac{\|\vec{r} - \vec{r}'\|}{c}\right)}{\|\vec{r} - \vec{r}'\|} dV \approx \frac{1}{4\pi\epsilon_0} \iiint_{r' \in V} \frac{\rho(\vec{r}', t)}{\|\vec{r} - \vec{r}'\|} dV \\ \vec{A}(\vec{r}, t) = \frac{\mu_0}{4\pi} \iiint_{r' \in V} \frac{\vec{J}_C\left(\vec{r}', t - \frac{\|\vec{r} - \vec{r}'\|}{c}\right)}{\|\vec{r} - \vec{r}'\|} dV \approx \frac{\mu_0}{4\pi} \iiint_{r' \in V} \frac{\vec{J}_C(\vec{r}', t)}{\|\vec{r} - \vec{r}'\|} dV \end{array} \right. \quad (2.2)$$

where $\Phi(\mathbf{r}, t)$ and $\mathbf{A}(\mathbf{r}, t)$ are respectively the electric and the magnetic potentials. These expressions are established in chapter 4: (3.22) and (3.23). The strikeout term indicates that the propagation time is very little compared to the variation last of the system. In that case, the concepts of voltage and intensity are well defined:

$$U_{AB} = \phi_A - \phi_B = - \int_{\phi_A}^{\phi_B} d\phi = \int_A^B -\overrightarrow{\text{grad}} \phi \cdot \overrightarrow{dl} = \int_A^B \left(\vec{E} + \frac{\partial \vec{A}}{\partial t} \right) \cdot \overrightarrow{dl} \quad (2.3)$$

$$I = \iint_S \vec{J} \cdot \overrightarrow{dS} = \iint_S \left(\vec{J}_C + \frac{\partial \vec{D}}{\partial t} \right) \cdot \overrightarrow{dS} \quad (2.4)$$

where U_{AB} is the voltage between point A and point B, and I is the intensity going through a section S of conductor.

When propagation is no more negligible, signals become waves and their representation is much more complex. One special case, however, is the TEM mode case. If the structure can be demonstrated to work at TEM or quasi-TEM mode - *i.e.* electric and magnetic fields belong to the plane perpendicular to the propagation direction - one can use the concepts of voltage and intensity though. The model is then an external representation of the device, only showing its behavior at some points, and hiding the propagation phenomenon with lumped elements. We will not present any model that does not verify the condition that lumped elements can be used (*quasi-stationary or TEM or quasi-TEM*).

3 - One-port models

At low frequency, a coil can be considered as a one-port device, *i.e.* the knowledge of the potential of its two electrodes is sufficient to fully describe its behavior. We will see in section 3 that when frequency increases, at least ground potential must be taken into account.

A - Serial resistance



Fig. 2.1 – Frequency dependant equivalent model of an inductor

At pulsation ω , the coil conductors, generally made of copper with resistivity ρ , are responsible for the serial resistance $R_s(\omega)$. In static regime, the value of this resistance is proportional to the length l of the conductors and inversely proportional to their section S :

$$R_s = \frac{\rho \cdot l}{S} \quad (2.5)$$

At low frequency, inductive effect coupled with resistive losses can be modeled in a very easy way by decomposing the equivalent impedance expression:

$$Z(\omega) = R_s(\omega) + j \cdot L_s(\omega) \cdot \omega \quad (2.6)$$

B - Leakage inductance



Fig. 2.2 – Proper inductance and leakage inductance

Leakage inductance is a notion specific to magnetic core inductors. Indeed, the total magnetic flux ϕ_T is split into magnetic circuit flux ϕ_p and air circuit flux ϕ_f :

$$\phi_T = \phi_p + \phi_f \quad (2.7)$$

The total inductance $L_s = \frac{\phi_T}{I}$ can thus be expressed as the sum of the proper inductance and the leakage inductance:

$$L_T = L_p + L_f \quad (2.8)$$

C - RLC lumped model

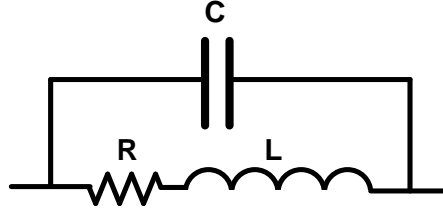


Fig. 2.3 – Lumped elements model of an air inductor

Capacitive effects also occur in the dielectric part of the component (outside conductors). This means that some current flows directly from turn to turn as the dielectric region provide a new path for displacement currents which can be modeled by a capacitor in shunt with the serial RL dipole. In that case, a lumped element model is constituted, as shown on Fig. 2.3 which models the frequency behavior of the component with non frequency dependent elements. The impedance expression that is going to be studied next is then:

$$Z(\omega) = \frac{R + j \cdot \omega \cdot [L(1 - LC\omega^2) - R^2C]}{(1 - LC\omega^2)^2 + R^2C^2\omega^2} \quad (2.9)$$

The capacitive element beside the inductive element gives the dipoles its second order property: for $\omega_0 = 1/\sqrt{LC}$, a discontinuity can be observed in the impedance value that corresponds to the circuit resonance. The serial resonance frequency is then given by:

$$f_0 = \frac{1}{2\pi\sqrt{LC}} \quad (2.10)$$

As we consider that the RLC model is applied to an inductive component at low frequency, one can write:

- On one hand, that the imaginary part of the impedance of the RL dipole is much higher than its real part, *i.e.* $L\omega \gg R$.
- On the other hand, that from the two dipoles in shunt, L and C, the inductive one has the smallest impedance magnitude (*the inductive effect is more important than the capacitive one*), *i.e.* $\frac{1}{C\omega} \gg L\omega$.

We can thus deduce that $L \gg R^2C$, and then the expressions of $R_S(\omega)$ and $L_S(\omega)$ can be simplified by having $\alpha = \frac{R^2C}{L} \rightarrow 0$ appear:

$$R_S(\omega) = \frac{R}{1 - \left(2 - \frac{R^2 C}{L}\right) LC\omega^2 + (LC\omega^2)^2} = R \frac{1}{1 - (2 - \alpha) \left(\frac{f}{f_0}\right)^2 + \left(\frac{f}{f_0}\right)^4} \quad (2.11)$$

$$L_S(\omega) = \frac{L \left[\left(1 - \frac{R^2 C}{L}\right) - LC\omega^2 \right]}{1 - \left(2 - \frac{R^2 C}{L}\right) LC\omega^2 + (LC\omega^2)^2} = L \frac{(1 - \alpha) - \left(\frac{f}{f_0}\right)^2}{1 - (2 - \alpha) \left(\frac{f}{f_0}\right)^2 + \left(\frac{f}{f_0}\right)^4} \quad (2.12)$$

The resonance frequency is the validity limit of the model proposed in section 1. Generally, the inductor is used in the frequency range at least one decade below the resonance frequency. However, some applications can lead to its use at limits.

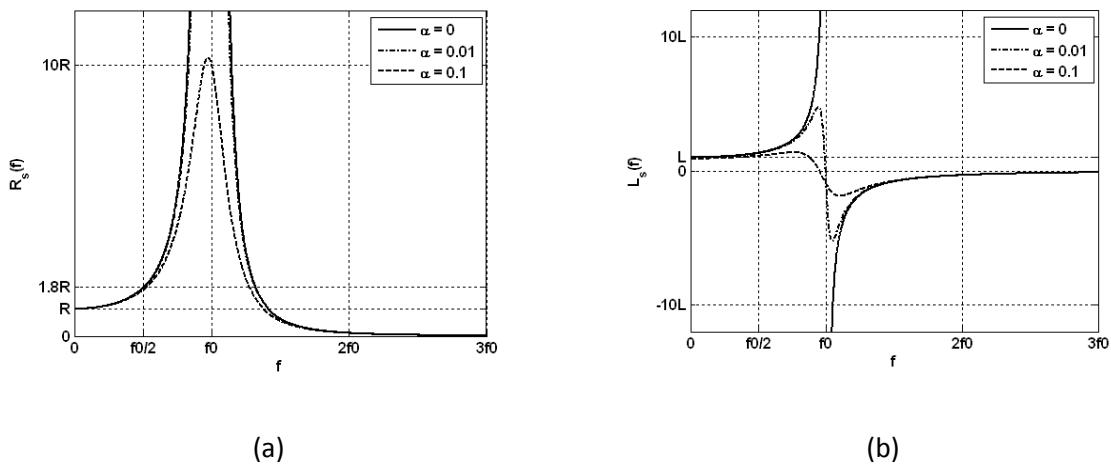


Fig. 2.4 - Normalized representation of real inductor equivalent resistance and inductance versus frequency

D - Skin and proximity effects

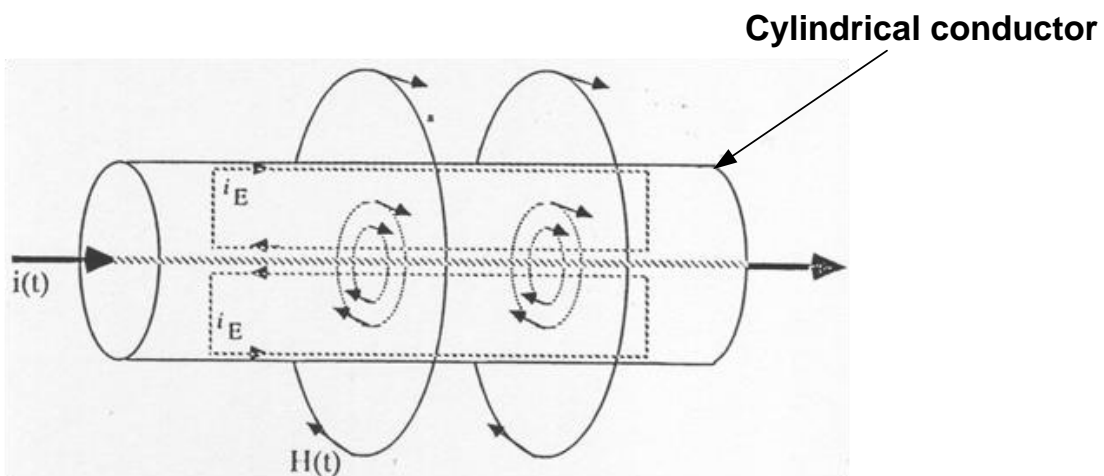


Fig. 2.5 - The skin effect origin: induced magnetic field H and current i_E inside a cylindrical conductor [Niknejad_thesis]

An alternative current $i(t)$ carried by a single conductor generates a magnetic excitation field $\mathbf{H}(t)$. This field is rotational around the current conduction path as shown on Fig. 2.5 and it is responsible for the induced current $i_E(t)$, called eddy current. Eddy currents obey to Lorentz principle and their direction is so that they partially cancel the magnetic field. They are collinear to the inducing current in the external region of conductors and anti-collinear in the internal region. This results in a crown of greater current density known as skin effect. The non homogeneous distribution of current density can be roughly modeled as an annulus of thickness δ , corresponding to the “skin depth” or penetration of current inside the conductor.

$$\delta = \sqrt{\frac{\rho}{\pi f \mu}} \tag{2.13}$$

where ρ is the resistivity of conductors, f the working frequency and μ the permeability of the environment media. The equivalent section of conductors thus decreases with frequency. The equivalent serial resistance is then greater in high frequency and active losses are increased too. One uses Litz wire (*multiconductor wire*) to prevent this parasitic effect.

The induction of Eddy currents also occurs between conductors and real current distribution depends on each conductor’s current. This global phenomenon is called proximity effect.

We have simulated the current density distribution in two infinite cylindrical conductors both excited by 1A. Fig. 2.6 shows the cross section response of such conductors, first separately excited ($1A, 0A$) and ($0A, 1A$), and then excited together ($1A, 1A$). On the excited conductor, the total current density is maximum and positive ($+J_{max}$) on the peripheral.

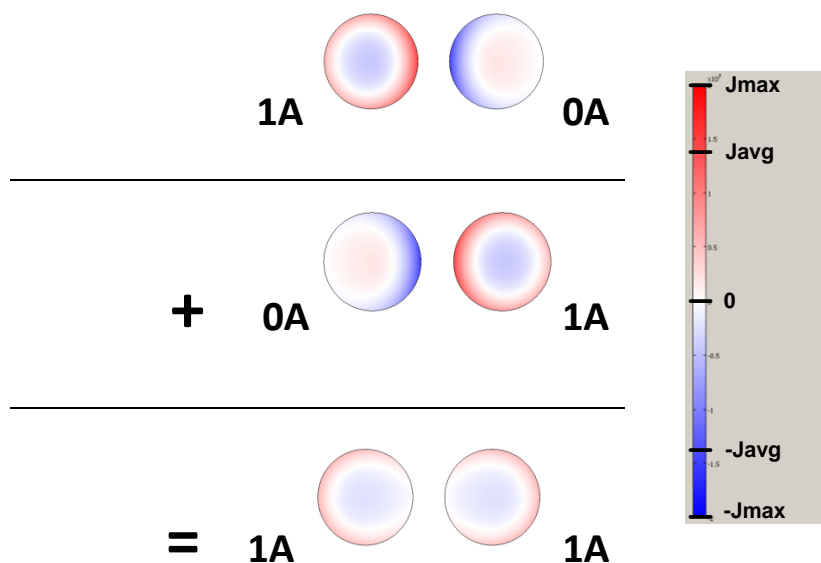


Fig. 2.6 - Skin and proximity effect inside two close infinite cylindrical conductors

The frequency response of an inductor with skin and proximity effects can be modeled by replacing the RL dipole by several coupled RL dipoles (*cf.* Fig. 2.6). Generally, two or three RL cells are sufficient, under the condition that an order reducing algorithm is used [Mei2003].

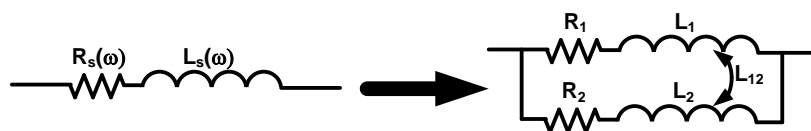


Fig. 2.7 - A way of representing skin and proximity effects with non frequency dependant lumped elements

E - Eddy currents

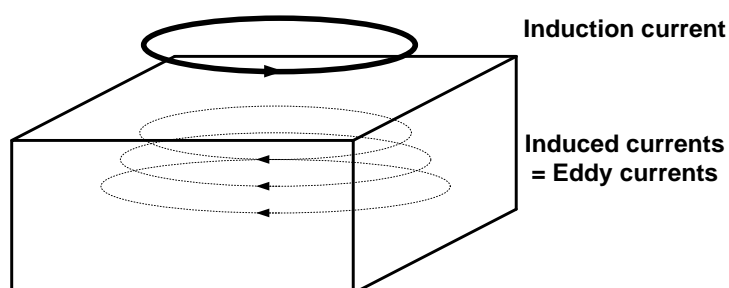


Fig. 2.8 - Substrate eddy currents

We have seen in previous part that induced currents in conductors are responsible for active losses by skin and proximity effects. When induced currents take place in a conductive media, they are referred as “eddy currents”. In discrete components, the main source of eddy current losses is magnetic cores when resistivity is not negligible or infinite. In integrated spiral inductors, designer must also model eddy current substrate losses.

This electromagnetic problem is complex and analytical approaches are generally imprecise. Actually, on one hand, the Finite Element Method approach requires huge meshing leading to very time-consuming solutions. On the other hand, analytical approaches are based on considerations over the symmetry of the problem. They are then devolved to simple problems, *i.e.* composed of basic geometrical shape conducting paths and substrates.

F - Hysteresis losses

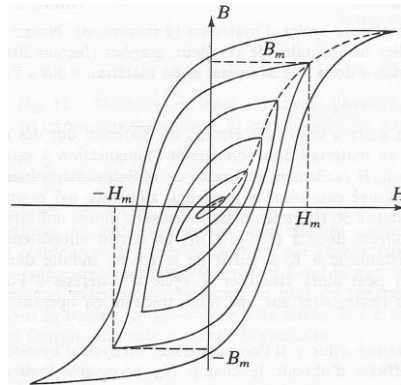


Fig. 2.9 - Hysteretic cycles of a ferromagnetic material under various excitations (various maximum magnetic fields H_m) [Leplus1986]

Magnetizing in ferromagnetic materials is not reversible. The $B=f(H)$ curve is in fact constituted of hysteresis cycles which area is proportional to the total energy consumed to run one cycle (*cf. Fig. 2.9*). When working frequency increases, dissipated power becomes consequent:

$$P = \frac{1}{T} \int u(t) \cdot i(t) \cdot dt = \frac{1}{T} \int_{\text{cycle}} HdB \quad (2.14)$$

This theoretical formula allows the calculus of hysteretic losses under the condition that the hysteretic cycle corresponding to the excitation is exactly known, *i.e.* the magnetic field is known at any time. It can be calculated from the voltage of the proper inductance L_p , which represents the inductive part of which magnetic flux density is inside the core (*cf Fig. 2.10.a*).

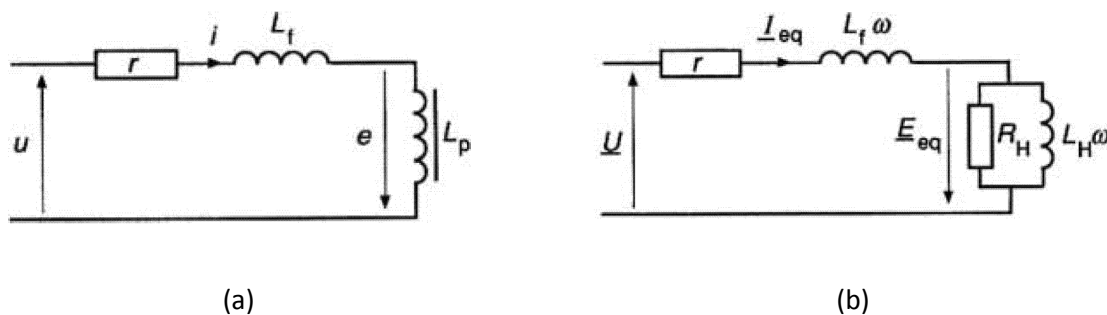


Fig. 2.10 - Ferromagnetic core coil. Nonlinear model (a) and linearized model (b) [Leplus1986]

This approach leads to a correct evaluation of losses when they are not important but, in fact, active losses introduced by hysteretic phenomenon must sometimes be taken into account in the electrical model to achieve good precision. Losses are important when using semi-soft ferromagnetic materials (the hysteretic cycle is larger than the one of soft materials) or when a big amount of

energy is stored inside the material instead of the air gap. This phenomenon is very complex because it is nonlinear.

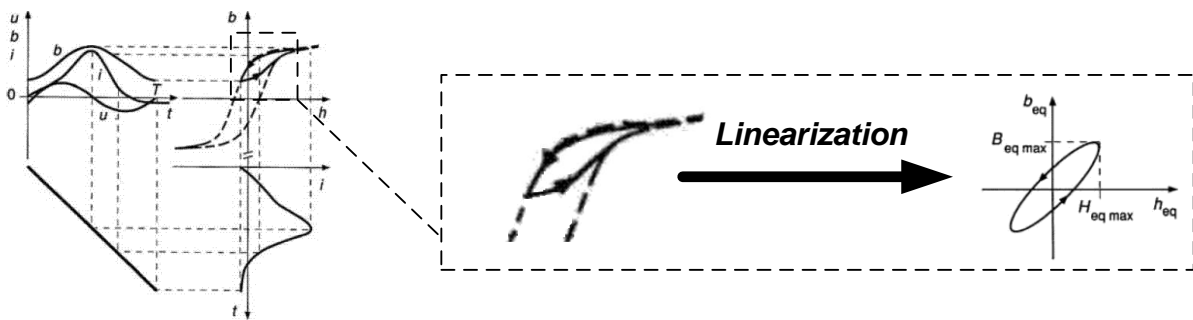


Fig. 2.11 - Linearization of hysteretic phenomenon at a bias point [Leplus1986]

One can linearize this phenomenon around a bias point, however. Fig. 2.11 shows how a mini hysteresis cycle can be approximated by an ellipsoid [Leplus1986]. Indeed, this kind of curve is described by linear equations relating B and H fields. This method corresponds to approximate voltages and currents for the proper inductance dipole sinusoidal signals with a phase difference. This way, the hysteretic behavior of the proper inductance can be modeled by a constant inductor L_H in shunt with a constant resistance R_H (cf. Fig. 2.10). Another way to represent this linearized phenomenon is the use of complex relative permeability $\mu_r = \mu_r' + i \cdot \mu_r''$.

4 - Two-port model

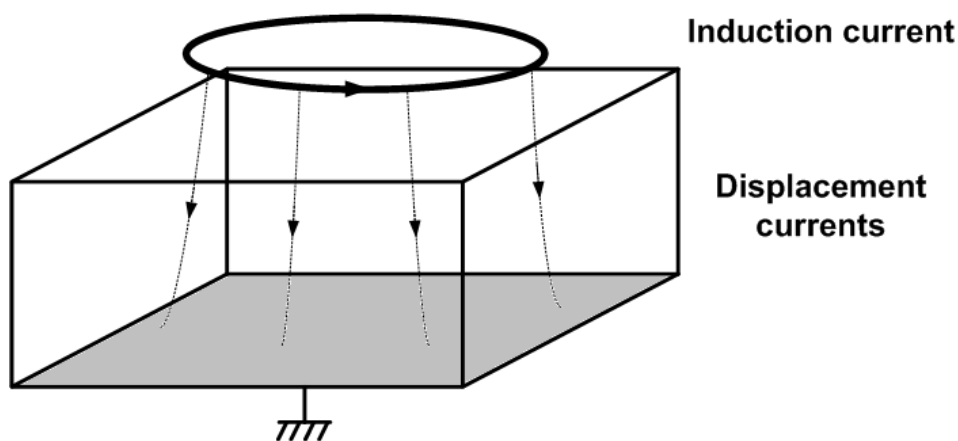


Fig. 2.12 - Displacement currents in the substrate

Radio-frequency (RF) approach of spiral integrated inductors generally considers that kind of device as microstrip structures. The characteristics of microstrip structures on semiconductor substrate, especially metal on oxide on silicon, have been investigated extensively [Yue2000, Burghartz2003]. Contrary to low frequency approaches where the zero isopotential is viewed as a

sphere of infinite radius, designers of radio-frequency devices consider a ground plane at the bottom of the substrate. This way, the environment is limited in space and models can be more precise, including common mode current losses. Those currents are called displacement currents as they result from capacitive effects that take place between conductors and ground plane. These capacitive effects can be modeled by lumped capacitors and resistances. On Fig. 2.13, we can see that each substrate layer is represented by a capacitor and a resistor when the layer's conductivity is not zero. Here, C_{ox} represents the oxide equivalent capacitance and the couple R_{Si} and C_{Si} represents the lossy capacitive effect of silicon.

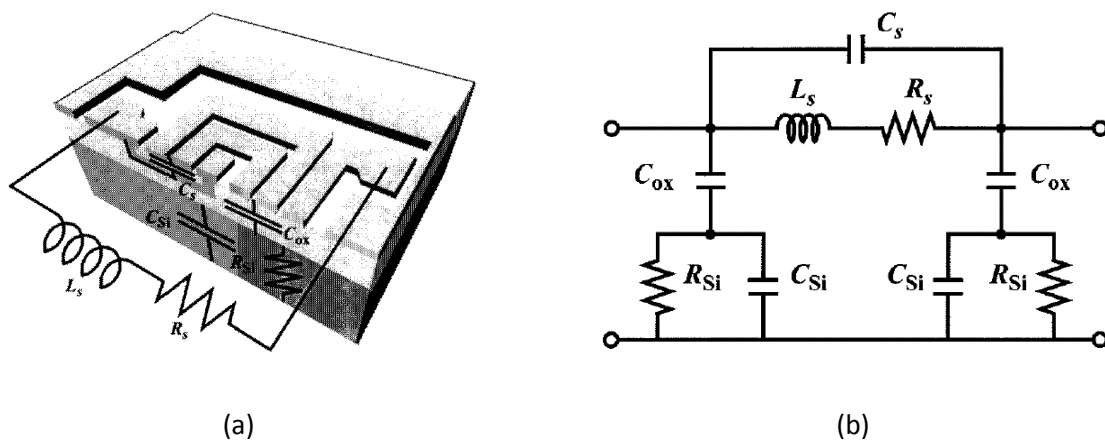


Fig. 2.13 - Two port model of a realistic inductor [Yue2000]

This structural model is the most commonly used non frequency dependant lumped element model. In the same manner as one-port model, one can define a generic impedance approach where each structural dipole is replaced by frequency-dependant impedance. The corresponding model is presented on Fig. 2.14.a. The representing of Z_A , Z_B and Z_C is useful to precisely show the behavior of each structural dipole (Z_A and Z_B capacitive and Z_C inductive). Furthermore, this impedance approach can be generalized by introducing matrix representation. Impedance matrix Z (cf. Fig. 2.14.b) is more appropriate to model low frequency phenomena as it involves voltage and current concepts. High frequency designers prefer S-parameters (cf. Fig. 2.14.c) matrix which is equivalent to Z-parameters matrix but uses reflected and transmitted power concepts instead [Combes_book, Combes2_book].

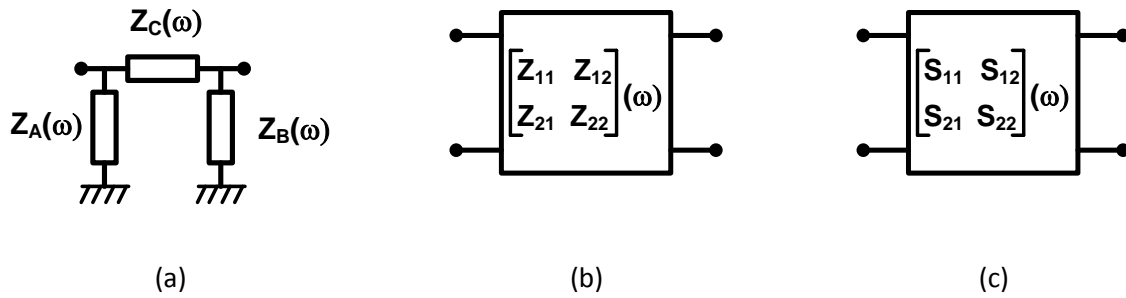


Fig. 2.14 - Frequency dependant two-port models of the inductor

5 - Conclusion

In this chapter, we presented the different electrical models available for designers when working on integrated inductors. We have seen that these models are based on electromagnetic interpretation of phenomena, especially parasitic phenomena responsible for electric losses. This study has led us to make choices for the standard representation we use for our components. We thus decided:

- to consider linear equations allowing the frequency approach (*non linear hysteretic phenomena can be linearized*)
- to consider voltage and current concepts, as usual for power electronics problems, even if we work with high frequency phenomena (*quasi-stationary regime or quasi-TEM mode*)

We also focused on the importance of the choice of the ground isopotential for a model. We will usually work with one-port models as ground plane at the bottom of the substrate would generate more losses, but our modelization will take the substrate conductivity and relative permittivity into account. The more generic way for representing an inductive behavior is the frequency response of the equivalent impedance of the dipole. Our goal in simulating, modeling and characterizing will then be the obtaining of $Z(f)$. One can use curve fitting or other regression methods to obtain lumped element models presented above. Modeling the frequency response of the impedance and extracting a non frequency dependant electrical model with few elements is actually a common way to integrate theoretical models of inductive components in the design flow of full power electronic systems.

Chapter 3

Circular spiral inductors PEEC modelization and FEM simulation

1 - Introduction

The design of inductive components, inductors or transformers, requires three complementary technical skills: a good understanding of physical phenomena taking place in the component, the ability of modeling and predicting its electrical behavior and an efficient intuitive approach of the topology optimization. The goal of the software tool SPIRALC developed in LAAS-CNRS is to provide a useful help to the designer based on those needs.

In this chapter, we present the developed formal model based on Partial Element Equivalent Circuit (*PEEC*) applied to circular spiral inductors and its implementation in a software tool SPIRALC [Artillan2007, Artillan2008]. This work proposes a new formalization of PEEC model for axisymmetric structure in quasistationary regime. Electromagnetic formulation is derived in the Mixed Potential Integral Equation (*MPIE*) and expressed in cylindrical coordinates. The conductive volume of the system is meshed and approximated by equivalent elements (*resistive and inductive coupled dipoles and capacitive coupled panels*). The whole equivalent electrical circuit is expressed in matrix formulation and several analytical of finite element methods for the calculation of matrices coefficients are proposed. Finally, the software implementation is reported: SPIRALC has been

SPIRALC approach for circular spiral inductors: cylindrical PEEC + quasistatic FEM simulations or analytic formulas

developed with coupled features of Matlab (*generalist matrix numerical calculus software environment*) and Comsol Multiphysics (*syntax compatible finite element method solver*).

Such an approach for modeling circular spiral inductors, or transformers, is much less computing time consuming than full finite element approach. It enables the calculation of the frequency response of a component from static regime to serial resonance frequency in a few minutes. This allows the optimizing of topologies with size and losses constraints for instance. The PEEC approach in general also provides a good way to understand each cause of losses in a component as it separates electric and magnetic effects. In a second section, we present the use of electromagnetic solvers Maxwell3D and HFSS from Ansoft Corp. We first justify the choice of these solvers among several others we evaluated. Then, we describe a simulation method to achieve precise simulation and, finally, we use the simulation results to validate our model.

2 - SPIRALC approach for circular spiral inductors: cylindrical PEEC + quasistatic FEM simulations or analytic formulas

A - Fundamentals and hypotheses

a - Maxwell's equations

The electromagnetic scheme of our work is based on Maxwell's equations which are declined in their local form and expressed in the Laplace domain as all the constitutive media are assumed to be linear:

$$\nabla \times \mathbf{E} = -s\mathbf{B} \quad (3.1)$$

$$\nabla \times \mathbf{H} = \mathbf{J}_c + s\mathbf{D} \quad (3.2)$$

$$\nabla \cdot \mathbf{D} = \rho \quad (3.3)$$

$$\nabla \cdot \mathbf{B} = 0 \quad (3.4)$$

where s is the generalized Laplace variable, \mathbf{H} the magnetizing field, \mathbf{E} the electric field, \mathbf{B} the magnetic flux density (also called magnetic field), \mathbf{D} the electric displacement field, ρ the volume charge density and \mathbf{J}_c the conduction current density. These equations are valid at any point of space.

Three medium-dependant parameters, called the constitutive constants of the medium, are also defined: the electric permittivity ε , the magnetic permeability μ and the electric conductivity σ . We consider linear, homogeneous and isotropic materials with instantaneous response to changes in

magnetizing and electric field. So these three constitutive constants are simply scalar values inside each material, and each material is entirely defined by their specific constitutive constants:

$$\mathbf{D} = \varepsilon \mathbf{E} \quad (3.5)$$

$$\mathbf{B} = \mu \mathbf{H} \quad (3.6)$$

$$\mathbf{J}_c = \sigma \mathbf{E} \quad (3.7)$$

Moreover, the displacement current density \mathbf{J}_d is defined as $\mathbf{J}_d = s\mathbf{D}$ and equation (3.2) can be rewritten as:

$$\nabla \times \mathbf{H} = \mathbf{J}_c + \mathbf{J}_d = \mathbf{J} \quad (3.8)$$

b - Magnetic and electric potentials

Magnetic vector potential

The magnetic vector potential \mathbf{A} is defined so that:

$$\mathbf{B} = \nabla \times \mathbf{A} \quad (3.9)$$

The magnetic vector potential is entirely defined as we consider the Coulomb's gauge:

$$\nabla \cdot \mathbf{A} = 0 \quad (3.10)$$

Since only low frequencies are considered, the magnetic vector potential \mathbf{A} is the solution of:

$$\nabla^2 \mathbf{A} = -\mu \mathbf{J} \quad (3.11)$$

Demonstration of (3.11):

Multiplying (3.8) by $\mu \Rightarrow \nabla \times \mu \mathbf{H} = \mu \mathbf{J}$

Introducing (3.6) in (3.9) $\Rightarrow \mu \mathbf{H} = \nabla \times \mathbf{A}$

Combining both the above equations $\Rightarrow \nabla \times (\nabla \times \mathbf{A}) = \mu \mathbf{J}$

Using an identity of differential operators $\Rightarrow \nabla(\nabla \cdot \mathbf{A}) - \nabla^2 \mathbf{A} = \mu \mathbf{J}$

Introducing Coulomb's gauge (3.10) in the previous equation $\Rightarrow -\nabla^2 \mathbf{A} = \mu \mathbf{J}$

Rewriting the previous equation $\Rightarrow \nabla^2 \mathbf{A} = -\mu \mathbf{J}$

Electric scalar potential

The electric scalar potential Φ is defined so that:

$$\mathbf{E} = -\nabla \Phi - s\mathbf{A} \quad (3.12)$$

Analogously, in low frequency domain, the scalar potential Φ can be calculated as the solution of a differential equation:

$$\nabla^2 \Phi = -\frac{\rho}{\varepsilon} \quad (3.13)$$

Demonstration of (3.13):

$$\text{Combining (3.3) and (3.5)} \Rightarrow \nabla \cdot (\varepsilon \mathbf{E}) = \rho$$

$$\text{Multiplying (3.12) by } \varepsilon \text{ and taking its divergence} \Rightarrow \varepsilon \nabla \cdot (-\nabla \Phi) = \varepsilon \nabla \cdot \mathbf{E} + s\varepsilon \nabla \cdot \mathbf{A}$$

$$\text{Using an identity of differential operators} \Rightarrow \varepsilon(-\nabla^2 \Phi) = \nabla \cdot (\varepsilon \mathbf{E}) + s\varepsilon \nabla \cdot \mathbf{A}$$

$$\text{Inserting Coulomb's gauge (3.10) and combining the first equation with the above equation} \Rightarrow \varepsilon(-\nabla^2 \Phi) = \rho$$

$$\text{Rewriting the previous equation} \Rightarrow \nabla^2 \Phi = -\frac{\rho}{\varepsilon}$$

c - Solving vector and scalar potentials

Definition of Green's functions

Equations (3.11) and (3.13) are equations of type:

$$\nabla^2 u(\mathbf{r}) = f(\mathbf{r}), \quad \mathbf{r} \in V \quad (3.14)$$

where V is a volume domain of the space ($V \subset \mathbb{R}^3$), $f(\mathbf{r})$ is an excitation function and $u(\mathbf{r})$ is the solution of the equation. Since we can apply superposition principle to this linear partial differential equation, we are going to use a Green's function $\mathcal{G}(\mathbf{r}|\mathbf{r}')$ to express its mathematical solution. As the Green's function satisfies all boundary conditions, the solution $u(\mathbf{r})$ expressed with $\mathcal{G}(\mathbf{r}|\mathbf{r}')$ will do so be unique, *i.e.* the Green's function contains all the information.

Thus, Green's function $\mathcal{G}(\mathbf{r}|\mathbf{r}')$ is the solution of the differential equation which right-hand member has been replaced by an elementary excitation $\delta(\mathbf{r} - \mathbf{r}')$ at a point of the space. Then, our Green's function can be found by solving:

$$\nabla^2 \mathcal{G}(\mathbf{r}|\mathbf{r}') = \delta(\mathbf{r} - \mathbf{r}'), \quad \mathbf{r} \in V \quad (3.15)$$

We can formally write the right-hand side of (3.14) as:

$$f(\mathbf{r}) = \int_{\mathbf{r}' \in V'} \delta(\mathbf{r} - \mathbf{r}') f(\mathbf{r}') dV', \quad \mathbf{r} \in V \quad (3.16)$$

If we multiply (3.15) by $f(\mathbf{r}')$, and integrate the result with respect to \mathbf{r}' over the volume V , we obtain:

$$\mathbf{u}(\mathbf{r}) = \int_{\mathbf{r}' \in V'} \mathcal{G}(\mathbf{r}|\mathbf{r}') \mathbf{f}(\mathbf{r}') dV' \quad (3.17)$$

In (3.14), if the function $\mathbf{u}(\mathbf{r})$ is a vector function, it can be demonstrated that in our case the following generalized expression is valid:

$$\mathbf{u}(\mathbf{r}) = \int_{\mathbf{r}' \in V'} \mathcal{G}(\mathbf{r}|\mathbf{r}') \mathbf{f}(\mathbf{r}') dV' \quad (3.18)$$

Use of Green's functions

Applying the Green's functions scheme, solutions of (3.11) and (3.13) can be expressed as:

$$\mathbf{A}(\mathbf{r}) = \int_{\mathbf{r}' \in V'} \mathcal{K}(\mathbf{r}|\mathbf{r}') \mathbf{J}(\mathbf{r}') dV' \quad (3.19)$$

$$\Phi(\mathbf{r}) = \int_{\mathbf{r}' \in V'} \mathcal{G}(\mathbf{r}|\mathbf{r}') \rho(\mathbf{r}') dV' \quad (3.20)$$

where $\mathcal{K}(\mathbf{r}|\mathbf{r}')$ and $\mathcal{G}(\mathbf{r}|\mathbf{r}')$ are both Green's functions which expression depends on media and boundary conditions.

For instance, in free space, the common expression of $\mathcal{K}(\mathbf{r}|\mathbf{r}')$ and $\mathcal{G}(\mathbf{r}|\mathbf{r}')$ are [Mattheij_book pp. 171-173]:

$$\mathcal{K}(\mathbf{r}|\mathbf{r}') = \mathcal{G}(\mathbf{r}|\mathbf{r}') = -\frac{1}{4\pi} \frac{1}{\|\mathbf{r} - \mathbf{r}'\|} \quad (3.21)$$

Demonstration of (3.21):

In free space, spherical symmetry converts (3.15) to an ordinary differential equation, where the only variable dependence is the distance $r \Rightarrow \nabla^2 \mathcal{G} = \frac{d^2 \mathcal{G}}{dr^2} + \frac{1}{r} \frac{d\mathcal{G}}{dr} = \delta(r)$

The general solution to the above equation is, for $r > 0 \Rightarrow \mathcal{G}(r) = \frac{A}{r} + B$, $(A, B) \in \mathbb{R}$

We may choose $\mathcal{G} \rightarrow 0$ when $r \rightarrow \infty$, that implies $B = 0$

To determine A, we define a ball $\mathcal{B}(\mathbf{0}; r)$ around $\mathbf{0}$ with radius r . From Gauss' theorem we can write \oint

$$\int_{\mathcal{B}(\mathbf{0}; r)} \nabla^2 \mathcal{G}(r) dV = \oint_{\partial \mathcal{B}(\mathbf{0}; r)} \frac{d\mathcal{G}(r)}{dr} dS$$

Since $\int_{\mathcal{B}(\mathbf{0}; r)} \nabla^2 \mathcal{G}(r) dV = 1$, we obtain $\oint_{\partial \mathcal{B}(\mathbf{0}; r)} \frac{d\mathcal{G}(r)}{dr} dS = 1$

That is to say $\oint_{\partial \mathcal{B}(\mathbf{0}; r)} \frac{-A}{r^2} dS = -4\pi A$

So in this case $\Rightarrow A = -\frac{1}{4\pi}$

And finally $\Rightarrow \mathcal{G}(\mathbf{r}|\mathbf{r}') = -\frac{1}{4\pi} \frac{1}{\|\mathbf{r} - \mathbf{r}'\|}$

In that case, (3.19) and (3.20) can be rewritten as:

$$\mathbf{A}(\mathbf{r}) = \frac{\mu}{4\pi} \int_{\mathbf{r}' \in V'} \frac{1}{\|\mathbf{r} - \mathbf{r}'\|} \mathbf{J}(\mathbf{r}') dV' \quad (3.22)$$

$$\Phi(\mathbf{r}) = \frac{1}{4\pi\epsilon} \int_{\mathbf{r}' \in V'} \frac{1}{\|\mathbf{r} - \mathbf{r}'\|} \rho(\mathbf{r}') dV' \quad (3.23)$$

It is important to notice that (3.22) and (3.23) are particular solutions, since $\mathcal{K}(\mathbf{r}|\mathbf{r}')$ and $\mathcal{G}(\mathbf{r}|\mathbf{r}')$ are particular solution of Green's functions in free space.

d - General hypotheses and domain of application of the model

Concentric rings approximation

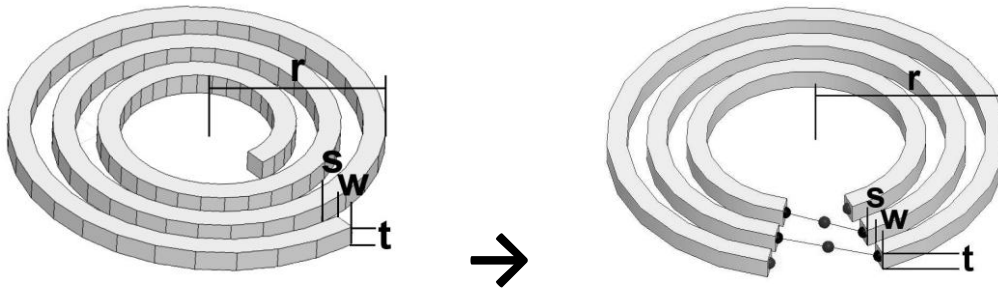


Fig. 3.1 - Concentric rings approximation of a spiral

In order to enable mathematical calculus, we are going to simplify the geometry of the spiral inductors. We will consider our spiral inductors geometry as a set of concentric rings with the same width w and the same spacing s between rings (*cf. Fig. 3.1*).

This approximation is fairly accurate even if the shape of the inductor deviates a lot from a serie of concentric annulus, in other words, if $s > w$ [Rejaei1998].

Negligible propagation time

We can consider that the dimensions of the system are small enough to neglect propagation times:

$$t' = t - \frac{\|\mathbf{r} - \mathbf{r}'\|}{c} \sqrt{\mu_r \epsilon_r} \approx t \quad (3.24)$$

where t is the time variable and c is the speed of light.

B - Magnetic, quasi-static approach

a - Hypotheses over the current density

Azimuthal current density

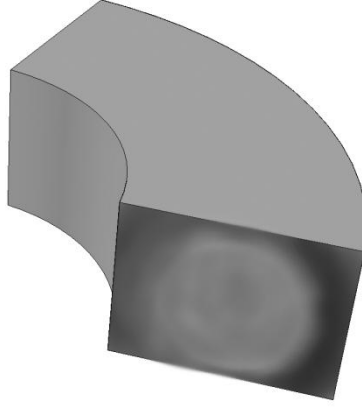


Fig. 3.2 - Azimuthal current density hypothesis

Due to the geometry of the system, we can formulate the hypothesis that the current density is azimuthal, *i.e.* along the “natural” circulating direction in conductors. Since we use a cylindrical coordinate system, we can write that the current density vector $\mathbf{J}(\mathbf{r})$ is collinear to the azimuthal vector (\mathbf{e}_θ component), whereas it will not be homogeneous in transversal sections (*cf.* Fig. 3.2).

Therefore, the current density vector $\mathbf{J}(\mathbf{r})$ can be expressed as:

$$\mathbf{J}(\mathbf{r}) = J(r, \theta, z)\mathbf{e}_\theta = J_\theta(r, \theta, z)\mathbf{e}_\theta \quad (3.25)$$

Thus, only the \mathbf{e}_θ component of the current density vector $\mathbf{J}(\mathbf{r})$ is not equal to zero, but it is *a priori*, r , θ and z dependant.

A conclusion of this hypothesis is that scalar potential Φ is constant over transversal sections. This can be demonstrated by inserting (3.7) and (3.19) into (3.12):

$$-\nabla\Phi = \frac{1}{\sigma}\mathbf{J}(\mathbf{r}) + s \int_{\mathbf{r}' \in V'} \mathcal{K}(\mathbf{r}|\mathbf{r}')\mathbf{J}(\mathbf{r}') dV' \quad (3.26)$$

and using the azimuthal $\mathbf{J}(\mathbf{r})$ hypothesis (3.25):

$$\begin{bmatrix} -\frac{\partial\Phi}{\partial r} \\ \frac{1}{r}\frac{\partial\Phi}{\partial\theta} \\ -\frac{\partial\Phi}{\partial z} \end{bmatrix} = \begin{bmatrix} 0 \\ \frac{1}{\sigma}J_{\theta}(r, \theta, z) + s \int_{\mathbf{r}' \in V'} \mathcal{K}(\mathbf{r}|\mathbf{r}')J_{\theta}(r', \theta', z')dV' \\ 0 \end{bmatrix} \quad (3.27)$$

$\nabla\Phi$ is then collinear to the azimuthal vector \mathbf{e}_{θ} (others components of $\nabla\Phi$ are 0). That means Φ transverse components (Φ_r and Φ_z) are constant over the section of a ring. Therefore, scalar potential in cylindrical coordinate system can be expressed as:

$$\Phi(\mathbf{r}) = \Phi(\theta) \quad (3.28)$$

Low frequency approximation

The hypothesis that we work at low frequencies makes current density vector $J_{\theta}(r, \theta, z)\mathbf{e}_{\theta}$ not θ dependant. Even if skin effect happens inside the conductor, current distribution is considered uniform for any θ value. And it can then be written as:

$$J_{\theta}(\mathbf{r}) = J_{\theta}(r, z) \quad (3.29)$$

b - Magnetostatic general formulation

Using the $\Phi(\mathbf{r})$ expression given by (3.28) and the $J_{\theta}(\mathbf{r})$ expression given by (3.29), we can write the θ component of equation (3.27) as:

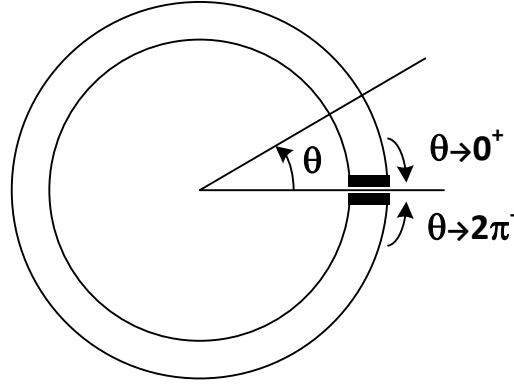
$$-\frac{1}{r}\frac{d\Phi(\theta)}{d\theta} = \frac{1}{\sigma}J_{\theta}(r, z) + s \int_{\mathbf{r}' \in V'} \mathcal{K}(\mathbf{r}|\mathbf{r}')J_{\theta}(r', z')dV' \quad (3.30)$$

c - Volume discretizing and equivalent impedance definition

In order to define equivalent impedances, we are going to mesh the conductors into a number d of separate volumes, which we will call dipoles:

$$-\frac{1}{r}\frac{d\Phi_i^d(\theta)}{d\theta} = \frac{1}{\sigma}J_{\theta}(r, z) + s \sum_{k=1}^d \int_{\mathbf{r}' \in V'_k} \mathcal{K}(\mathbf{r}|\mathbf{r}')J_{\theta}(r', z')dV'_k \quad (3.31)$$

where Φ_i^d , is the potential distribution inside the i^{th} dipole.


 Fig. 3.3 - Definition of electrodes on a ring by its θ coordinate

We excite the rings with a homogeneous potential over the first cross section $\theta \rightarrow 0^+$ with a potential Φ_i^{d+} for the input and the second cross section $\theta \rightarrow 2\pi^-$ with a potential Φ_i^{d-} for the output (cf. Fig. 3.3).

We introduce these definitions:

$$(\forall i \in \{1, \dots, d\}) \quad \Phi_i^{d+} = \lim_{\theta \rightarrow 0^+} \Phi_i^d(\theta) \quad (3.32)$$

$$(\forall i \in \{1, \dots, d\}) \quad \Phi_i^{d-} = \lim_{\theta \rightarrow 2\pi^-} \Phi_i^d(\theta) \quad (3.33)$$

$$(\forall i \in \{1, \dots, d\}) \quad U_i = \Phi_i^{d+} - \Phi_i^{d-} \quad (3.34)$$

$$(\forall i \in \{1, \dots, d\}) \quad I_i = \int_{z=z_{i1}}^{z_{i2}} \int_{r=r_{i1}}^{r_{i2}} J_\theta(r, z) dr dz \quad (3.35)$$

If we divide (3.31) by the i^{th} dipole's section area $S_i = w_i \cdot t_i = (r_{i2} - r_{i1}) \cdot (z_{i2} - z_{i1})$ and integrate over the variables ranges $(r, \theta, z) \in [r_1, r_2] \times [0, 2\pi] \times [z_1, z_2]$, we obtain:

$$\begin{aligned} & \frac{\ln\left(\frac{r_{i2}}{r_{i1}}\right)}{w_i} [\Phi_i^{d+} - \Phi_i^{d-}] \\ &= \frac{2\pi}{w_i t_i \sigma} \int_{z=z_{i1}}^{z_{i2}} \int_{r=r_{i1}}^{r_{i2}} J_\theta(r, z) dr dz \\ &+ \frac{1}{w_i t_i} s \sum_{k=1}^d \int_{z=z_{i1}}^{z_{i2}} \int_{\theta=0}^{2\pi} \int_{r=r_{i1}}^{r_{i2}} \int_{r' \in V'_k} \mathcal{K}(\mathbf{r}|\mathbf{r}') J_\theta(r', z') dV'_k dr d\theta dz \end{aligned} \quad (3.36)$$

Demonstration of (3.36):

Division by section and integration of (3.31) \Downarrow

$$\begin{aligned} & \frac{1}{w_i t_i} \int_{z=z_{i1}}^{z_{i2}} \int_{\theta=0}^{2\pi} \int_{r=r_{i1}}^{r_{i2}} -\frac{1}{r} \frac{d\Phi_i^d(\theta)}{d\theta} dr d\theta dz = \\ & \frac{1}{w_i t_i} \int_{z=z_{i1}}^{z_{i2}} \int_{\theta=0}^{2\pi} \int_{r=r_{i1}}^{r_{i2}} \left[\frac{1}{\sigma} J_\theta(r, z) + s \sum_{k=1}^d \int_{r' \in V'_k} \mathcal{K}(\mathbf{r}|\mathbf{r}') J_\theta(r', z') dV'_k \right] dr d\theta dz \end{aligned}$$

$$\text{Solving integrals } \oint - \frac{1}{w_i t_i} [\ln(r)]_{z_{i1}}^{z_{i2}} [\Phi_i^d(\theta)]_0^{2\pi} [z]_{r_{i1}}^{r_{i2}} = \frac{1}{w_i t_i \sigma} [\theta]_0^{2\pi} \int_{z=z_{i1}}^{z_{i2}} \int_{r=r_{i1}}^{r_{i2}} J_\theta(r, z) dr dz + \frac{1}{w_i t_i} s \sum_{k=1}^d \int_{z=z_{i1}}^{z_{i2}} \int_{\theta=0}^{2\pi} \int_{r=r_{i1}}^{r_{i2}} \int_{r' \in V'_k} \mathcal{K}(\mathbf{r}|\mathbf{r}') J_\theta(r', z') dV'_k dr d\theta dz$$

Then, above equation becomes \oint

$$\frac{\ln\left(\frac{r_{i2}}{r_{i1}}\right)}{w_i} [\Phi_i^{d+} - \Phi_i^{d-}] = \frac{2\pi}{w_i t_i \sigma} \int_{z=z_{i1}}^{z_{i2}} \int_{r=r_{i1}}^{r_{i2}} J_\theta(r, z) dr dz + \frac{1}{w_i t_i} s \sum_{k=1}^d \int_{z=z_{i1}}^{z_{i2}} \int_{\theta=0}^{2\pi} \int_{r=r_{i1}}^{r_{i2}} \int_{r' \in V'_k} \mathcal{K}(\mathbf{r}|\mathbf{r}') J_\theta(r', z') dV'_k dr d\theta dz$$

Equation (3.36) enables the i^{th} dipole voltage to be expressed as a linear combination of the k^{th} dipole intensity respectively defined in (3.34) and (3.35). To do this, we are going to multiply and divide the last term of (3.36) by I_k :

$$U_i = \left[\frac{2\pi}{\ln\left(\frac{r_{i2}}{r_{i1}}\right) t_i \sigma} \delta_{ik} + \frac{s}{\ln\left(\frac{r_{i2}}{r_{i1}}\right) t_i} \sum_{k=1}^d \frac{\int_{z=z_{i1}}^{z_{i2}} \int_{\theta=0}^{2\pi} \int_{r=r_{i1}}^{r_{i2}} \int_{r' \in V'_k} \mathcal{K}(\mathbf{r}|\mathbf{r}') J_\theta(r', z') dV'_k dr d\theta dz}{\int_{z=z_{k1}}^{z_{k2}} \int_{r=r_{k1}}^{r_{k2}} J_\theta(r, z) dr dz} \right] I_k \quad (3.37)$$

Where δ_{ik} is the Kronecker symbol which value is 1 when $i = k$ and 0 otherwise.

d - Properties and identifications

Impedance matrix identification

Equation (3.37) can be rewritten as:

$$U_i = \sum_{k=1}^d Z_{ik} I_k \quad (3.38)$$

Again, in matrix formulation:

$$\mathbf{U} = \mathbf{Z} \mathbf{I} \quad (3.39)$$

By identification in (3.37), one can define the impedances Z_{ik} as:

$$\forall (i, k), \quad Z_{ik} = R_{ik}^{\text{DC}} + sL_{ik}^{\text{AC}} \quad (3.40)$$

With the resistance value at low frequencies R_{ik}^{DC} :

$$R_{ik}^{\text{DC}} = \frac{2\pi}{\ln\left(\frac{r_{i2}}{r_{i1}}\right) t_i \sigma} \delta_{ik} \quad (3.41)$$

And L_{ik}^{AC} , when $i = k$, is the partial self-inductance L_{ii} of the i^{th} dipole, and when $i \neq k$, the mutual inductance L_{ik} between the i^{th} and the k^{th} dipoles:

$$L_{ik}^{AC} = \frac{1}{\ln\left(\frac{r_{i2}}{r_{i1}}\right) t_i} \frac{\int_{z=z_{i1}}^{z_{i2}} \int_{\theta=\theta_{i1}}^{\theta_{i2}} \int_{r=r_{i1}}^{r_{i2}} \int_{r' \in V_k'} \mathcal{K}(\mathbf{r}|\mathbf{r}') J_{\theta}(r', z') dV_k' dr d\theta dz}{\int_{z=z_{k1}}^{z_{k2}} \int_{r=r_{k1}}^{r_{k2}} J_{\theta}(r, z) dr dz} \quad (3.42)$$

The value R_{ii}^{DC} corresponds to the DC resistance of the i^{th} dipole. L_{ik}^{AC} is a term homogeneous to an inductance, its value depends on the current density distribution $J_{\theta}(r, z)$, which means it is a function of frequency. At low frequencies, J_{θ} is in phase with the excitation U_i and L_{ik}^{AC} is real. But in general case, it is a complex value. Then, the values of the apparent resistances R_{ik} and inductances L_{ik} are:

$$R_{ik} = R_{ik}^{DC} + \frac{\text{Im}[L_{ik}^{AC}]}{2\pi f} \quad (3.43)$$

$$L_{ik} = \text{Re}[L_{ik}^{AC}] \quad (3.44)$$

The general expression of the impedance depends on J_{θ} which is, in turn, depending on the excitations U_i . It is then impossible to give a generic simplified expression of the impedance, however, we'll see in next part that some approximations or linearizations can lead to much more simple expressions.

Admittance matrix

The admittance matrix is simply defined as:

$$\mathbf{Y}(f) = [\mathbf{Z}(f)]^{-1} \quad (3.45)$$

It verifies:

$$\mathbf{I}_i = \sum_{k=1}^d \mathbf{Y}_{ik} \mathbf{U}_k \quad (3.46)$$

That is, in matrix form:

$$\mathbf{I} = \mathbf{YU} \quad (3.47)$$

C - Electric, quasi-static approach

a - Charge density

Surface charge density hypothesis



Fig. 3.4 – Surface charge density hypothesis

The total volume charge density ρ will be located at conductor surface. This can be demonstrated in all conductors, whether a current goes through or not. We can define the surface charge density ρ_s to represent this charge distribution over the surface of conductors:

$$\rho_s = \frac{dQ}{dS} \quad (3.48)$$

where dQ is the elementary charge carried by a surface element dS .

As charge distribution is surface based, volume integral equation (3.20) can then be simplified to a surface integral:

$$\int_{\mathbf{r}' \in V'} \mathcal{G}(\mathbf{r}|\mathbf{r}') \rho(\mathbf{r}') dV' = \int_{\mathbf{r}' \in S'} \mathcal{G}(\mathbf{r}|\mathbf{r}') dQ'(\mathbf{r}') = \int_{\mathbf{r}' \in S'} \mathcal{G}(\mathbf{r}|\mathbf{r}') \rho_s(\mathbf{r}') dS' \quad (3.49)$$

Demonstration of (3.49):

From equation (3.7) $\Rightarrow \mathbf{J}_c = \sigma \mathbf{E}$

If the conductor has a conductivity $\sigma \rightarrow \infty \Rightarrow \mathbf{E} = 0, \mathbf{r} \in V$

According to Gauss' law $\Rightarrow \oint_S \mathbf{E} \cdot d\mathbf{S} = \frac{q_o}{\epsilon_0}$, where q_o is the charge inside the closed surface S

Then, since $0 = \frac{q_o}{\epsilon_0}$ for all closed surfaces inside of the charged conductor $\Rightarrow q_o = 0$

Then, necessarily, all the charge must be located at the surface of the conductor

This hypothesis is justified since the conductors have a big value of σ

b - Electrostatic general formulation

Inserting (3.48) in (3.49) and rewriting (3.20) leads to:

$$\Phi(\mathbf{r}) = \int_{\mathbf{r}' \in S'} \mathcal{G}(\mathbf{r}|\mathbf{r}') \rho_s(\mathbf{r}') dS' \quad (3.50)$$

The Green's function $\mathcal{G}(\mathbf{r}|\mathbf{r}')$ contains all the information about the media and boundary conditions, and then, the scalar potential $\Phi(\mathbf{r})$ is entirely defined.

c - Surface discretizing and equivalent capacitance definition

Since all the charges are on the surface of the conductors, we are going to mesh their surface into a number p of smaller surfaces that we are going to call panels.

We define the scalar potential Φ_i^p as the average value of the continuous scalar potential Φ over the i^{th} panel S_i :

$$\Phi_i^p = \frac{1}{S_i} \int_{\mathbf{r} \in S_i} \Phi(\mathbf{r}) dS_i \quad (3.51)$$

Inserting Φ from (3.50), and discretizing, results in:

$$\Phi_i^p = \sum_{k=1}^p \frac{1}{S_i} \int_{\mathbf{r} \in S_i} \int_{\mathbf{r}' \in S'_k} \mathcal{G}(\mathbf{r}|\mathbf{r}') \rho_s(\mathbf{r}') dS'_k dS_i \quad (3.52)$$

If we define the total charge of each panel Q_i^p :

$$Q_i^p = \int_{\mathbf{r} \in S_i} \rho_s(\mathbf{r}) dS_i \quad (3.53)$$

And if we multiply and divide (3.52) by (3.53), we finally obtain:

$$\Phi_i^p = \sum_{k=1}^p \frac{1}{S_i} \cdot \frac{\int_{\mathbf{r} \in S_i} \int_{\mathbf{r}' \in S'_k} \mathcal{G}(\mathbf{r}|\mathbf{r}') \rho_s(\mathbf{r}') dS'_k dS_i}{\int_{\mathbf{r} \in S_k} \rho_s(\mathbf{r}) dS_k} Q_k^p \quad (3.54)$$

Then, one can identify P_{ik} as:

$$P_{ik} = \frac{1}{S_i} \cdot \frac{\int_{\mathbf{r} \in S_i} \int_{\mathbf{r}' \in S'_k} \mathcal{G}(\mathbf{r}|\mathbf{r}') \rho_s(\mathbf{r}') dS'_k dS_i}{\int_{\mathbf{r} \in S_k} \rho_s(\mathbf{r}) dS_k} \quad (3.55)$$

This expression is almost the dual of Z_{ik} defined in the magnetostatic part. Analogously, (3.55) can be expressed as:

$$\Phi_i^p = \sum_{k=1}^p P_{ik} Q_k^p \quad (3.56)$$

Again, in matrix formulation, the scalar potential on each panel is given by the vector Φ^p :

$$\Phi^p = \mathbf{P} \mathbf{Q}^p \quad (3.57)$$

Where, according to electrostatic equations, \mathbf{P} is the potential coefficient square matrix and \mathbf{Q}^p the electric charges vector, which is the integral of the surface charge density over each panel surface (3.53).

We are going to work with the capacitance matrix \mathbf{C} , defined as the inverse of \mathbf{P} :

$$\mathbf{C} = \mathbf{P}^{-1} \quad (3.58)$$

By definition, the inversion of \mathbf{P} is available under the condition that the matrix is not singular, *i.e.* its determinant is not zero. Let's demonstrate that it is always true in the case of only 2 panels. This result can be generalized to the case of p panels. If we consider the hypothesis that P_{ik} only depends on the geometry because the charge density distribution is linearly related to the excitation, the value of each P_{ik} can be calculated by the method of separate excitations. Considering two conductors of respective charges Q_1 and Q_2 , and potentials Φ_1 and Φ_2 , we obtain from equation (3.57):

$$P_{11} = \frac{\Phi_1}{Q_1|_{Q_2=0}} \quad (3.59)$$

$$P_{21} = \frac{\Phi_2}{Q_1|_{Q_2=0}} \quad (3.60)$$

If, arbitrarily, $Q_1 > 0$ then $\Phi_1 > 0$ and consequently $P_{11} > 0$. Moreover, since Φ_2 is not a maximum or a minimum of the potential function, it comes that $0 < \Phi_2 < \Phi_1$. And then, $0 < P_{21} < P_{11}$. In the same manner, it can be demonstrated that $0 < P_{12} < P_{22}$. Finally, we can write $P_{11}P_{22} > P_{12}P_{21}$, so the determinant Δ of \mathbf{P} is strictly positive:

$$\Delta = P_{11}P_{22} - P_{12}P_{21} > 0 \quad (3.61)$$

As the determinant Δ is never equal to zero, the matrix $\mathbf{C} = \mathbf{P}^{-1}$ is defined. The on diagonal coefficients are called the capacitance coefficients and the off diagonal coefficients are called the influence coefficients. Furthermore, each panel can be viewed as half a capacitor. Any couple of panels is a full capacitor. As panels are not in total influence, those structural capacitors values are called partial capacitances, which are accessible from the capacitance matrix. There are two kinds of partial capacitances: panel-to-panel capacitances $C_{p_i p_k}$ given by equation (3.62) and panel-to-ground capacitances $C_{p_i G}$ given by equation (3.63):

$$C_{p_i p_k} = -C_{ik} \quad (3.62)$$

$$C_{p_i G} = \sum_{i=1}^p C_{ik} \quad (3.63)$$

D - Linear circuit model

a - Incidence matrices definition

In order to give a formal representation of the equivalent circuit constituted by “partial elements”, dipoles or panels, and by the terminals, we define three incidence matrices that relate those elements to the electrical nodes.

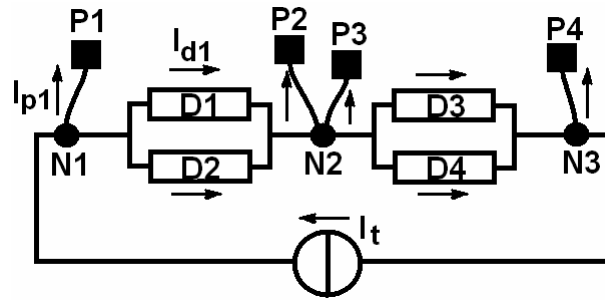


Fig. 3.5 - An example of equivalent circuit associated to the system

Dipoles to nodes (D2N)

This matrix links the dipoles to the nodes. Each line corresponds to a dipole and each column to a node. Every coefficient is 0, except for each dipole, the input node that is affected with “1” and the output node that is affected with “-1”. There is an exception to this: grounded nodes (*generally the low potential node of each terminal*) aren’t represented at all because their potential is known (0V) and there is no need to include them in the unknowns of the system of equations.

Panels to nodes (P2N)

This matrix links the panels to the nodes. Each line corresponds to a panel and each column to a node. Every coefficient is 0, except for each panel, the node they are connected to is affected with “1”. The grounded nodes aren’t represented in this matrix too.

Terminals to nodes (T2N)

Finally, this third matrix links terminals to nodes. Each line corresponds to a terminal and each column to a node. Every coefficient is 0, except for each dipole, the input node that is affected with “1” and the output node that is affected with “-1”. The grounded nodes aren’t represented in this matrix too.

For the sake of clarity, we are going to give an example of the construction of D2N, P2N and T2N matrices corresponding to the Partial Equivalent Element Circuit described by Fig. 3.5:

$$D2N = \begin{bmatrix} 1 & -1 \\ 1 & -1 \\ 0 & 1 \\ 0 & 1 \end{bmatrix} \quad (3.64)$$

$$P2N = \begin{bmatrix} 1 & 0 \\ 0 & 1 \\ 0 & 1 \\ 0 & 0 \end{bmatrix} \quad (3.65)$$

$$T2N = [1 \quad 0] \quad (3.66)$$

b - Linear circuit representation

Once the electrical potentials of the system have been aggregated to average potentials listed in vectors Φ^d , Φ^p and Φ^t for dipoles, panels and terminals, we can link them to the node potentials and then reconstitute an equivalent linear circuit with dipoles representing magnetic behavior, panels for electrical behavior and terminals as a way to define excitations.

We are going to define the voltages of dipoles U_i^d , panels U_i^p and terminals U_i^t as:

$$U_i^d = \Phi_i^{d+} - \Phi_i^{d-} \quad (3.67)$$

$$U_i^p = \Phi_i^p \quad (3.68)$$

$$U_i^t = \Phi_i^{t+} - \Phi_i^{t-} \quad (3.69)$$

Applying the D2N, P2N and T2N matrix definitions, the above potential differences can be expressed as follows:

$$\mathbf{U}^d = \mathbf{D2N}\Phi^n \quad (3.70)$$

$$\mathbf{U}^p = \mathbf{P2N}\Phi^n \quad (3.71)$$

$$\mathbf{U}^t = \mathbf{T2N}\Phi^n \quad (3.72)$$

The vector of the charges carried by each panel is defined as:

$$\mathbf{Q}^p = \mathbf{C} \cdot \mathbf{P2N}\Phi^n \quad (3.73)$$

The intensity through panels \mathbf{I}^p can thus be written as:

$$\mathbf{I}^p = j2\pi f \mathbf{Q}^p = j2\pi f \mathbf{C} \cdot \mathbf{P2N}\Phi^n \quad (3.74)$$

The intensity through dipoles \mathbf{I}^d can be written as:

$$\mathbf{I}^d = \mathbf{Y} \cdot \mathbf{D2N}\Phi^n \quad (3.75)$$

The total current in nodes can be expressed as the sum of currents through dipoles \mathbf{I}^d and panels \mathbf{I}^p produced by the excitation currents at terminals \mathbf{I}^t . Applying Kirchhoff's law, *i.e.* the sum of all currents at any node is equal to zero, we can write:

$$\mathbf{0} = \mathbf{D2N}^T \cdot \mathbf{I}^d + \mathbf{P2N}^T \cdot \mathbf{I}^p - \mathbf{T2N}^T \cdot \mathbf{I}^t \quad (3.76)$$

And reorganizing the above equation:

$$\mathbf{D2N}^T \cdot \mathbf{I}^d + \mathbf{P2N}^T \cdot \mathbf{I}^p = \mathbf{T2N}^T \cdot \mathbf{I}^t \quad (3.77)$$

Therefore, we can write the fundamental linear system of equations ruling the node potentials Φ^n in matrix form:

$$[\mathbf{D2N}^T \cdot \mathbf{Y} \cdot \mathbf{D2N} + \mathbf{P2N}^T \cdot \mathbf{j}2\pi f \cdot \mathbf{C} \cdot \mathbf{P2N}] \Phi^n = \mathbf{T2N}^T \cdot \mathbf{I}^t \quad (3.78)$$

Finding the solution of (3.78), we finally obtain:

$$\Phi^n = [\mathbf{D2N}^T \cdot \mathbf{Y} \cdot \mathbf{D2N} + \mathbf{P2N}^T \cdot \mathbf{j}2\pi f \cdot \mathbf{C} \cdot \mathbf{P2N}]^{-1} \mathbf{T2N}^T \cdot \mathbf{I}^t \quad (3.79)$$

The currents and charges can still be calculated from the potentials with equations (3.73)-(3.75) if needed; however, this is not useful for the single calculus of the frequency response of the device.

E - Partial elements calculus by analytical method

Our spiral inductors have been approximated with concentric rings and a mathematical scheme has been developed to formulate the electromagnetic coupling between each element. The partial elements model described in the above part consists in an equivalent circuit composed of partial resistances, inductances and capacitances.

The main formulation is given by generic equations (3.41) for resistances, (3.42) for inductances and (3.55)-(3.58) for capacitances. The calculus of the partial coefficients R, L and C can be performed by several methods.

An analytical approach is possible since, in some cases, we can consider filiform conductors and in other cases, a homogeneous charge or current density on conductors.

As in general case, charge and current densities are not homogeneous in the volume and over the surface of conductors, we are going to mesh them in an appropriate manner. Therefore, in small portions, different approximations can be done in order to obtain analytical expressions.

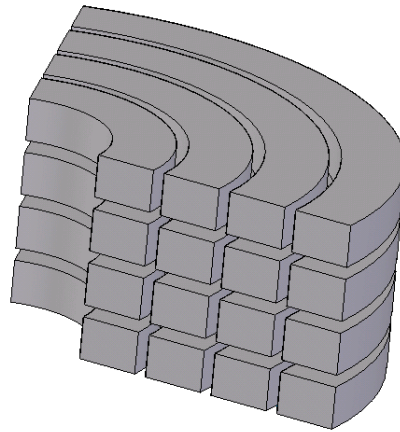


Fig. 3.6 - Volume mesh: dipoles

In Fig. 3.6, we mesh the whole volume in smaller rings which will constitute the dipoles.

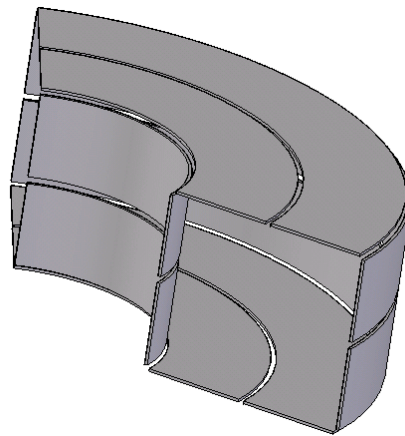


Fig. 3.7 - Surface mesh: panels

In Fig. 3.7, we split each face of conductor into two surface meshes. With this type of mesh, we can modelize the charge distribution variations over each face.

It is important to notice that this meshing will take skin and proximity effects into account, even if the current density is considered homogeneous or quasi-homogeneous in each mesh, because the magnetic coupling between each dipole pairs represented by the inductive part of the coupling matrix is the electrical point of view of those electromagnetic phenomena [Mei2003].

a - Resistance

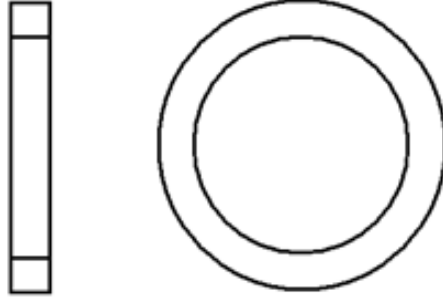


Fig. 3.8 – An annulus of rectangular cross section

As enounced in magnetic quasi-static part, the expression (3.41) gives the value of the DC resistance of an annulus with rectangular cross section (*cf. Fig. 3.8*). This value must not be confused with the total resistance given by (3.43), which corresponds to the resistive part of the impedance at a specific frequency. Here, we suppose that each dipole has a cross section small enough to consider that the current density is homogeneous over it, and then, the resistance value is calculated only once in DC conditions. For the sake of completeness, we propose a demonstration of the analytical formula of the resistance:

$$R = \frac{2\pi}{\sigma \cdot \ln\left(\frac{r_2}{r_1}\right) \cdot t} \quad (3.80)$$

where σ is the conductivity of the material and t , r_1 and r_2 are respectively the thickness (*not the time variable as listed in symbol table*), the internal radius and external radius of the annulus.

Demonstration of (3.80):

$$\text{No charges inside conductors} \Rightarrow \nabla^2 \Phi = 0$$

$$\text{In cylindrical coordinates, with } \Phi \text{ only } \theta \text{ dependent} \Rightarrow \nabla^2 \Phi = \frac{1}{r^2} \frac{\partial^2 \Phi}{\partial \theta^2} = 0$$

Then, a solution Φ can be found if we define U as the potential difference between the cross sections (=boundary conditions for $\theta \rightarrow 0^+$ and $\theta \rightarrow 2\pi^-$) $\Rightarrow \Phi = -\frac{\theta}{2\pi} U$

$$\text{Deducing the electric field by } \mathbf{E} = -\nabla \Phi \Rightarrow \mathbf{E} = E_\theta \mathbf{e}_\theta \text{ and } E_\theta = -\frac{1}{r} \frac{\partial \Phi}{\partial \theta} = \frac{U}{2\pi r}$$

$$\text{Finally, expressing the intensity } I = \int_S \sigma E_\theta dS \text{ in function of } U \Rightarrow I = \frac{\ln\left(\frac{r_2}{r_1}\right) (z_2 - z_1) \sigma}{2\pi} U$$

$$\text{By definition, the resistance is } R = \frac{U}{I} \Rightarrow R = \frac{2\pi}{\ln\left(\frac{r_2}{r_1}\right) t \sigma}$$

b - Inductance

The inductance formula (3.42) demonstrated in the magnetic quasi-static part is not directly applicable because it involves integral computation over the current density, that is, a priori, unknown. Furthermore, even if the hypothesis of homogeneous current density is formulated, it is

pretty much more efficient to use approximated formulas of the multiple integrals. We present here some approximated formulas, adapted to the topologies studied, which have proved their efficiency in terms of accuracy and computing time.

Self inductance

The inductance of circular coils of rectangular cross section (*cf. Fig. 3.8*) in free space can be calculated thanks to the analytical formula given by Grover [Grover_book]. This formula has been calculated in DC and with quasi-homogeneous current density:

$$\left\{ \begin{array}{l} a = \frac{w}{2r} \\ L[\text{H}] = 4\pi \cdot 10^{-7} \cdot r \cdot \left[\frac{1}{2} \left(1 - \frac{1}{6} a^2 \right) \cdot \log_e \frac{8}{a^2} - 0.84834 + 0.2041 a^2 \right] \end{array} \right. \quad (3.81)$$

where w and r are respectively the width and the average radius of the annulus. The thickness does not appear in this expression as if the section is almost square, with a consequent tolerance, the inductance is the same whatever the thickness. This can be explained by the inductance calculus is based on the mean flux computation, which is not much subject to variations of the thickness.

Mutual inductance

This section deals with the calculation of the mutual inductance of two dipoles in free space. We assume that each conductor is filiform. This approximation is generally sufficient when conductors are very close to each other, however a few cases may require a better precision which can be achieved by Lyle's method and will be described later. Fig. 3.9 presents the general case studied here.

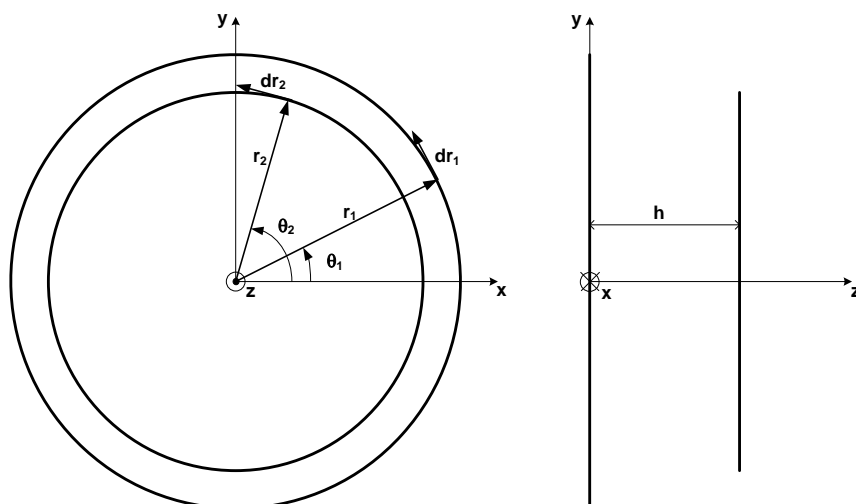


Fig. 3.9 - Two circular wires inductively coupled

We look for an 1‰ accurate and very fast computing expression of the mutual inductance M_{12} of two coaxial circular wire loops with respective radii r_1 and r_2 ($r_1 > r_2$ by convention), and which distance between centers is denoted h . The systematic comparison of many formulas found in literature is detailed in [Artillan2008a]. For the sake of completeness, we are going to present here the only essential steps to obtain this numerical expression of the mutual inductance.

Neumann's formula gives the theoretical expression of the mutual inductance of any two wire loops [Griffiths_book]:

$$M_{12} = \frac{\mu_o}{4\pi} \oint_{C_1} \oint_{C_2} \frac{d\mathbf{r}_1 \cdot d\mathbf{r}_2}{\|\mathbf{r}_1 - \mathbf{r}_2\|} \quad (3.82)$$

In our case, using cylindrical coordinates as shown in Fig. 3.9, the previous formula can be simplified into a single integral expression. Setting down $\|\mathbf{r}_1 - \mathbf{r}_2\| = \sqrt{r_1^2 + r_2^2 - 2r_1r_2\cos(\theta_2 - \theta_1) + h^2}$ and $d\mathbf{r}_1 \cdot d\mathbf{r}_2 = r_1r_2 \cos(\theta_2 - \theta_1)d\theta_1d\theta_2$, we find the particular case of our formula for the partial inductances found into the quasi-static magnetic part (3.42), which can be written as:

$$M_{12} = \frac{\mu_o}{4\pi} \int_{\theta_1=0}^{2\pi} \int_{\theta_2=0}^{2\pi} \frac{r_1r_2 \cos(\theta_2 - \theta_1)d\theta_1d\theta_2}{\sqrt{r_1^2 + r_2^2 - 2r_1r_2\cos(\theta_2 - \theta_1) + h^2}} \quad (3.83)$$

This expression can be simplified into:

$$M_{12} = \frac{\mu_o}{2} \sqrt{\frac{r_1r_2}{2}} \int_{\alpha=0}^{2\pi} \frac{\cos(\alpha)d\alpha}{\sqrt{q - \cos(\alpha)}} \quad (3.84)$$

Where $q = \frac{r_1^2 + r_2^2 + h^2}{2r_1r_2}$, ($0 \leq q \leq \infty$) and $\alpha = \theta_2 - \theta_1$

In order to normalize the expression of M_{12} so that the various numerical methods of computation can be compared, it has been written as the product of $\sqrt{r_1r_2}$ and a function $f(k)$ which only depends on one parameter, k , included between 0 and 1. The function $f(k)$ can be viewed as an image of the magnetic coupling quality:

$$M_{12} = f(k)\sqrt{r_1r_2} \quad (3.85)$$

Where k can be written as:

$$k = \frac{(r_1 - r_2)^2 + h^2}{(r_1 + r_2)^2 + h^2}, \quad (0 \leq k \leq 1 \text{ if } r_1 \geq r_2) \quad (3.86)$$

Finally, by introducing the change of variable $q = \frac{1+k}{1-k}$ and using (3.84), the expression of $f(k)$ can be established:

$$f(k) = \frac{\mu_o}{\sqrt{8}} \int_{\alpha=0}^{2\pi} \frac{\cos(\alpha) d\alpha}{\sqrt{q - \cos(\alpha)}} \quad (3.87)$$

The analytic expression of (3.87) has subsequently been obtained thanks to symbolic calculation software [Mapple_url]:

$$f(k) = \mu_o \sqrt{\frac{2}{q+1}} \left(m \cdot \text{EllipticK} \left[\frac{2}{q+1} \right] - (q+1) \cdot \text{EllipticE} \left[\frac{2}{q+1} \right] \right) \quad (3.88)$$

This expression uses elliptic integral special functions defined as:

$$\text{EllipticK}[a] = \int_{\theta=0}^{2\pi} \frac{d\theta}{\sqrt{1 - a \cdot \sin^2(\theta)}}, \text{EllipticE}[a] = \int_{\theta=0}^{2\pi} \sqrt{1 - a \cdot \sin^2(\theta)} d\theta \quad (3.89)$$

The associated method of computation using built-in elliptic functions will then be referred by mnemonic ELLIP.

Besides this method, various papers propose approximate expressions of $f(k)$, whose validity domain is only partial. Two expressions due to F. W. Grover [Grover_book] have been normalized and compared: they are referred by GROVER0 and GROVER1 and respectively intended to values of k very close to 0 and very close to 1.

$$f_{\text{GROVER0}}(k) = 1.44800 \cdot 10^{-6} \left(\log_{10} \left(\frac{1}{k} \right) - 5.33070 \cdot 10^{-1} \right) \quad (3.90)$$

$$f_{\text{GROVER1}}(k) = 10^{(-6.60776 + \frac{3}{2} \log_{10}(1-k))} \quad (3.91)$$

If one compares the results of all functions (with the values of $f(k)$ given by ELLIP as exact values), it is possible to build an optimized expression of $f(k)$ by using approximate formulae on their range of validity and by completing it with a look-up table linear interpolation function. The optimized expression of $f(k)$, later referred as OPTIM, is then:

$$f_{\text{OPTIM}}(k) = \begin{cases} f_{\text{GROVER0}}(k) & \text{if } k \in]0; 1.7755 \cdot 10^{-3}] \\ f_{\text{GROVER1}}(k) & \text{if } k \in [0.99987; 1[\\ f_{\text{INTERPOLATION}}(k) & \text{otherwise} \end{cases} \quad (3.92)$$

It must be mentioned that the construction of the interpolating function is available on the restricted range of k because $f(k)$ is bounded on this range. On the contrary, an interpolating function could not have been built on the whole range of k , where $f(k)$ is not bounded.

The accuracy of the linear interpolation depends on the values of k that appear in the look-up table. The table has been built with a progressive algorithm: the first value is $k = 1.7755 \cdot 10^{-3}$ and next values have been chosen one after another with respect of the maximum tolerance thanks to the optimization toolbox of Matlab®, *i.e.* for a given value k_i , the next value k_{i+1} has been computed as the maximum value satisfying the criteria:

$$\varepsilon_{\text{INTERPOLATION}}(k) = \left| \frac{f_{\text{INTERPOLATION}}(k) - f_{\text{ELLIP}}(k)}{f_{\text{ELLIP}}(k)} \right| \quad (3.93)$$

$$\max_{k \in [k_i; k_{i+1}]} \varepsilon_{\text{INTERPOLATION}}(k) \leq 0.001 \quad (3.94)$$

The results for $f_{\text{OPTIM}}(k)$ in terms of computing time and accuracy $\varepsilon_{\text{OPTIM}}(k)$ are respectively shown in Fig. 3.10(a) and Fig. 3.10(b). Fig. 3.10(a) shows that OPTIM is at least 1% accurate on the whole range of k . Finally, it can be seen on Fig. 3.10(b) that OPTIM is almost as fast as approximate expressions over the ranges where they are used, however there is a few difference due to the evaluation of the condition over the value of k . Over the range of the interpolating function, OPTIM is a bit faster than ELLIP, which validates that it is optimized.

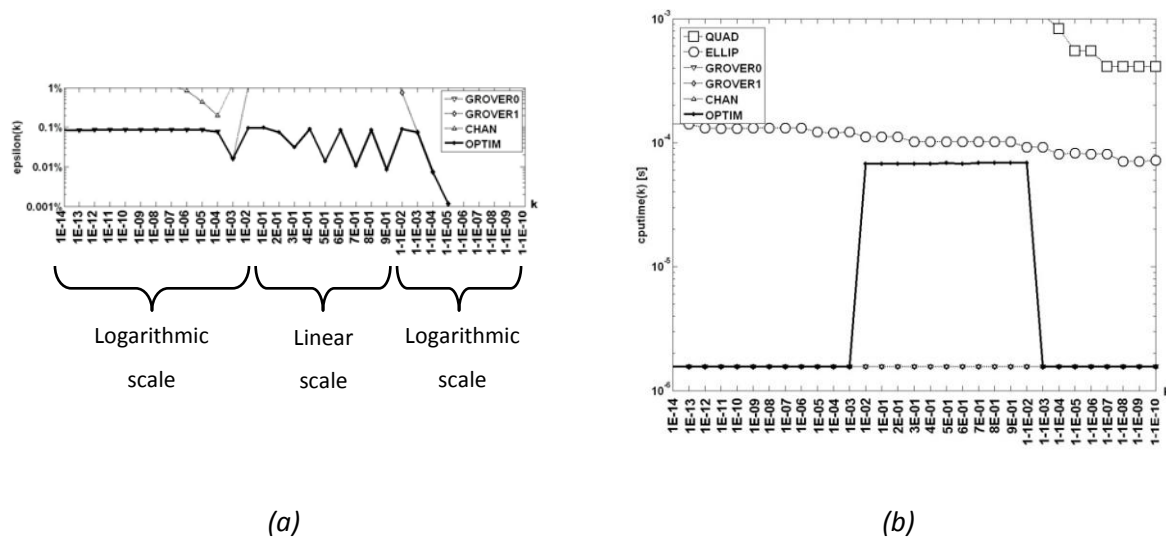


Fig. 3.10 - Comparison of the different methods for the calculus of mutual inductance along the whole parameter k range. Accuracy (a) and computing time (b)

Lyle's method for close conductors

If the conductors are too close, the classic filiform approximation is not sufficient. To avoid a complex volume calculus, Lyle's method [Grover_book] allows us to obtain rather precise values by using a new filiform approach.

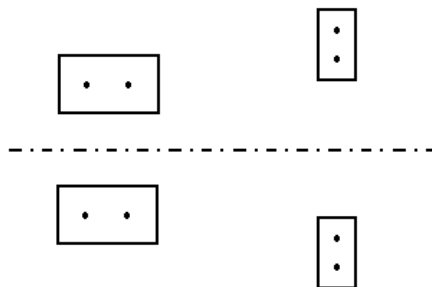


Fig. 3.11 - Two rectangular coils of rectangular cross section approximated by Lyles's method

This method works by replacing each inductance by one or more filaments, depending on the geometry of the cross section. Then, we can calculate the mutual inductance value by applying the basic formula for the mutual inductance of coaxial circles to find the mutual inductance of all the pairs of filaments. Therefore, the mutual inductance of the coils is the sum of all calculated mutual inductances between wires.

c - Capacitance

There are at least two different approaches to find the capacitance matrix defined in (3.58). The first one is a physical approach using the potential coefficients, whereas, the second one is more electrical, as it uses real structural capacitors to compute capacitances and then converts them into the capacitance matrix thanks to (3.62) and (3.63).

Capacitances from the potential coefficient matrix \mathbf{P}

As we have seen, \mathbf{C} matrix is the inverse of \mathbf{P} . From equation (3.55) we can find the expression that will give us the matrix \mathbf{P} when ρ_s is considered constant over a surface panel:

$$P_{ik} = \frac{1}{S_i S_k} \int_{r \in S_i} \int_{r' \in S'_k} G(\mathbf{r}|\mathbf{r}') dS'_k dS_i \quad (3.95)$$

Since this matrix can be inverted, capacitance matrix \mathbf{C} can be found by doing this calculation.

Lateral capacitance formula

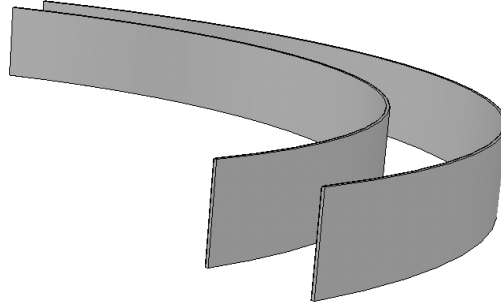


Fig. 3.12 – Lateral capacitance (horizontal face-to-face)

The lateral capacitance C_{lat} between panels i and k can be computed as the capacitance of two face-to-face cylindrical surfaces, considering that the electric field is perpendicular to the lateral faces:

$$C_{\text{lat-ik}} = \frac{1}{4} \cdot \frac{2\pi t \epsilon}{\ln\left(\frac{r_{\text{ext}}}{r_{\text{int}}}\right)} \quad (3.96)$$

Demonstration of (3.96):

Neglecting the edge effects and applying Gauss' theorem to a cylindrical surface S , with height t and radius r (between r_{int} and r_{ext}) $\Rightarrow 2\pi r t E = \frac{Q}{\epsilon}$

Since electrical field must only have a radial component $\Rightarrow E = \frac{Q}{2\pi \epsilon r t}$

Then, applying the relation $\Rightarrow U = V_{r_{\text{int}}} - V_{r_{\text{ext}}} = \int_{r_{\text{int}}}^{r_{\text{ext}}} \mathbf{E} \cdot d\mathbf{r} = \int_{r_{\text{int}}}^{r_{\text{ext}}} \frac{Q}{2\pi \epsilon r} \frac{dr}{r} = \frac{Q}{2\pi \epsilon} \ln\left(\frac{r_{\text{ext}}}{r_{\text{int}}}\right)$

Finally, since $C = \frac{Q}{U} \Rightarrow C = \frac{2\pi t \epsilon}{\ln\left(\frac{r_{\text{ext}}}{r_{\text{int}}}\right)}$

$C_{\text{lat-ik}}$ is just a quarter of the whole capacitance C since whole conductor surfaces are split in four smaller surfaces.

Vertical face-to-face capacitance formula

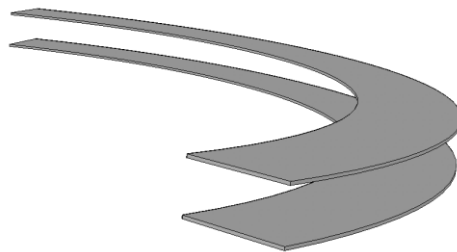


Fig. 3.13 – Stack capacitance (vertical face-to-face)

Interlayer capacitance C_{stack} can also be computed by a general formula of conductors in total influence:

$$C_{\text{stack-ik}} = \frac{1}{4} \frac{\varepsilon \cdot S}{|z_i - z_k|} \quad (3.97)$$

Demonstration of (3.97):

Neglecting the edge effects, a capacitor with parallel panels of surface S and with thickness $|z_i - z_k|$

$$U = V_{z_k} - V_{z_i} = \int_{z_k}^{z_i} \mathbf{E} \cdot d\mathbf{r} = \frac{Q}{\varepsilon_0 S} \int_{z_k}^{z_i} dz = \frac{Q|z_i - z_k|}{\varepsilon_0 S}$$

$$\text{Finally, since } C = \frac{Q}{U} \Rightarrow C = \frac{\varepsilon_0 S}{|z_i - z_k|}$$

C_{stack} is a quarter of the whole capacitance C for the same reason as for the lateral capacitances calculus.

F - Partial elements calculus by FEA method

In this part, we are going to describe different global methods to find the coefficients of the admittance matrix \mathbf{Y} and the capacitance matrix \mathbf{C} by using finite elements calculus. Therefore, we will be able to solve the linear system (3.79). These methods are global since we can determine several coefficients (*a whole matrix column*) by performing only one simulation. Comsol Multiphysics is used to compute conductor set responses to specific excitations.

a - Admittance matrix computation

The value of a coefficient of the admittance matrix can be found as:

$$\forall i, \quad Y_{ij} = \left. \frac{I_i}{U_j} \right|_{U_i(i \neq j) = 0} \quad (3.98)$$

Determining \mathbf{Y} then consists in obtaining the vector of intensities through each conductor \mathbf{I} produced by each canonical excitation \mathbf{U} at the working frequency f . We remind that the admittance matrix is f dependant $\mathbf{Y}(f)$. Canonical excitations can be written as:

$$\mathbf{U} = \begin{bmatrix} 1 \\ 0 \\ \vdots \\ 0 \end{bmatrix}, \begin{bmatrix} 0 \\ 1 \\ \vdots \\ 0 \end{bmatrix}, \dots, \begin{bmatrix} 0 \\ 0 \\ \vdots \\ 1 \end{bmatrix} \quad (3.99)$$

This simplifies the expression (3.98) into:

$$\forall i, \quad Y_{ij} = I_i \quad (3.100)$$

given the i -th canonical excitation \mathbf{U} . Next part describes how to compute those intensity responses to voltage excitation with Comsol Multiphysics.

Comsol Multiphysics subdomain settings

We use the application mode “Azimuthal induction currents, vector potentials” which solves the following differential equation:

$$(\mathbf{j}\omega\sigma - \omega^2\varepsilon)A_\varphi + \nabla \times \left(\frac{1}{\mu} \nabla \times A_\varphi \right) = \frac{\sigma v_{loop}}{2\pi r} \quad (3.101)$$

where A_φ is the φ component of the vector potential \mathbf{A} and v_{loop} the voltage excitation over the cross section. The boundary conditions are detailed in next table:

On z axis	On other external limits	Others
Axial symmetry $r = 0$	Magnetic insulation $A_\varphi = 0$	Continuity $\mathbf{n} \times (\mathbf{H}_1 - \mathbf{H}_2) = 0$

where \mathbf{n} is the vector normal to the considered surface.

Next, we build the meshing. Since the effects on fields near the interfaces between materials are of special interest, to get accurate results we generate a very fine mesh in these areas. To do so, an automatic meshing is convenient and moreover, we refine the mesh one time. Finally we determine a box large enough to have plausible results (*cf. next section: electromagnetic simulations*).

Comsol Multiphysics solutions postprocessing

When simulation is finished, Comsol gives several physical values. On the one hand, we obtain the φ component of vector potential \mathbf{A} (*other components are zero*). On the other hand, current densities are given since Comsol decomposes the total current density \mathbf{J}_{TOT} into the potential current density \mathbf{J}_{POT} and the induced current density \mathbf{J}_{IND} ($\mathbf{J}_{TOT} = \mathbf{J}_{POT} + \mathbf{J}_{IND}$). \mathbf{J}_{POT} corresponds to the current which results from DC conduction effects while \mathbf{J}_{IND} corresponds to the magnetic influence of the system over itself.

Finally, to obtain the intensity through the i^{th} dipole we perform the surface integral of the total current density \mathbf{J}_{TOT} over the i^{th} dipole cross section:

$$I_i = \int_{\mathbf{r} \in S_i} \mathbf{J}_{TOT}(\mathbf{r}) dS_i \quad (3.102)$$

R^{DC} and L^{DC} matrices calculus

R^{DC} and L^{DC} matrices can be calculated with the previous method when frequency is very low, typically 1Hz (*in DC mode the inductance matrix is not accessible in this manner*):

$$\begin{cases} \mathbf{R}^{DC} = \mathbf{Re}[\mathbf{Y}(f = 1Hz)]^{-1} \\ \mathbf{L}^{DC} = \frac{\mathbf{Im}[\mathbf{Y}(f = 1Hz)]^{-1}}{j2\pi f} \end{cases} \quad (3.103)$$

Y(f) computation

For each frequency point, the admittance matrix $\mathbf{Y}(f)$ can be computed with the method described above which takes eddy currents effects into account and leads to precise determination of frequency response. Very computing time efficient method is also the use of DC resistance and inductance matrix:

$$\mathbf{Y}(f) = [\mathbf{R}^{DC} + j2\pi f \mathbf{L}^{DC}]^{-1} \quad (3.104)$$

, this calculation does not take eddy currents effects into account however.

b - Capacitance matrix computation

The value of a coefficient of the capacitance matrix can be found as:

$$\forall i, \quad C_{ij} = \left. \frac{Q_i}{U_j} \right|_{U_i(i \neq j) = 0} \quad (3.105)$$

In the same manner that for the admittance matrix determination, to determine \mathbf{C} we must obtain the charge \mathbf{Q} over each surface of the conductors produced by a canonical excitation \mathbf{U} . Since we work in a pure electrostatic problem, the capacitance matrix \mathbf{C} is not f dependant. Canonical excitations can be written as:

$$\mathbf{U} = \begin{bmatrix} 1 \\ 0 \\ \vdots \\ 0 \end{bmatrix}, \begin{bmatrix} 0 \\ 1 \\ \vdots \\ 0 \end{bmatrix}, \dots, \begin{bmatrix} 0 \\ 0 \\ \vdots \\ 1 \end{bmatrix} \quad (3.106)$$

This simplifies the expression (3.105) into:

$$\forall i, \quad C_{ij} = Q_i \quad (3.107)$$

given one canonic excitation \mathbf{U} . Next part proposes a way to compute these charge responses to voltage excitation with Comsol Multiphysics.

Comsol Multiphysics subdomain settings

We use the application mode "Electrostatic" which solves the Poisson differential equation:

$$\nabla^2 \Phi = -\frac{\rho}{\varepsilon} \quad (3.108)$$

where Φ is scalar potential and ρ the charge density (*excitation over the cross section*).

Boundary conditions are detailed in next table:

On z axis	On other external limits	Others
Axial symmetry	Ground	Surface charge
$r = 0$	$\Phi = 0$	$\mathbf{n} \cdot \mathbf{D} = \rho_s$

where \mathbf{n} is the normal vector to the considered surface.

Next, we build the meshing. Since the effects on fields near the interfaces between materials are of special interest, to get accurate results we generate a very fine mesh in these areas. To do so, an automatic meshing is convenient and moreover, we refine the mesh one time. Finally we determine a box enough large to have plausible results.

Comsol Multiphysics solutions postprocessing

When the simulation is finished, Comsol gives directly the surface charge density ρ_s . To calculate the total surface charge over each conductor, since we work on 2D with axial symmetry of revolution, we can integrate ρ_s as follows:

$$Q = \int_S \rho_s \, dS = \oint_C \int_{\theta=0}^{2\pi} \rho_s r \, d\theta \, dl = \oint_C 2\pi r \rho_s \, dl \quad (3.109)$$

Where dl is an elementary length element that describes the edges of the conductor C .

The capacitance matrix \mathbf{C} is determined in DC mode only since we used the electrostatic equations. The obtained capacitance matrix corresponds to full circular conductors, however, whereas we need the capacitance matrix of associated semi-circular conductors; Next part describes how to perform the necessary transformation.

Capacitance matrix transformation

Comsol gives us the matrix capacitance between rings. As we consider n conductors, capacitance matrix dimension is equal to n . To increase the precision, we are going to divide each ring into two conductors to obtain a matrix of $2n$ dimension. This is possible since we can work with the physical matrix and the matrix of real capacitors by applying the reversible transformation described in (3.62) and (3.63).

SPIRALC approach for circular spiral inductors: cylindrical PEEC + quasistatic FEM simulations or analytic formulas

Matrices type \ Number of panels	Physical matrix	Real capacitors
n	C_n	\tilde{C}_n (3.112)
2n	C_{2n}	\tilde{C}_{2n} (3.111)

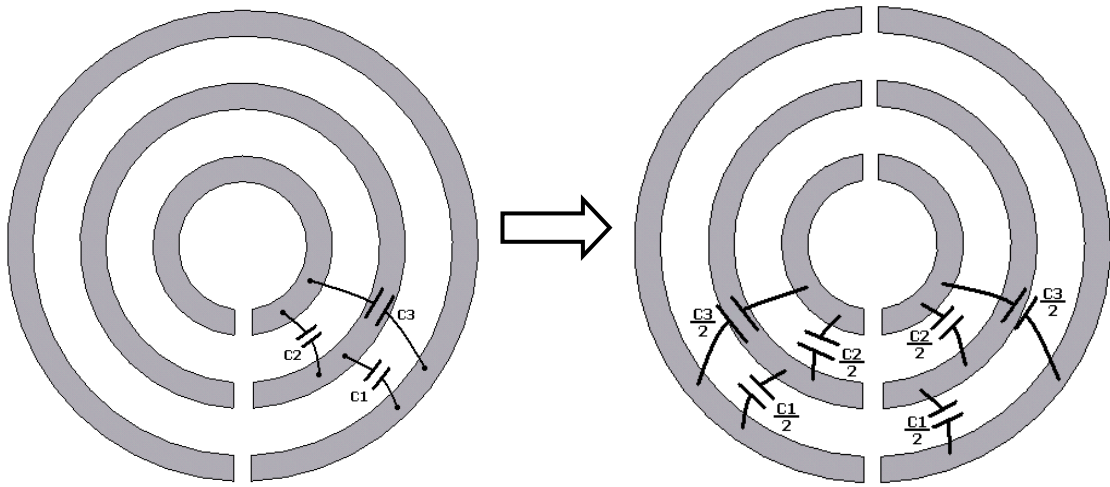


Fig. 3.14 – Capacitors transformation

Here, to pass from C_n to \tilde{C}_n we apply the reversible transformation:

$$\tilde{C}_{n_{ii}} = \sum_{i=1}^p C_{n_{ik}}, \quad \tilde{C}_{n_{ik} (i \neq k)} = -C_{n_{ik}} \quad (3.110)$$

Next, we split the rings into two parts and we only consider the capacitance between the same side rings as the half of the original capacitance. We neglect the capacitance between rings of different side. This leads to the new matrix of 2n dimension:

$$\tilde{C}_{2n} = \begin{bmatrix} \frac{\tilde{C}_n}{2} & 0 \\ 0 & \frac{\tilde{C}_n}{2} \end{bmatrix} \quad (3.111)$$

Finally, we can come back to the physical matrix by performing the inverse transformation:

$$C_{n_{ii}} = \sum_{i=1}^{2p} \tilde{C}_{n_{ik}}, \quad C_{n_{ik} (i \neq k)} = -\tilde{C}_{n_{ik}} \quad (3.112)$$

3 - The software tool: SPIRALC

The theoretical study developed above has been implemented in a software package, which we called SPIRALC to indicate it solves circular spiral inductors problems. In this section, first, we justify the choice of the developing environment, then we describe the functioning of the software tool and, finally, we report some interesting programming hints that have been used to perform the practical implementation.

A - The environment software: Matlab and Comsol Multiphysics

We chose to use the Matlab environment [Matlab_url] because of its powerful programming language, proposing numerous mathematical functions dealing with matrices and complex numbers, and for its direct compatibility with the finite element solver Comsol Multiphysics [Comsol_url]. Actually, Comsol was previously a toolbox of Matlab that evolved to a separate software package with a peculiar graphical interface and many predefined configurations for various types of problems. But the full solver can be used in command line mode using a specific script language to generate the geometrical model and the mesh, to set the equations and variables, to launch the solving of the problem and, finally, to post-process the solution. This script language is compatible with Matlab's syntax and any Matlab program can use the solver of Comsol, provided that the solving server is connected to Matlab. The easiest way to achieve this condition is to launch directly the server from the Matlab program. Furthermore, this method is advantageous as Comsol's graphic interface does not have to be launched, thus saving RAM memory.

We developed our program on Matlab release 7.4 and connected it to Comsol 3.4 solver. We used the standard Graphic User Interface (*GUI*) toolbox functions to create the graphical environment with script commands so that no special toolbox is needed. The only specific toolbox needed is the virtual reality toolbox that is useful to create 3D previews, but the program can run without it.

B - Presentation of the graphical interface

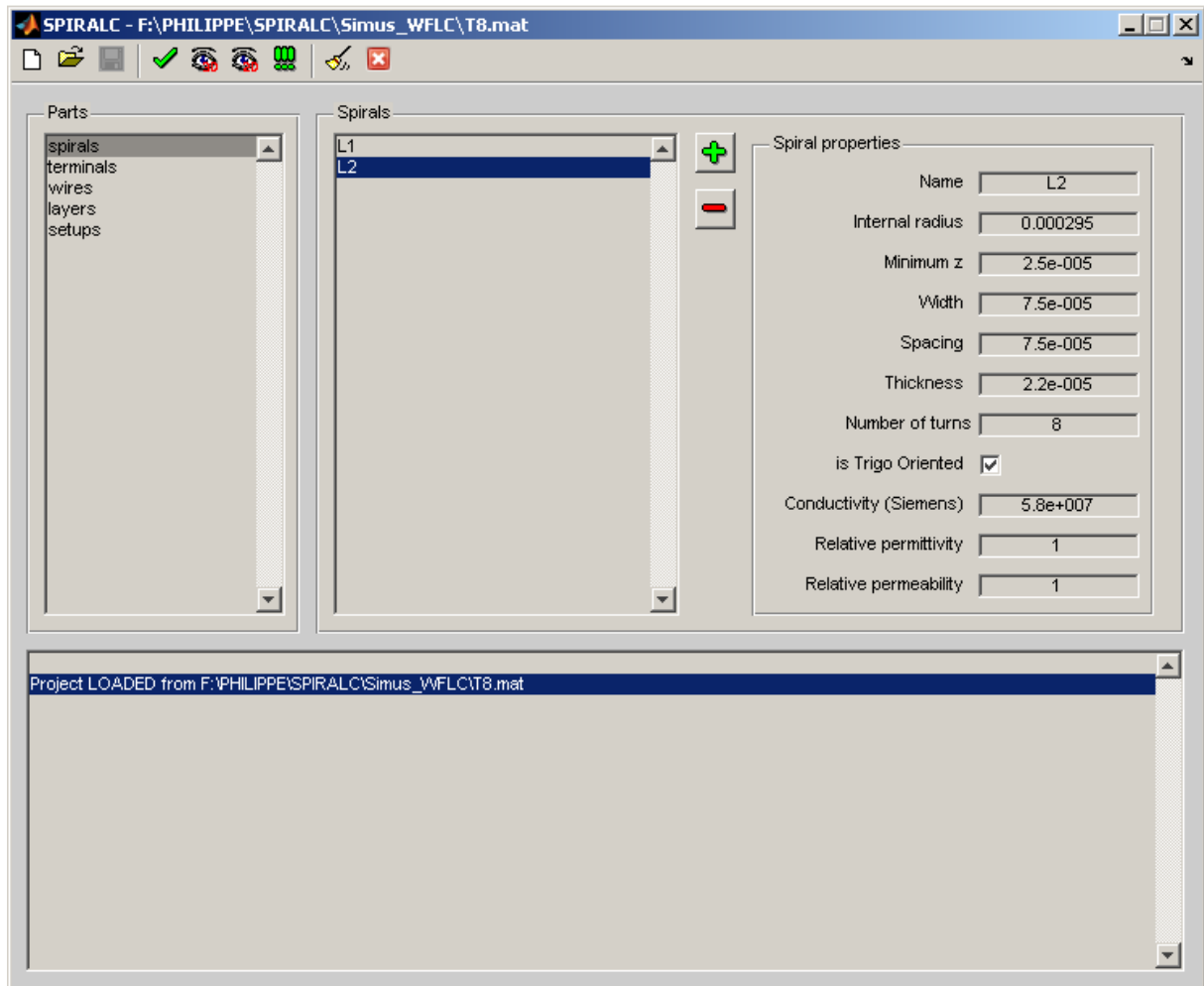


Fig. 3.15 - SPIRALC graphic user interface screenshot example

As said previously, the graphic user interface is set up with script commands, meaning it is “rebuild” at each execution of the program, even if this is not perceptible to the user as it executes very fast. Fig. 3.15 shows a screenshot of this interface. One window corresponds to project, *i.e.* one component being simulated. The toolbar buttons propose nine general actions, from left to right:

- Create a new project
- Open an existing project
- Save the current project
- Check the project
- 2D preview of the geometry
- 3D preview of the geometry
- Analyze all (*i.e.* launch every setup analysis)
- Clear log window
- Close the program

The three first buttons provide common use actions: New/Open/Save commands, allowing saving and loading projects to and from files. Dialog boxes enable to choose the path and name of those files.

The “Check project” button calls a verification procedure that checks the minimum requirements for the project to be valid: at least one terminal, no conductors overlap, etc... and sets a Boolean to “true” to enable the solving of each setup.

The preview buttons give the opportunity to watch the geometry of the component of the current project. The 2D view (*cf. Fig. 3.17*) offers a good representation of the simulated component with a split window both part presenting the conductors section and the rotational symmetry axis (*on the left*). The top subwindow presents the “front” sections, or the first sections met when turning in the trigonometric sense on the conductor seen on top view ($\theta \rightarrow 0^+$), whereas the bottom subwindow present the “back” sections ($\theta \rightarrow 2\pi^-$). The connections between the turns are called wires and are represented by a identical numbers appearing on the sections. The excitation points, called terminals, are represented with colors: a red section is a high potential point and a blue one is a low potential or ground point. Finally, the layers representing the different media surrounding the conductors are presented but the external limits are not represented in true scale because this would lead to undistinguishable information about the conductors. The capture of the geometry and electrical terminals is developed below. The 3D view (*cf. Fig. 3.17*) is, in turn, useful to have a global view of the designed component. The virtual reality modeling language (*VRML*) used to create the virtual reality object representing the component is compatible with different viewers. The screenshot presents a picture realized with the standard Matlab’s viewer that allows the displacement of the camera in the whole virtual world. This is especially handy to check visually the connections between turns.

The “analyze all” button launches the simulation of every setup, whereas the “Analyze setup” button in the setup panel only launches the current setup simulation. The “Clear log window” button is useful to delete all the comments displayed in the low subwindow. Finally, the “Exit” button provides a clean way to exit, however, any other action like closing the figure or using “CTRL+C” in Matlab command window works as well.

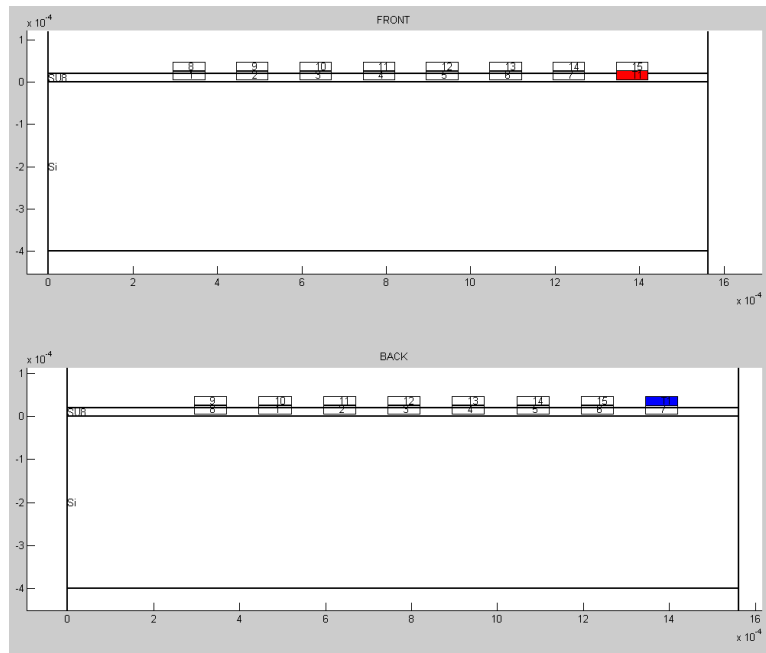


Fig. 3.16 - 2D preview window of SPIRALC

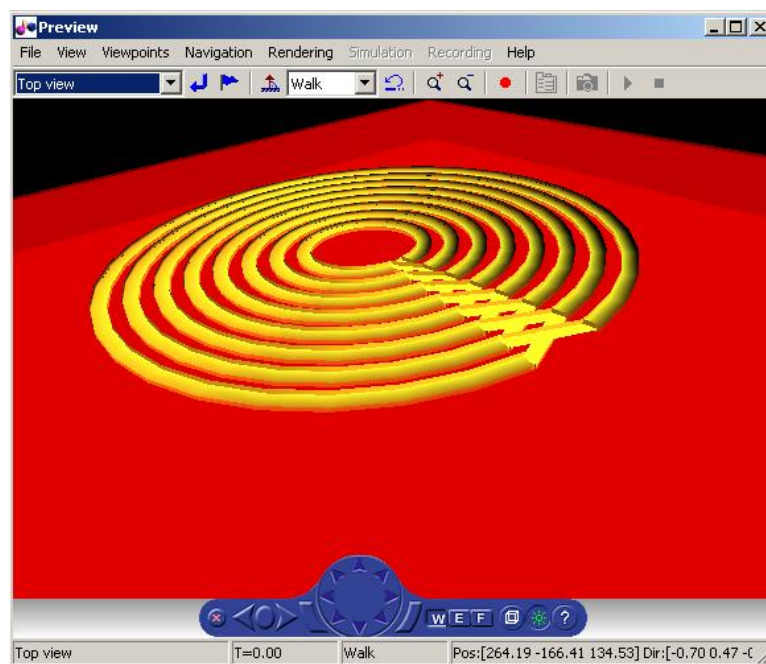


Fig. 3.17 - 3D preview window of SPIRALC

The main window is then separated in two panels: “Parts” and “Current part”. This structure is more or less the same as a tab one, the left panel providing a navigational widget and the right panel being contextually changed to correspond to the current part selection. Five “parts” are available:

- Spirals: to describe a set of conductors with their parameters (*number of turns, width and thickness of the conductors, orientation of the spiral...*). Wires are automatically generated to realize the turn-to-turn connections

- Terminals: to describe the electrical excitation points.
- Wires: to eventually add some connections between spirals
- Layers: to enter the media layers of the problem (*like silicon substrate, photoresist layer, magnetic core layer...*) with their three constitutive constants, *i.e.* conductivity, relative permittivity and relative permeability. The medium are considered linear and isotropic as explained in previous section.
- Setups: to make simulation sets, allowing solving the problem with or without eddy effects and/or with or without capacitive effects. The frequency points list can be generated single point by single point, as a linear set of values or as a logarithmic one.

When launched, the analyze function solves only one setup at once. All the results are saved in the projects as the solving function goes along. If some result has already been computed, it is loaded from the results, resulting in a drastic increase of computing time. When the geometry is modified, the results are automatically reset. First, the analyze function solves the capacitance matrix in DC mode, then the admittance matrix in DC (*arbitrarily taken at 1Hz*) to get the DC values of the resistance and inductance matrices, and finally, if eddy currents effects are requested, it launches one simulation by frequency point, using the linearization of the admittance matrix. At the end of the simulation, the computed values stocked in the results are:

- The DC matrices C , R_{DC} and L_{DC}
- The $d \times d$ admittance matrix Y , where d is the number of conductor rings or dipoles
- The $t \times t$ impedance matrix, where t is the number of ports or terminals
- The n potential vector containing the potential of each node
- The same data computed again with the linearization of the admittance matrix method if eddy currents effects have been computed.

4 - Inductor simulation with finite element method

The design of integrated inductors is generally performed by electromagnetic simulations. Depending on the desired level of modelization (*cf. Chapter 2*), several computing solutions are available. The general goal of a simulation is to give the frequency response of the inductor to a specific excitation. This way, by computing several “points”, or excitation sets, the designer can access the behavior response of the device. This can be achieved to obtain transient response, impedance response versus frequency, electromagnetic field special distribution, magnetic behavior of the core, *etc.* In our work, we are especially interested in computing the harmonic response of our inductors, including current distribution effects, because this is the departure point of the design of

components working at relatively high frequency. The computation of electric and magnetic fields are also useful to evaluate the advantages of specific geometries. On the contrary, we did not perform non linear materials simulations as we considered only air components in order to faster validate our analytical model (*cf. previous section*) with prototype characterizations (*cf. Chapter 4*).

The first part of this chapter is dedicated to the report of our evaluation periods on electromagnetic packages: Quest, Comsol Multiphysics, Maxwell3D and HFSS. After this introduction to FEM software tools and their comparison, the next part deals with the computation by FEM method of the frequency response of realistic inductors on the range of frequency from very low frequency to beyond their serial resonance frequency (*SRF*). This work has thus been split into quasistatic approach for precise low frequency resistive and inductive response and full wave approach for high frequency SRF determination. This has been done with the two FEM solvers by Ansoft Corp.: the quasistatic solver Maxwell® 3D and the full wave solver HFSS™.

A - Evaluated FEM solvers

For the choice of the solver(s) we used to simulate our inductor prototypes, we operated a first selection based on the criteria given above. Our goal was to be able to fully validate our analytical method of modeling, and to develop a simulation method for generic integrated inductor prototypes. The possibility of automatically optimizing the design of a component was not a primary criteria as we count on the analytical approach to perform this in a less time consuming way. However, the simplicity and ergonomomy of modelers including custom geometric variables has raised as a great advantage. We carried out several evaluation periods for various software packages including **Quest by Silvaco** [Silvaco_url], **Comsol Multiphysics by The Mathworks** [Comsol_url] and **Maxwell 3D/HFSS by Ansoft Corp** [Ansoft_url].

Quest is an academic software package passed to industrial market and uses a very new algorithm for interconnect capacitance extraction based on the fictitious domain method which consists in linking the computation of surface charge density on complex shape conductors to the electrical potential computed on a simple “fictitious” domain [Putot1999, Putot1999a]. Its possibilities are limited because it does not have an integrated modeler and needs the importation of design and technology files (*respectively .gds and .tek*) [Silvaco_tech]. This is quite embarrassing because the simulation method is necessarily iterative, meaning that each time an error appears in the model, the full modeling procedure must be performed again. Furthermore, the results obtained for our designs seemed not to take correctly capacitive effects into account as no resonance has been observed.

On the contrary, **Comsol Multiphysics** is a very generic software package: it was first the Matlab PDE toolbox (*Partial Differential Equation*)/Femlab (*Finite Element Method LABORatory*) and then became a separate package. Its approach of magnetic problems is very mathematical. Indeed, the solver implements differential equations on subdomains and their boundary conditions [Langemyr2001]. This provides a complete physical solving environment and seems to be more adapted to special problems involving several physics domains like thermo-electromagnetic problems. We tested version 3.4 extensively, trying 2D and 3D models, and using AC/DC and RF modules. The weak point of this tool is that the automatically generated mesh is not necessarily sufficient for complex structures and the user needs to spend long time to find the adequate mesh, often leading to over-dimensioned ones, thus consuming much simulation time. On the contrary, the possibility to execute any action with script commands and its direct compatibility with the Matlab syntax make it a very powerful tool, and this is why we decided to use it later.

Ansoft Corp. is a company specialized in electromagnetic simulation tools. The Ansoft software suite provides compatible tools (*exportable geometries and results from a package to another, etc.*) which cover a very large part of electromagnetism applications: quasistatic problems including moving pieces (*Maxwell 3D*), radio frequency devices like antennas (*HFSS*), circuit solving (*Simplorer*), parasitic parameters extractor (*Q3D extractor*), etc. On the contrary, no coupled physics or thermodynamics are available, which reduces its use in our case to pure electrical simulations, with the hypothesis that other phenomena influence on the problem is negligible.

Maxwell3D is a package dedicated to low frequency electromagnetism problems: typically rotating machines, magnets applications... but it is also suitable for inductor design as it can solve precisely magnetic effects in harmonic analysis including skin and eddy effects, however, it is not intended to solve the fully coupled electromagnetic equations and is thus unable to model capacitive effects and eddy effects at the same time. The given solution is then valid above the serial resonance frequency, where the capacitive effects are negligible. Depending on needs of the user, four specific solvers are available: "electrostatic", "magnetostatic", "eddy-current" et "transient" (*for non linear materials*).

HFSS is the complement of Maxwell 3D in terms of physical system simulation. Its application domain begins when wave propagation appears, which is the theoretical limit of the quasistatic approach.

Both Ansoft software packages Maxwell 3D and HFSS were thus chosen and used to fully modelize the inductor prototypes frequency behavior. The strong points of the software suite is the

easiness of use of its graphic modeler, its very good adaptive meshing method with a user defined converging criteria and the quality of the visualization tool for the simulated fields.

B - Preliminary simulations: air box dimensioning and ground ring influence

The FEM simulation of any components needs specific preliminary settings. The air inductor case is quite easy, as there are no non linear effects to take into account and thus no bias point to calculate. Anyway, the space restriction domain, or “air box”, and the “para component” elements, in our case the ground ring that has been added to the design for high frequency measurements, are important issues to be performed before the effective component simulation can be done.

a - Air box dimensioning problem

The finite element method consists in discretizing the field region in small meshes where partial derivative relations can be simplified into discrete ones. As the theoretical space region occupied by the fields generated by an inductor (*especially by an air inductor*) is infinite, the designer must approximate it by a finite one, chose as the minimum volume around the component that allows correct simulations. There is no general rule to dimension this so called “air box”. The only valuable method is to begin the simulation process by a study of the influence of the parameters of its volume over the total magnetic energy stored for a given excitation. We chose to use the inductance value, given by Maxwell 3D, to which energy is proportional for a given current excitation. Further simulations performed with Comsol Multiphysics lead us to use the definition of magnetic energy as the integral over the volume of the magnetic energy density.

We customized the air box as a parallelepiped, volume centered on the component, with square cross section of side $D_x=D_y$ and of height D_z (*cf. Fig. 3.18*).

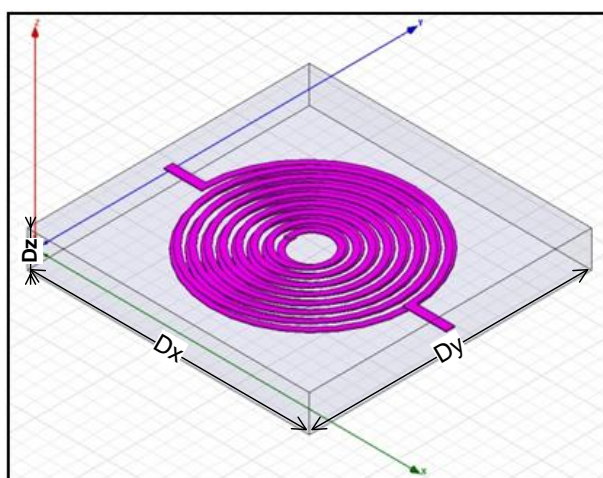
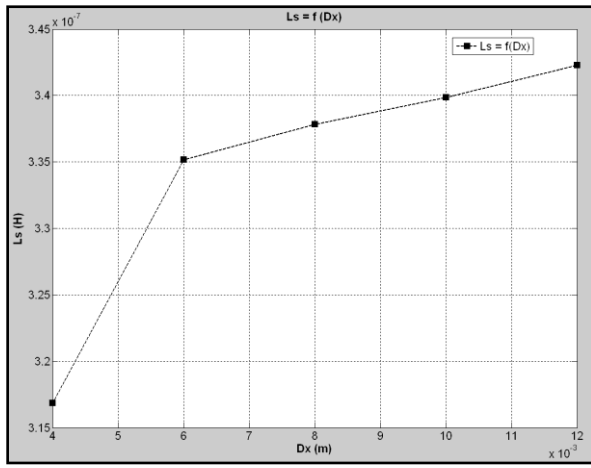
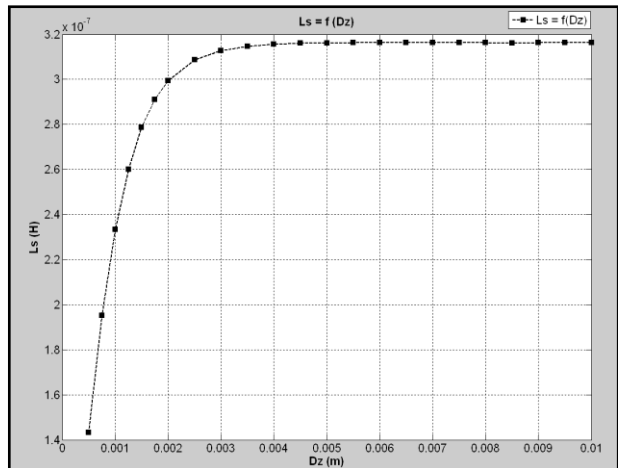


Fig. 3.18 - The inevitable "air box" for FEM simulations

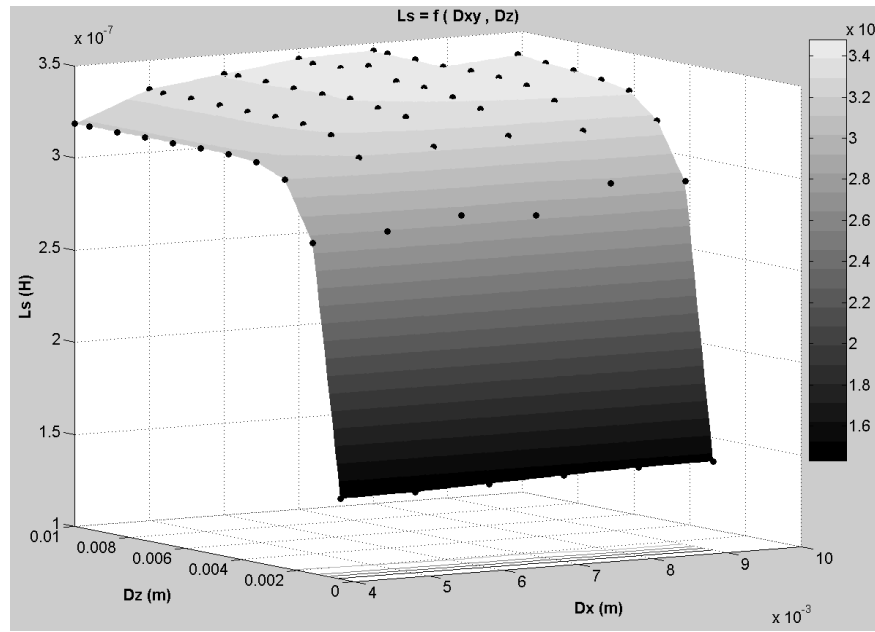
The influence of the two parameters D_x and D_z were first studied separately, as shown on Fig. 3.19 (a) and Fig. 3.19 (b). When D_x is great enough, the inductance is an affine function of it. The offset value of the inductance is the self inductance of the component and the variable part of the inductance value depends on the access path length. Indeed, Maxwell 3D only accepts excitations on the air box cross sections, which go away from each other as D_x increases. The inductance growth is about $1\mu\text{H}\cdot\text{m}^{-1}$ which is a well known order of magnitude for wires inductance. This problem does not appear when D_z increases, which leads to an asymptotic curve for the inductance. The combined influence of D_x and D_z is represented on Fig. 3.19 (c). The behavior is the same as previously described for independent variables. D_z must thus be chosen "great" enough to be in the flat part of the curve and D_x can correspond to real component size, under the condition that there is some sufficient space between the turns and the access electrodes.



(a)



(b)



(c)

Fig. 3.19 – The influence of the air box dimensions on inductance value. (a) inductance versus D_x , (b) inductance versus D_z , (c) inductance versus both D_x and D_z .

b - The influence of a ground ring

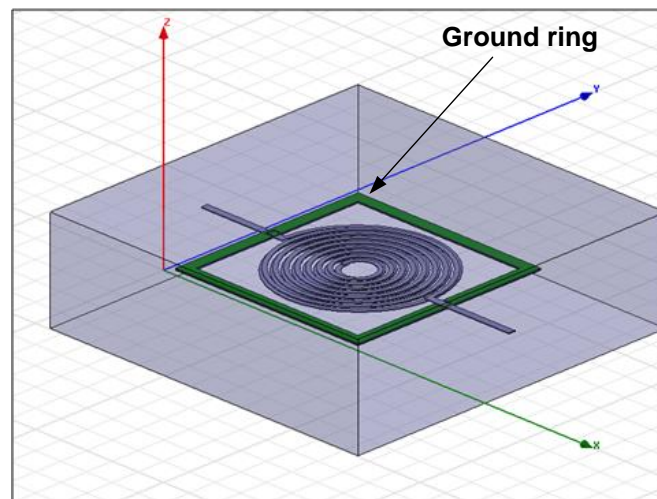


Fig. 3.20 - Simulated inductor with ground ring.

The same study as above has been performed for the same inductor with a ground ring (*cf. Fig. 3.20*). Actually, the ground ring is not useful at low frequency and then in final application of the inductor, but high frequency measurements with RF probes need it. The inductor prototypes have

thus been designed with a ground ring. The simulations lead to the conclusion that ground ring, as designed, does not affect the inductance value for more than 1% ($L_{inductor} \approx 340nH$, $L_{ground_ring} \approx 10nH$).

C - Simulation of the impedance frequency response of an inductor prototype

a - Presentation of the simulated component

We chose to simulate a quasi-realistic component, *i.e.* which could be realized with the same process as we used for our real prototypes. Actually, the simulations we performed mainly aimed at developing a methodology and giving some first theoretical results to have a comparison point with the results of our analytical model. We also choose to avoid the layers simulation, *i.e.* the copper conductors conductivity is $\sigma_{Cu} = 58.10^6 S.m^{-1}$ and air conductivity $\sigma = 0$ and relative permittivity/permeability $\epsilon_r = \mu_r = 1$ are defined elsewhere. This way, the convergence has been easier to obtain because there were no induced eddy currents in the substrate and the displacement currents were simpler. Once again, this does not affect the goal of those simulation to help validating the model.

The component we developed is an inductor constituted of two levels of 10 turns as can be seen on Fig. 3.21. The spiral conductors are $100\mu m$ width, $15\mu m$ thick, spaced of $50\mu m$ and $3500\mu m$ external radius. The two levels are spaced of $5\mu m$. Its DC characteristics are $L_{dc} = 338nH$ and $R_{dc} = 1.27\Omega$.

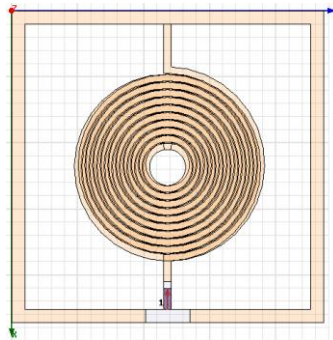


Fig. 3.21 – Top view of the inductor prototype.

b - Computation of impedance frequency response with both quasistatic and full wave solvers

As we explained in section 1, the computation of the full frequency response of the component, including the DC behavior to the serial resonance frequency needs to be separated into quasistatic regime and high frequency regime. We have modeled the same component in Maxwell 3D, as can be seen on Fig. 3.22 (a) and in HFSS, *idem* Fig. 3.22 (b). The best transition frequency appeared to be

10MHz. Maxwell 3D gives results after this frequency but capacitive effects are very poorly modeled and HFSS is unable to give results below this frequency.

Maxwell 3D design involves no ground ring. Two air boxes have been designed, a small one surrounding the conductors inside the big one, which is a way to ask for an automatic mesh refinement near and inside the conductors, where fields are strong and skin effects occurs. We can notice how easy it is to make such a complex operation with this software tool. No consideration about meshing have taken into account for HFSS design, as the RF tool computes coupled electromagnetic equations, which leads to worse precision about current density in the conductors anyway. The ground ring is represented in the RF model because its influence could be non negligible in high frequency, and furthermore, this design hint provides an easy way to define the excitation as a lumped port instead of a wave port.

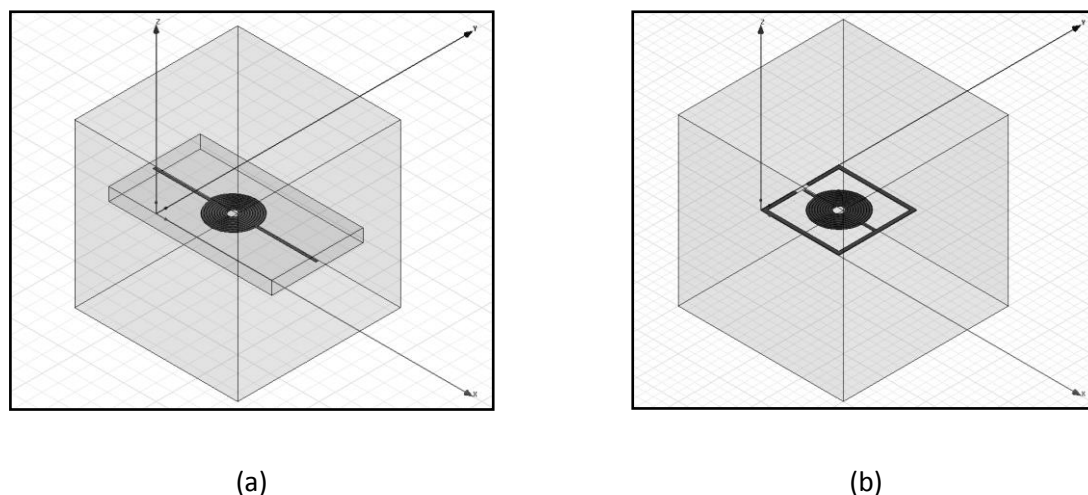


Fig. 3.22 – The simulated inductor prototype modeled in Maxwell 3D (a) and in HFSS (b).

The whole results in terms of complex impedance are shown in Fig. 3.23. We can say that the small increase of the phase before the inductive part of the curve demonstrates that Maxwell 3D takes skin and proximity effects into account. This has been verified by observing graphically the cross sections of the conductors too.

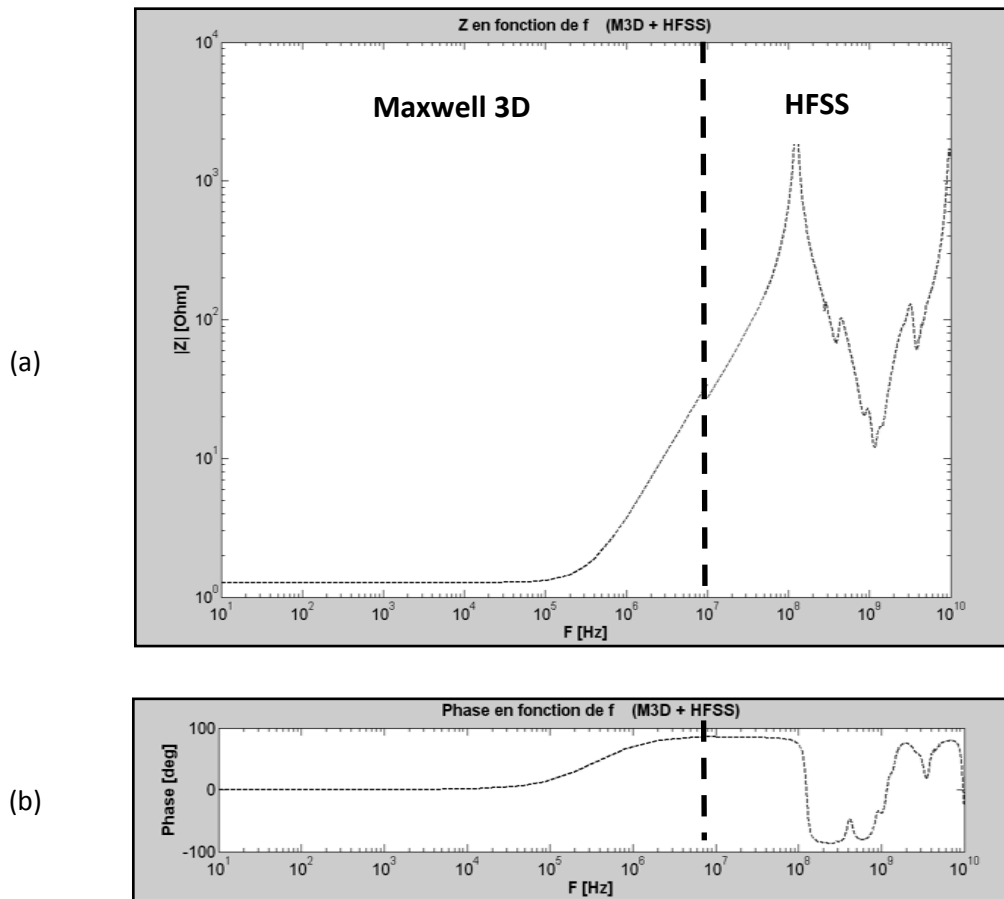


Fig. 3.23 – Complex impedance frequency response computed with Maxwell 3D and HFSS. Magnitude (a) and Phase (b).

Finally, by linking the curves obtained with Maxwell 3D and with HFSS, we have observed that the two software tools compute the same tendency. A little discontinuity exists, however, between the two curves. This is probably because the skin effect is not well modeled by HFSS and also because HFSS curve is obtained by smoothing the frequency response, whereas Maxwell 3D computes each frequency point.

c - Comparison between simulated and analytical results

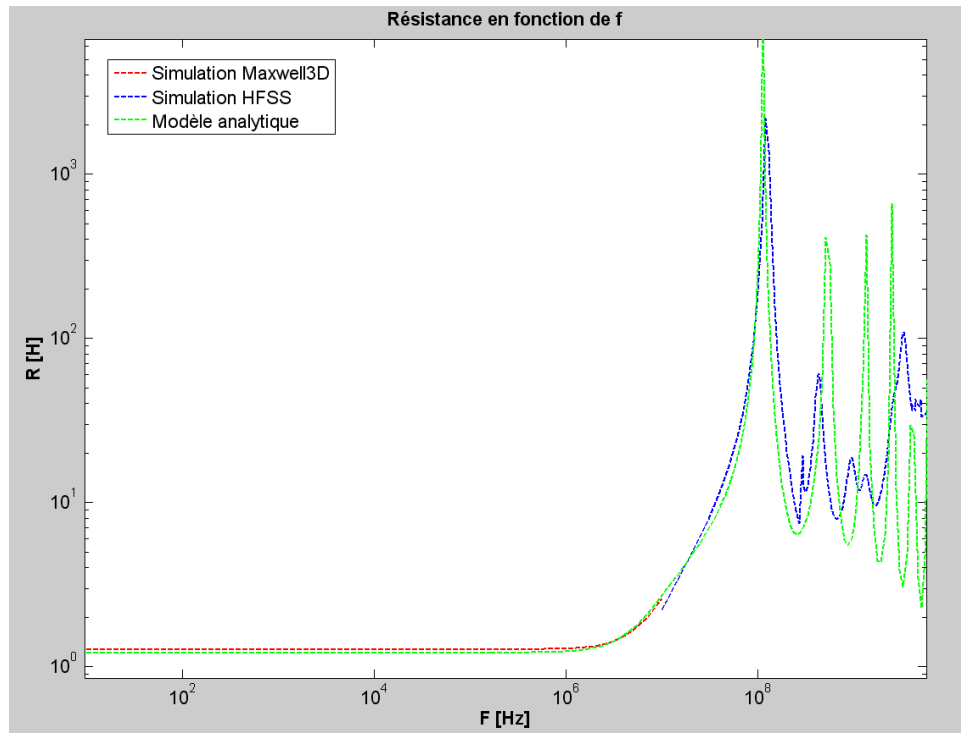
The simulations were the departure point to validate our analytical model which is developed in next chapter. The final validation has been performed upon measurements and will be explained much later. These results are interesting anyway as they demonstrate the very good agreement between simulation and cylindrical PEEC model on a wide frequency range: from DC values to the first rezoning mode.

Fig. 3.24 shows the resistance evolution with frequency. The model and the simulations are coherent above the serial resonance frequency $\left. \begin{array}{l} f_{model} = 113MHz \\ f_{simu} = 120MHz \end{array} \right\}$.

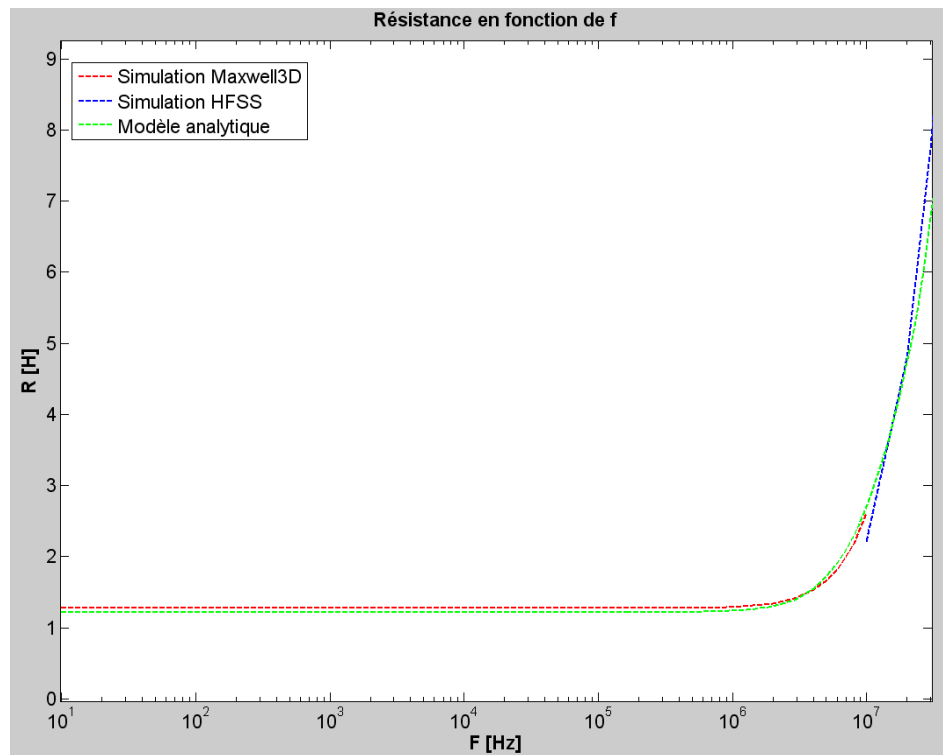
The resistance DC value is $\left\{ \begin{array}{l} Rdc_{model} = 1.21\Omega \\ Rdc_{simu} = 1.27\Omega \end{array} \right.$.

Fig. 3.25 shows the inductance evolution with frequency.

The inductance DC value is $\left\{ \begin{array}{l} Ldc_{model} = 568nH \\ Ldc_{simu} = 565nH \end{array} \right.$.

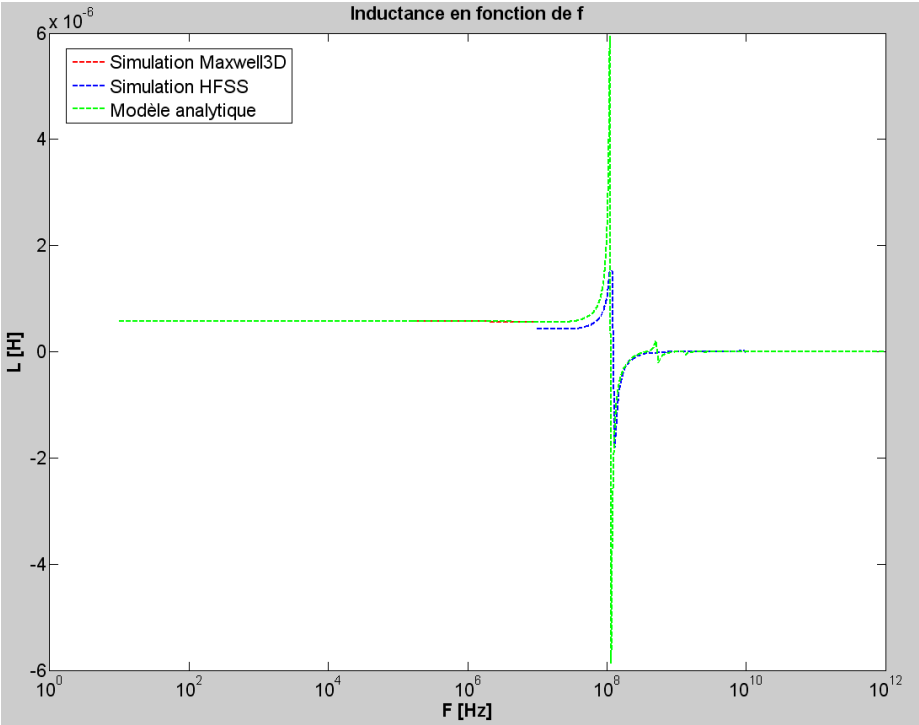


(a)

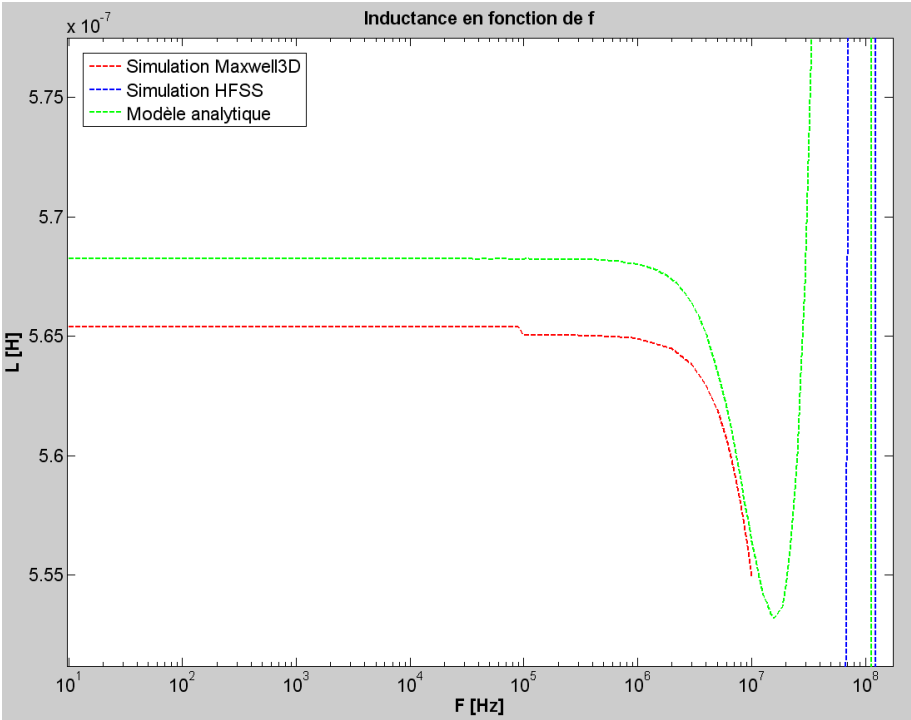


(b)

Fig. 3.24 – Simulated and analytically modeled equivalent serial resistance frequency response. Whole frequency range (a) and zoom on low frequency range (b).



(a)



(b)

Fig. 3.25 – Simulated and analytically modeled equivalent serial inductance frequency response. Whole frequency range (a) and zoom on low frequency range (b).

5 - Conclusion

In this chapter, we presented the full model we developed for circular spiral inductor design. This work has led to an efficient software package allowing the fast computation of the frequency response of integrated devices. The presented full analytical formulation of the PEEC model has been first implemented, but appeared to be either imprecise or slow depending on the size of the meshing used. Finally, the use of partial elements formulation and the computation of matrix coefficients with finite element analysis has been demonstrated to be the most efficient method for achieving our goals of design. A complete finite element method of simulation has then been proposed and shown to be limited because of computation memory needed and frequency range accessible. The results of analytical model and simulations have finally been compared. The good agreement between simulations and analytical results thus validates the formalization of a generalized PEEC method applied to axisymmetric geometry inductive components. This method has then been used to design the prototypes of inductors presented in next chapter.

Chapter 4

Realizations and characterizations

1 - Introduction

The design of integrated inductors implies various trades off to obtain a good compromise between easiness of realization and performances. A one level process would not be interesting in the sense that there is no possibility to design inductors without an underpath or overpath. On the contrary, more than two level processes could be imagined, however there would not be significant differences from the two level process, except the repetition of some steps. Finally, other fundamental processes, concerning the electroplating of magnetic cores or the etching of big aspect ratio trenches [Benazzi2007]. have been studied in parallel to this work in the lab and the perspective of coupling them with actual process will be treated in next chapter. This chapter thus presents our standard two level process for the realization of planar spiral inductors.

In a second time, the problem of characterization will be dealt with. Two methods are confronted: low frequency approach with an impedance analyzer and high frequency with a vector network analyzer. The components have been measured under probe station or in bonded packages. Both result precisions are studied and the most effective method is used to provide an experimental validation of the model presented in previous chapter.

2 - Developed processes for integrated inductive components

The following part describes each step of the process in detail.

Several processes have been developed and are potentially available to realize inductive components. Each process can be viewed as a variation of the basic process of the two level inductors described below.

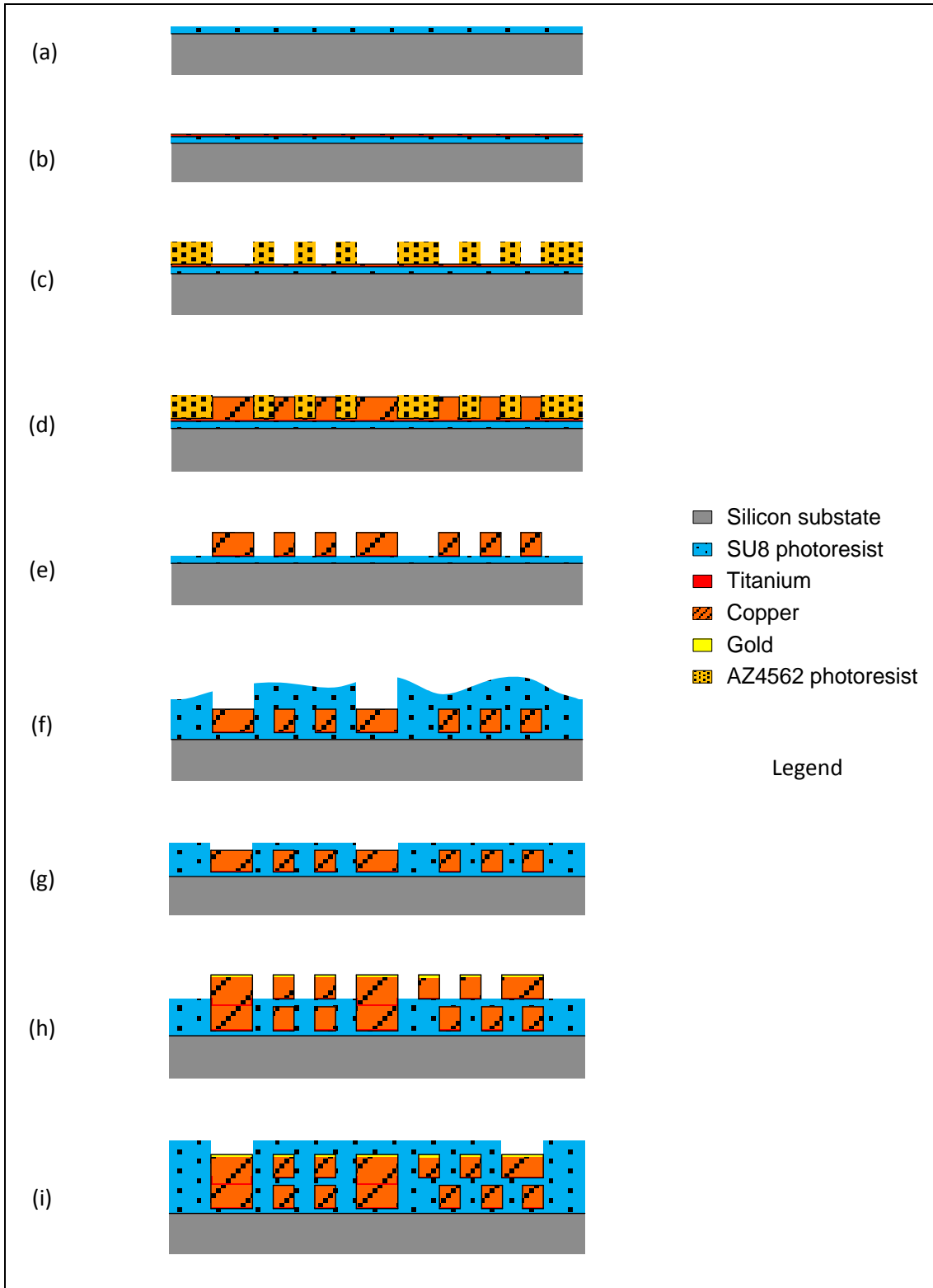


Fig. 4.1 - Two level inductor process

Fig. 4.1 represents the main steps of the process to realize inductors with two levels of conductors.

(a) SU8 insulating layer deposit

The first step of this process is devoted to create an insulation layer between the conductive silicon substrate and the top built component. This could have been achieved by a classical oxidation of the silicon surface by chemical vapor deposition methods (*CVD*); however, the thickness of the layer would have been quite insufficient. Actually, the maximum realizable thickness in an acceptable amount of time in standard ovens is about 3000\AA (*angstrom*). We have then decided to process a $5\mu\text{m}$ controlled thickness SU8 resist layer. It has been done manually by spin coating, using the following parameters.

Coating	<ul style="list-style-type: none"> • Rotating speed: $2000\text{ rot}\cdot\text{min}^{-1}$ • Acceleration: $300\text{ rot}\cdot\text{min}^{-1}\cdot\text{s}^{-1}$ • Rotation time: 30s • Volume: 6mL • Open top (good aeration)
Prebake	
Exposure	<ul style="list-style-type: none"> • Time: 30s (1000W) • Wavelength: 365nm • Full exposure, alignment gap: $50\mu\text{m}$ (to avoid risks of sticking)
Post exposure bake	<ul style="list-style-type: none"> • Idem prebake
Developing	<ul style="list-style-type: none"> • Propylene Glycol Methyl Ether Acetate (PGMEA)

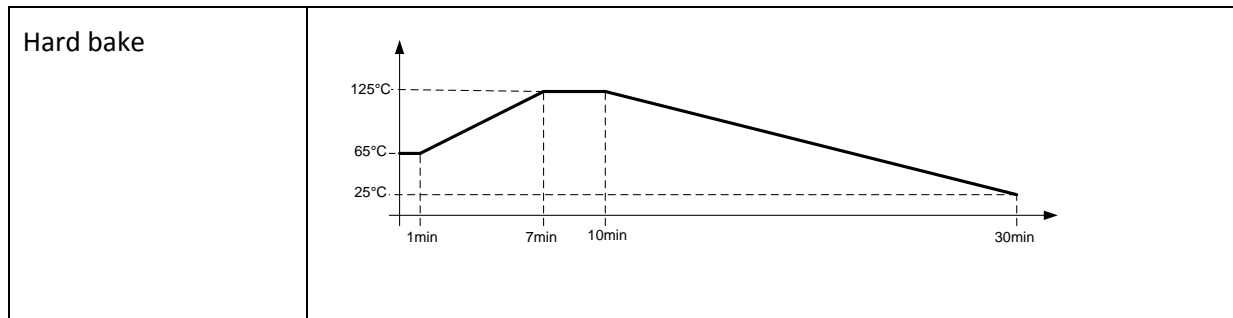


Fig. 4.2 - 5µm thick SU8 layer detailed process

At first, standard bakes have been performed because the SU8 resist is known to be constrictive and can bend the wafer [Guerin_url]. But those bakes are very much time-consuming and we found that this step can easily be shortened by the use of manual bakes simply consisting in putting the wafer on a heating plate set at the maximum temperature of the bake during the standard time. Constraint tests have indeed demonstrated the validity of this method: after the post-exposure bake, the constraint is the same for each method (17.5MPa) and even if right after the hard bake, the simplified bake leads to a stronger constraint (24.3MPa for the simplified bake versus 21.2MPa for the standard bake), and recovers a normal value after 24 hours (19.3MPa for both).

(b) Titanium / Copper seed layer

After the insulating layer is realized, a metallic seed layer must be processed to enable the next electroplating of the conductors. This layer is deposited by a thermal evaporator, a device using an electric resistance heater to melt the material and raising its vapor in a high vacuum to make a conformal depot to the wafer. A titanium/gold layer was first used because it had to be chemically etched after the electroplating step without etching the copper conductors. But an amelioration of the process consisting in a flash of electroplated gold at the end of the electroplating step has enabled the use of titanium/copper tack layers as the top gold on conductors protect them from etching. The experienced showed that a 1000Å titanium/1000Ågold layer is sufficient to realize a good electroplating.

(c) High thickness AZ4562 resist mold

This step consists in creating mold patterns for the electroplating step. It requires a thick resist and the technique is still under improvement. At present, we use AZ4562 photoresist which allows the deposition of metal up to 25µm and which developing process is not diffusible. Next generation of components may be realized with a BCB resist which seems to enable even thicker depots up to 80µm.

(d) Copper electroplating

Metal	Chemical symbol	Conductivity ($S.m^{-1}$) at room temperature (25°C)
Titanium	Ti	1.82×10^6
Aluminum	Al	3.65×10^7
Gold	Au	4.55×10^7
Copper	Cu	5.88×10^7
Silver	Ag	6.21×10^7

Fig. 4.3 - Various metals conductivities at room temperature

Fig. 4.3 shows the conductivity of various metals used for conductive layers and connections in IC process. Most IC metal layers are constructed from aluminum, however, for inductive components applications, the most conductive metal as possible must be chosen to reduce ohmic losses. Even though silver is more conductive, copper is an excellent compromise between conductivity and cost. Copper has then been chosen for the realization of the inductor conductors.

The electroplating of this metal consists in putting the wafer in a bath containing Cu^{2+} copper ions, the wafer constituting the negative electrode of a power supply and the positive electrode being immersed in the bath. In this way, copper is deposited while current is flowing through the bath thanks to ion current. This method is very simple and cost effective, however, it demands a lot of calibration procedures, as the quality, thickness and homogeneity of the depot depends on many parameters: copper concentration, current, pH, catalysts, etc.

Using the wafer as an electrode justifies the conductive layer realized in step (b). This layer must be accessible from the side and an external ring must then be added to the design of the mask used to open the thick resist of step (c).

Finally, an important amelioration has been given to the process by performing a flash of electroplated gold after the normal growth of copper. In this way, the copper conductors are protected during the next wet etching step. Before this innovation, the conductive layer had to be realized with gold for it to be etched with $KI+I_2$ solution which do not attack copper, and the conductors were damaged during the titanium etching.

(e) Wet etching of copper and titanium

As described above, this step consists in releasing the conductors by etching the conductive layer between them. The gold layers were etched with $KI+I_2$ solution and the present copper and titanium

layers are etched with buffer HF solution (=10% *fluorhydric acid*). The key to fulfill a good etching is to wet the wafer with deionized water and alternate etching and rinsing.

(f) SU8 resist planarization

This epoxy negative photoresist has already been used in step (a). It now used to planarize (=flatten) the current level of electroplated conductors. We carried out a lot of techniques to realize a good planarization:

- low speed spin coating with fluid resist SU8 3005 to let it mould the shape of conductors.
- high speed spin coating with viscous resist SU8 3010 and SU8 3020 to use the centrifugal force.
- a first thick deposit with a special photo lithographed pattern making kind of bowls and a second deposit with fluid resist to fill them, hoping the patterns would have retained the resist above each component.
- a one step polishing method consisting in a too thick depot which must be polished. The difficulty of this process is to planarize enough without reaching the conductors.
- a two step polishing process where the resist is deposited in the same way as the previous point but the polishing goes until the conductors and a thin layer of resist (*maximum 5 μ m*) is deposited after.

Experience has demonstrated that the two step polishing process is the best way to obtain a good and flat level after the first level process. The best resist found is the SU8 3005, hard baked at 125°C.

(g) SU8 Polishing

The polishing process has been performed with a grinder machine: the wafer is sandwiched between a fixed platform and a rotating ship.

(h) Second level fabrication

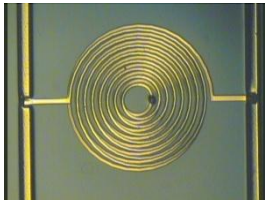
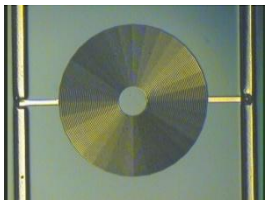
The second level fabrication is processed in the same way as the first level. The efforts made to obtain quality planarization have enabled to omit the classical via electroplating step which avoids several process steps. The via holes are opened during the SU8 deposition step and the thickness being slight enough, the second tack layer moulds the holes perfectly, leading to good conduction between the two layers. Planarizing the same way as first level could let a third level be feasible.

(i) Bonding

When the wafer process is finished, the components can be cut up and bonded on specific packages. This has been very useful for characterization and tests because it allows using the component as discrete ones. The components are stuck with glue and microwires are brazed. Double bonding can be performed to decrease the access resistance due to those wires. Finally, a drop of protecting resist can be put on the components too.

3 - Inductor prototypes

The final wafer is presented in details below. Others have been realized before to improve the process or test the incidence of inductor shape (square, octagonal, circular) [Salles_thesis]. The circular spiral shape has been chosen because it minimizes the current concentration in vertices, responsible for the DC resistance increase, the local overheating and finally the low current limitation of devices. Ground rings have been designed to enable the measurement with RF probes, according to Cascade Microtech recommendations [Cascade_tech]. Several types of components have been designed to experiment the action of various parameters, as described below (*cf. Fig. 4.4*), and some calibration patterns have been added to the final wafer mask set for measurement improvement (*cf. Fig. 4.5*).

	Photography	L_{DC} R_{DC} SRF	Description
T1		315nH 1.2 Ω 126MHz	Reference prototype: one conductor of width $w=75\mu\text{m}$ spaced of $s=75\mu\text{m}$. Internal radius $r_{int}=205\mu\text{m}$. First level has $n_1=8$ turns and second has $n_2=7.5$ turns. The ground ring is a square of width $200\mu\text{m}$ and its internal side is $a_{int}=4325\mu\text{m}$. Variant: T1bis idem without ground ring.
T2		9.4 μH 34 Ω 23MHz	High inductance prototype: idem T1 except $r_{int}=285\mu\text{m}$; $w=15\mu\text{m}$; $s=15\mu\text{m}$; $n_1=40$; $n_2=39.5$.

Inductor prototypes

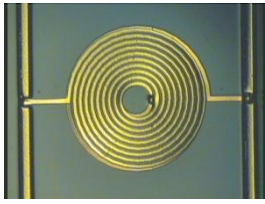
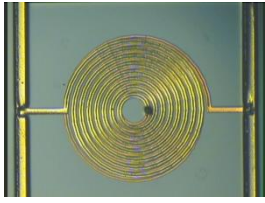
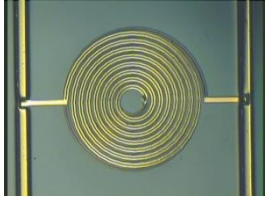
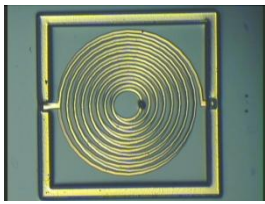
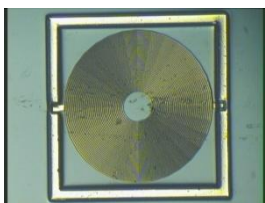
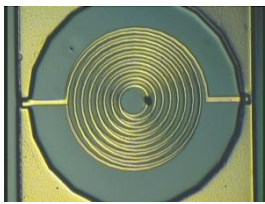
T3		310nH 930mΩ 75MHz	Low resistance prototype: idem T1 except $r_{int}=225\mu\text{m}$; $w=100\mu\text{m}$; $s=15\mu\text{m}$; $n1=10$; $n2=9.5$.
T4		340nH 1.6Ω 134MHz	Straight multiconductor prototype $r_{int}=245\mu\text{m}$; $w1=37.5\mu\text{m}$; $s1=15\mu\text{m}$; $w2=37.5\mu\text{m}$; $s2=60\mu\text{m}$ $n1=8$; $n2=7.5$.
T5		340nH 1.6Ω 134MHz	Crossed multiconductor prototype $r_{int}=245\mu\text{m}$; $w1=37.5\mu\text{m}$; $s1=15\mu\text{m}$; $w2=37.5\mu\text{m}$; $s2=60\mu\text{m}$ $n1=8$; $n2=7.5$.
T6		315nH 1.2Ω 126MHz	Small surface prototype: idem T1 except the ground ring is a square of internal side $a_{int}=3160\mu\text{m}$.
T7		9.4μH 34Ω 23MHz	Small surface, high inductance prototype: idem T2 except the ground ring is a square of internal side $a_{int}=3160\mu\text{m}$.
T8		315nH 1.2Ω 126MHz	Really axisymmetric prototype: idem T1 except the ground ring is circular of diameter $D_{int}=4325\mu\text{m}$.

Fig. 4.4 - Inductor prototypes nomenclature and description

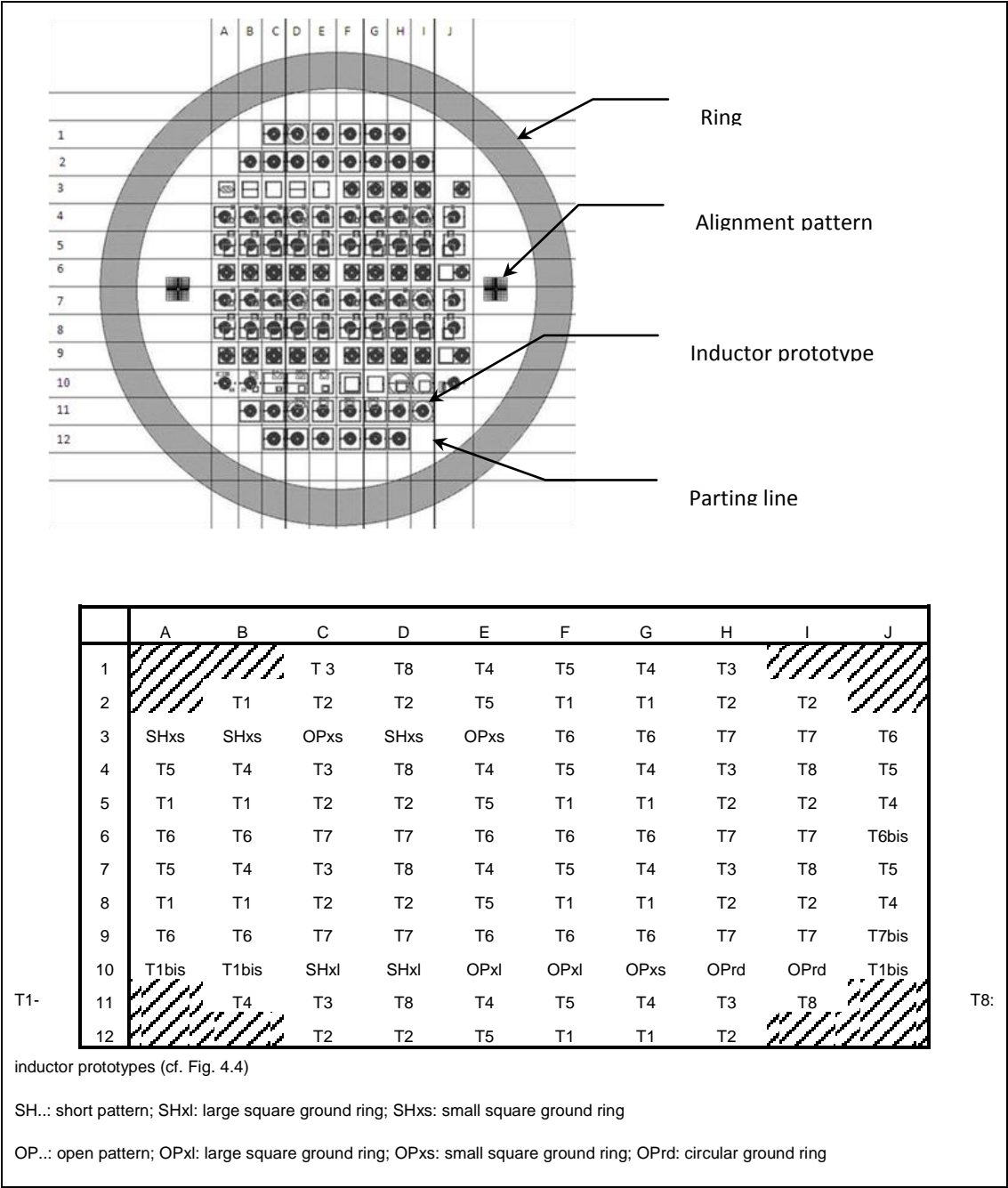


Fig. 4.5 - Wafer cartography

Remark: the denomination “open” and “short” patterns corresponds to low frequency measurement convention; high frequency measurement calls the short pattern a “thru” and the “short” denomination is dedicated to a pattern that shunts each port.

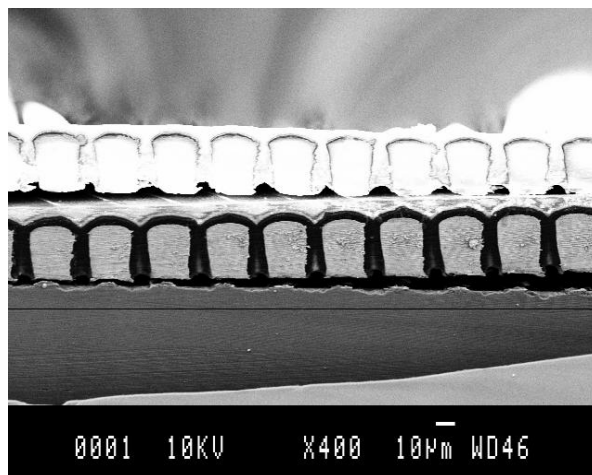


Fig. 4.6 – Cross section view of a two level inductor prototype

4 - Characterization of passive components

The characterization of passive components consists in obtaining some information about their behavior by electrical measurements. Thus, the two first emerging questions are: “where are the electrodes, i.e. the electrical access points?” and “what physical phenomena must be taken into account?” Chapter 2 is, in part, deals with these questions which sometimes become hard, especially when frequency increases and linearity disappears.

Concerning discrete components, a lot of experimental sets have been realized and reported in literature, leading to the measurement of magnetic or electric features, current limitations and complex impedance frequency response [Margueron2006]. Those methods are generally intended to allow a parameter extraction for a simplified model of the device. Even if previous works are mostly transposable to integrated passive components, their characterization is also a specific issue, as their complex structure, based on planar technology, and their smaller dimensions are often responsible for specific phenomena. Furthermore, the existing measurement devices are conceived for discrete components and a new solution must be found at each time to make them compatible.

In the following part, we propose a brief overview of existing measurement methods and a comparison of their performances.

A - Low frequency measurement

The low frequency (*LF*) characterization of inductors can be performed essentially with two kinds of measurement devices:

- LCR meters and impedance meters, that use the method of Wheatstone bridge or current/tension measurement (*I-V method*). They deliver spot (*=point by point*) measurements, like 4284A/4285A [Agilent5_tech].
- Impedance analyzers, that use auto balancing bridge method or any method capable to automatically give the impedance with a controlled oscillator, They deliver continuous frequency measurements (*=the user sets a frequency range and a number of points*) like 4294A impedance analyzer or E4991A RF impedance analyzer.

The choice of the measurement device is the result of some previous work. Various types of measurement methods have been studied and their comparison is extensively related in [Artillan_tech]. This work has lead to the installation of a measurement bench. The chosen device is the Agilent 4294A which features are described in next part. Several configurations for on wafer or bonded components measurements have been tried and compared and are reported below.

a - The auto balancing bridge measurement method

The characterization of our prototypes has been performed at low frequency with the impedance analyzer 4294A from Agilent Technologies. This device is conceived to measure one-port components in a very large range of impedances, $3m\Omega \leq |Z| \leq 500M\Omega$, in the frequency range from 40Hz to 110MHz, with a very good accuracy (*cf. part e -*).

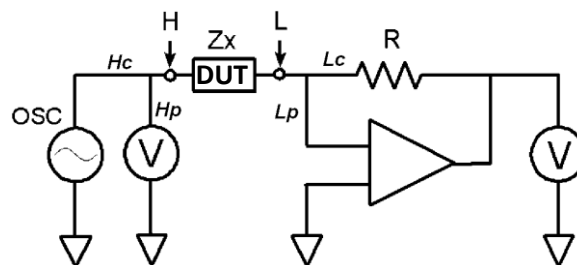


Fig. 4.7 – Functional diagram of auto-balancing bridge method and four points impedance measurement

Fig. 4.7 shows a functional representation of the auto-balancing bridge method used in the impedance analyzer Agilent 4294A. The current through the device under test, or DUT, also goes through the resistor R. The L point potential is maintained equal to 0V (it is a virtual ground) because the current in R balances with the current in the DUT thanks to the current-voltage converter. The impedance of the DUT is computed from the measurement of voltages at the H point and over R.

The 4294A has a four terminals configuration in order to decrease the line losses. Actually, the “lines” are composed of the electrical path from the oscillator, the voltmeters and the current-voltage converter to the DUT. It can be quite long, especially when a test fixture, or a whole specific access device as a probe station, is inserted between the impedance analyzer and the DUT. In that

case, it is useful, when possible, to avoid the line losses by splitting the excitation current and the measurement voltage paths.

Finally, it is important to note that the low point (L) of the DUT is floating, *i.e.* is not connected to the circuit ground. The device has then four coaxial ports Hc, Hp, Lc and Lp (*respectively standing for High current, High potential, Low current and Low potential*) of which shields are grounded.

b - Probe station measurements

We first attempted to measure our components directly with a probe station system. We set up two systems:

- **Four points probing system** (*cf. Fig. 4.8*): two LF probes allowing the four terminals configuration measurement. This configuration is intended to minimize line losses.
- **One port HF probing system** (*cf. Fig. 4.9*): using the Agilent probe 42941A which converts the four terminal panel output of the 4294A to a one-port coaxial access. We connected the probe SMA connector (*small coaxial*) to an RF probe. As the DUT is designed in two-port configuration, the second port is shorted with a second RF probe on which a shorting device is connected. This configuration is intended to take advantage of the Agilent probe 42941A test fixture that is designed to enable measurement in places far from the 4294A. Indeed, when the cable length is important, it is recommended to use a unique coaxial access that reduces the current path. Furthermore, the 4294A performs a phase compensation routine that sets the balancing bridge circuit to emit a balancing signal in phase with the excitation signal and thus guaranteeing the balance of the bridge even for highest frequencies.

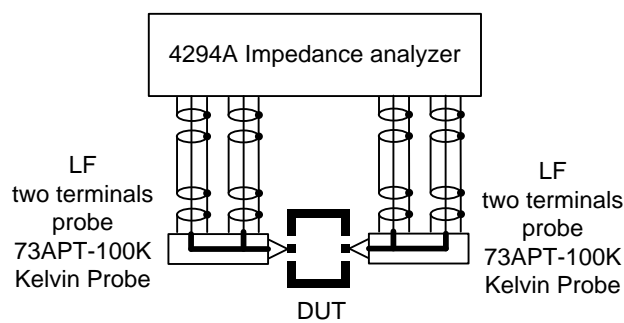


Fig. 4.8 - Four points measurement probing system

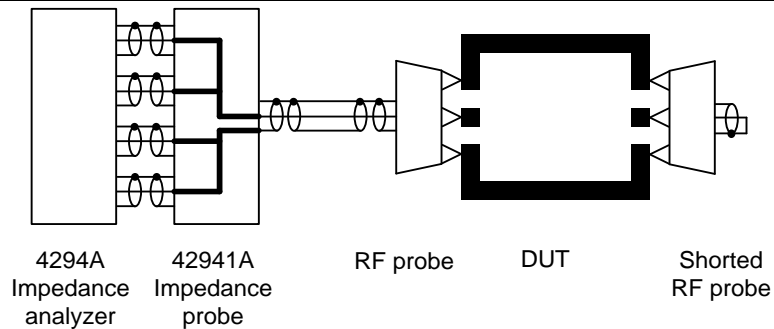


Fig. 4.9 - RF probing system using Agilent 42941A impedance probe

The accuracy of measurements is discussed in part (e -) .

c - Bonded components

The Agilent 4294A is originally designed to measure discrete components with the specific four terminal pair test fixture 16047E. Discrete components are then placed very close to the front panel, thus minimizing the cable length and the resulting losses. A solution to measure integrated components impedance is then to mount them in discrete packages as described in part 2 -. The losses then come from the package and can be evaluated and in part subtracted by performing the compensation with specially designed compensation patterns mounted in packages.

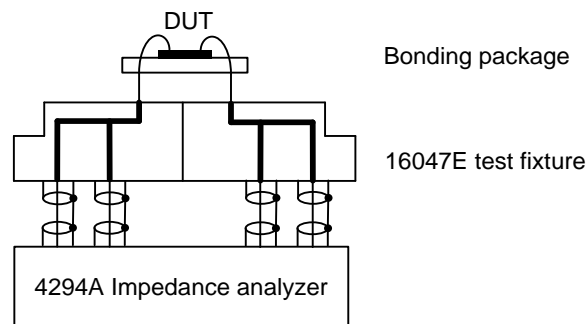


Fig. 4.10 - Bonded components measurement with Agilent 4294A impedance analyzer

The accuracy of measurements is discussed in part (e -).

d - Test fixture compensation

We performed open and short compensations for each configuration of the measurement system described previously. This method assumes that the residuals of the test fixture can be represented by the simple RLCG transmission line model (*cf. Fig. 4.11 - a*). When the terminals of the test fixture are open, stray admittance Y_o (*conductance and capacitance $Y_o = G_o + j\omega C_o$, cf. Fig. 4.11 - a*) is measured because residual impedance Z_s is negligible. When the test fixture terminals are shorted, the measured impedance represents residual impedance $Z_s = R_s + j\omega L_s$ because Y_o is bypassed

(cf. Fig. 4.11 - b) [Agilent4_tech]. As a result, each residual parameter is known and, the DUT's impedance, Z_{dut} , can be calculated from the following equation:

$$Z_{dut} = \frac{Z_m - Z_s}{1 - Y_o \cdot (Z_m - Z_s)} \tag{4.1}$$

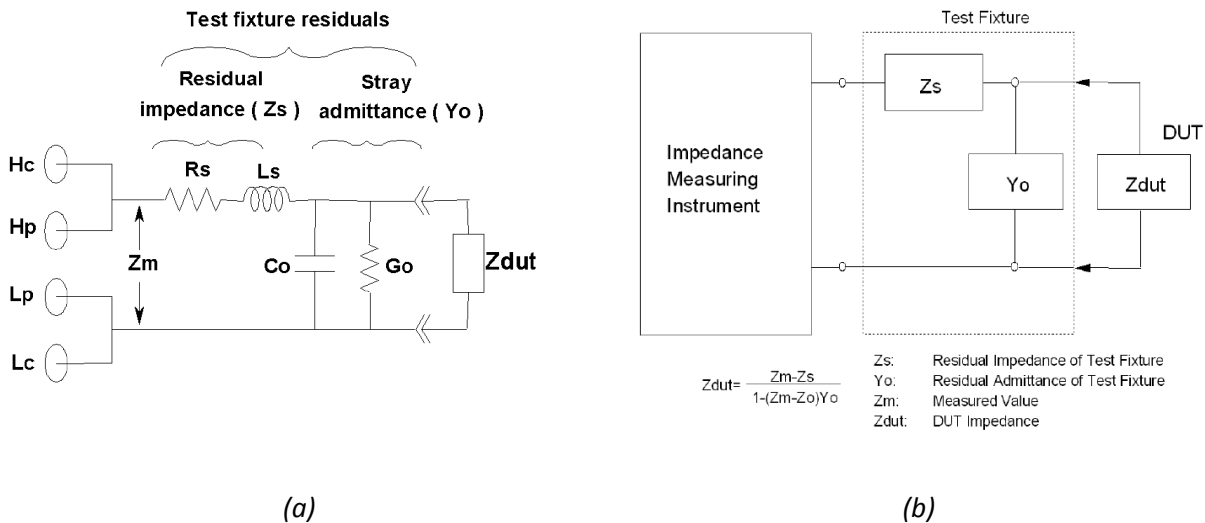


Fig. 4.11 - Open/Short compensation: RLCG equivalent model (a) and impedances measured during compensation (b) [Agilent_tech]

Notice that a “short” pattern in LF is the equivalent to a “thru” pattern in RF as LF is a one-port approach and HF is a two-port approach.

e - Accuracy evaluation

The measurement accuracy depends on many parameters like frequency, measured impedance value, sampling bandwidth, oscillator level, etc. We choose to study the accuracy of bonded components measurements because they have demonstrated to be the most valuable measurements as explained in part C -. The settings of the 4294A were:

- frequency range: [100Hz-110MHz],
- sampling bandwidth reference: 3,
- oscillator level: 300mV for the bridge to be balanced over the whole frequency range

The 4294A datasheet [Agilent4_tech] gives a complete documentation about the accuracy computation. For the above settings, the following equations for this calculus are reported here for the sake of completeness. First, the total error, defined as the ratio of the variation of the impedance magnitude over the impedance magnitude itself $\frac{|\Delta Z|}{|Z|}$, is the sum of the error due to the oscillator

E_{OSC} , the error due to the bandwidth selection E_{BW} , the error due to static imprecision in the measurement circuit E_P and the error due to the impedance dependant error in the measurement circuit E_M :

$$E = \frac{|\Delta Z|}{|Z|} = E_{POSC} + E_{PBW} + E_{PF} + E_{PMEAS} \quad (4.2)$$

And, according to the 4294A datasheet, the phase absolute error can be deduced from (4.2):

$$\Delta\theta = \frac{E[\%]}{100} [\text{rad}] \quad (4.3)$$

The oscillator error is given by:

$$E_{POSC}[\%] = 0.03 \left(\frac{500}{V_{OSC}[\text{mV}]} - 1 \right) = 0.02\% \quad (4.4)$$

where $V_{OSC}[\text{mV}]$ is the oscillator voltage amplitude.

The bandwidth selection error is given by:

$$E_{PBW}[\%] = \begin{cases} 0.2\% & \text{if } 40\text{Hz} \leq f < 50\text{kHz} \\ 0.1\% & \text{if } 50\text{kHz} \leq f < 110\text{MHz} \end{cases} \quad (4.5)$$

The measurement circuit error is given by:

$$E_{PF}[\%] = \begin{cases} 0.5\% & \text{if } 40\text{Hz} \leq f < 100\text{Hz} \\ 0.3\% & \text{if } 100\text{Hz} \leq f < 800\text{Hz} \\ 0.075\% & \text{if } 800\text{Hz} \leq f < 1\text{MHz} \\ 0.1 \cdot f[\text{MHz}]\% & \text{if } 1\text{MHz} \leq f < 15\text{MHz} \\ 1.5\% & \text{if } 15\text{MHz} \leq f < 110\text{MHz} \end{cases} \quad (4.6)$$

And finally, the impedance dependant error is given by:

$$Y_{INT} = \begin{cases} 10 \cdot 10^{-9} & \text{if } 40\text{Hz} \leq f < 100\text{Hz} \\ 2.5 \cdot 10^{-9} & \text{if } 100\text{Hz} \leq f < 200\text{kHz} \\ 5 \cdot 10^{-9} & \text{if } 200\text{kHz} \leq f < 1\text{MHz} \\ 50 \cdot 10^{-9} & \text{if } 1\text{MHz} \leq f < 15\text{MHz} \\ 500 \cdot 10^{-9} & \text{if } 15\text{MHz} \leq f < 110\text{MHz} \end{cases} \quad (4.7)$$

$$Z_{INT} = \begin{cases} 0.01 & \text{if } 40\text{Hz} \leq f < 100\text{Hz} \\ 0.0025 & \text{if } 100\text{Hz} \leq f < 110\text{MHz} \end{cases}$$

$$K_{BW} = \begin{cases} 3 & \text{if } 40\text{Hz} \leq f < 1\text{MHz} \\ 4 & \text{if } 1\text{MHz} \leq f < 110\text{MHz} \end{cases}$$

$$K_{OSC} = \frac{500}{V_{OSC}[\text{mV}]}$$

$$E_{PMEAS}[\%] = 100 \cdot K_{BW} \cdot K_{OSC} \cdot \left(Y_{INT} \cdot |Z| + \frac{Z_{INT}}{|Z|} \right)$$

Those equations have been implemented in Matlab® to visualize the effects of accuracy. First, the contribution of each error type versus frequency is represented in Fig. 4.12. The total accuracy is never greater than 2%, which means the measurements are theoretically very accurate. We'll see though that the determination of inductance and resistance can be affected by the device accuracy even with such a quality of measurement.

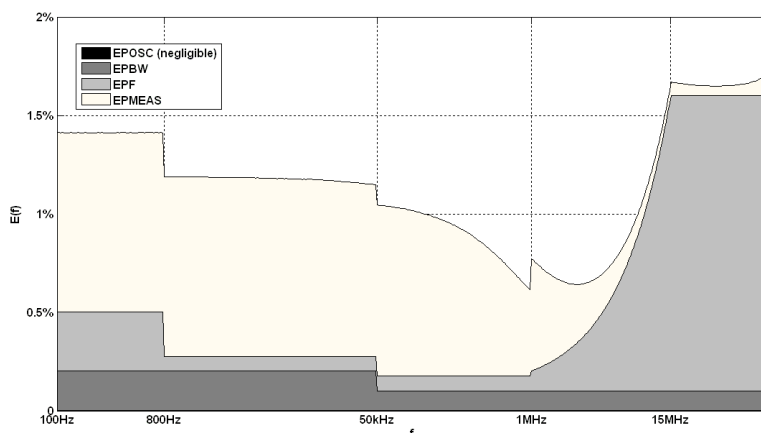


Fig. 4.12 - Agilent 4294A decomposed relative error function E(f)

Fig. 4.13 shows the measured value of the impedance of a T8 inductor prototype. It has been represented in four real parameter: the magnitude $|Z|$, the phase $\text{Phase}(Z)$, the equivalent serial resistance R_s and the equivalent serial inductance L_s which definitions are further detailed in chapter 2. The uncertainty zone, the domain where the curve could be according to the frequency dependant accuracy calculus is also plotted to show the specificity of the measurements. The calculus of accuracy showed that for any frequency, the magnitude and the phase could vary less than 2%. However, the equivalent resistance and inductance are very sensitive to measurement errors in certain domain: low frequency for inductance and the frequency range before the serial resonant frequency of the component. These phenomena can be explained by the distribution of uncertainty depending on the phase value: for frequencies where the component is very resistive, the inductance

value is very low accurate, and, conversely, an inductive behavior leads to an inaccurate determination of the resistance.

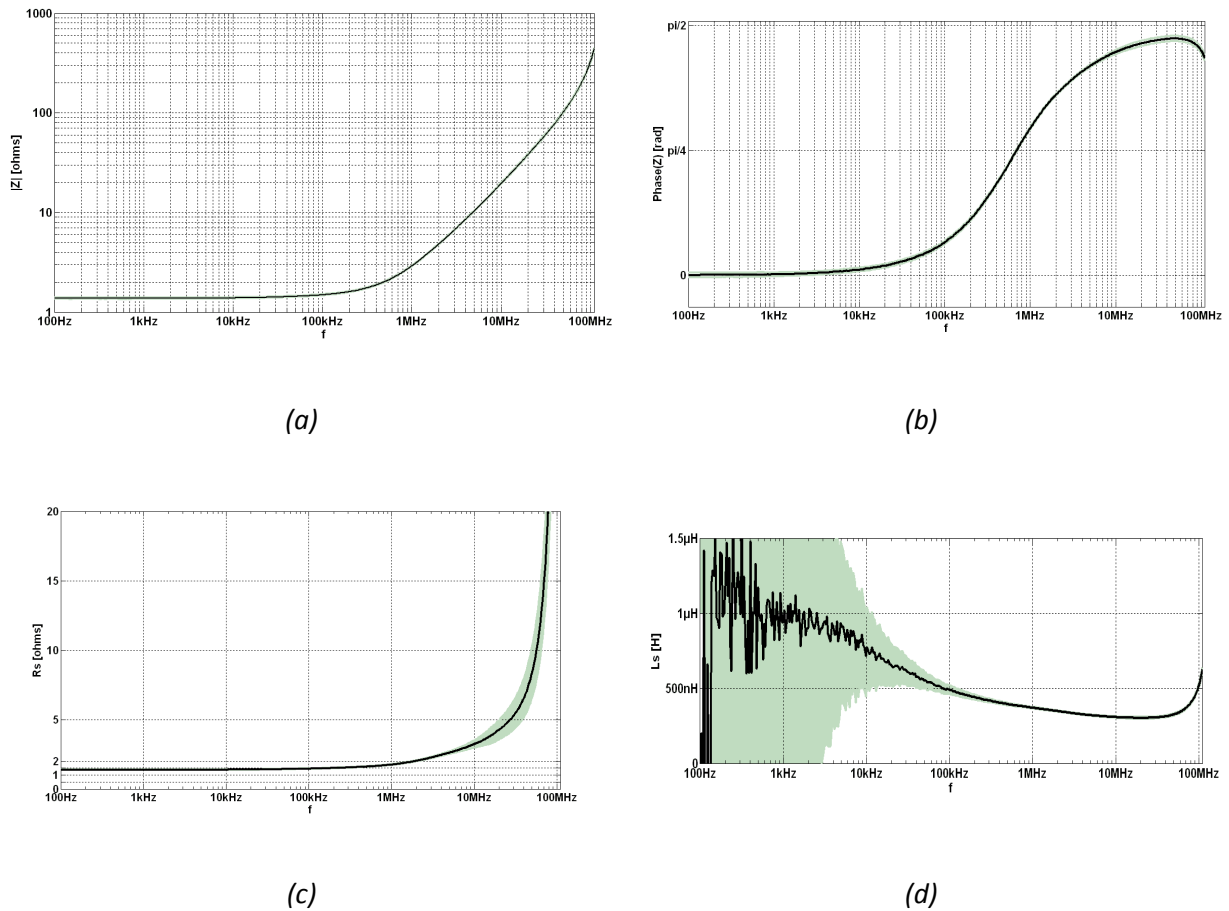


Fig. 4.13 - Measurement of T8 inductor prototype with uncertainty zone in grey. (a) Impedance magnitude. (b) Impedance phase. (c) Equivalent resistance. (d) Equivalent inductance.

B - High frequency measurement

For higher frequency measurements, from about 100 MHz, the accurate auto-balancing bridge method described above cannot be employed anymore. Even if real impedance measurement methods exist, for instance the RF-IV method implemented by Agilent Technologies in the E4991A RF impedance analyzer [Agilent6_tech], the most common method uses Vector Network Analyzers (VNA) [Agilent2_tech]. Those instruments implement a totally different approach, based on the definition of impedance given by microwave theory. In its fundamental form, network analysis involves the measurement of incident, reflected, and transmitted waves that travel along transmission lines. It takes advantage of those properties associated with the reflection and transmission of electrical signals known as scattering parameters (S-parameters).

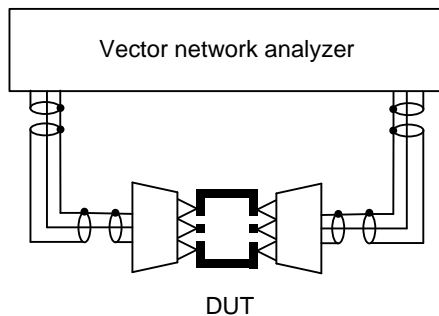


Fig. 4.14 – Vector network analyzer probing system



Fig. 4.15 - Vector network analyzer experimental bench

As our components were designed in two-port configuration, we performed measurements of the S-parameter 2x2 matrix, even if, as for the RF approach with 4294A, it would have been interesting to have one port configuration components to limit the access parasites. This approach, involving the only reflection coefficient Γ , will be envisaged for later wafer processes. In the two-port configuration, it is possible to express Z-parameters in terms of S-parameters:

$$\begin{bmatrix} Z_{11} & Z_{12} \\ Z_{21} & Z_{22} \end{bmatrix} = Z_0 \begin{bmatrix} \frac{(1 + S_{11})(1 - S_{22}) + S_{12}S_{21}}{(1 - S_{11})(1 - S_{22}) - S_{12}S_{21}} & \frac{2S_{12}}{(1 - S_{11})(1 - S_{22}) - S_{12}S_{21}} \\ \frac{2S_{21}}{(1 - S_{11})(1 - S_{22}) - S_{12}S_{21}} & \frac{(1 + S_{22})(1 - S_{11}) + S_{12}S_{21}}{(1 - S_{11})(1 - S_{22}) - S_{12}S_{21}} \end{bmatrix} \quad (4.8)$$

where $Z_0 = 50\Omega$ is the line characteristic impedance.

Then, defining the impedance of the DUT as the ratio of the primary voltage over the primary current, when the second port is shorted (*caution, this is different from the definition of Z_{11}*):

$$Z = \frac{U_1}{I_1} \Big|_{U_2=0} \quad (4.9)$$

One can calculate the expression of Z in function of the previously calculated Z matrix:

$$Z = \frac{Z_{11}Z_{22} - Z_{12}Z_{21}}{Z_{22}} \quad (4.10)$$

C - Comparison between measurement methods

A comparison between each measurement method has been performed on the same prototype inductor T8. Unfortunately, it has demonstrated that, in actual configuration, the probe station approach, both with the impedance analyzer and the vector network analyzer, does not allow good measurements. We can see on Fig. 4.16 that the serial resonance frequency (SRF) is underestimated with the probe station approach. This is probably due to the parasitic effect of the cables which introduce a consequent distributed LC network that cannot be compensated by the methods described above.

On the contrary, the bonded components approach gives satisfying results. The serial resonant frequency and the low frequency behavior is close to the expected one as will be showed in next part. These measurements have thus been considered as the valuable one and used to validate the theoretical development of previous chapter.

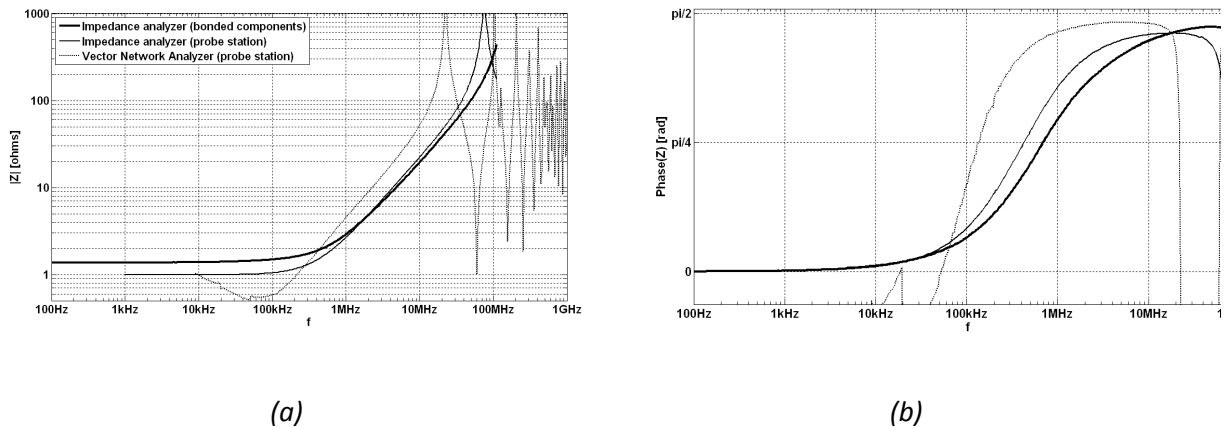


Fig. 4.16 - Measurement of T8 inductor prototype with incertitude zone in grey. (a) Impedance magnitude. (b) Impedance phase. (c) Equivalent resistance. (d) Equivalent inductance.

D - Experimental validation of theoretical study

In order to validate the PEEC approach presented in the previous chapter, we compared the measured and the simulated frequency responses of inductor prototype T8. The geometrical model parameters we entered in the software tool are recapitulated in Fig. 4.17 and Fig. 4.17.

Inductor	Bottom height	Thickness	Internal radius	Width	Space	Number of turns	Conductivity	Relative permittivity	Relative permeability
	z	t	r_{int}	w	s	N	σ	ϵ_r	μ_r
L1	0	15 μ m	290 μ m	75 μ m	75 μ m	8	58.10 ⁶ S.m ⁻¹	1	1
L2	20 μ m	15 μ m	290 μ m	75 μ m	75 μ m	7	58.10 ⁶ S.m ⁻¹	1	1

Fig. 4.17 - Theoretical geometrical and electrical parameters of the conductors of T8 prototype

Layer	Interface height	Resistivity ¹	Relative permittivity	Relative permeability
Air	24 μ m $\leq z \leq +\infty$	0	1	1
SU8 photoresist	0 $\leq z \leq 24\mu$ m	0	3.2	1
Silicon	-400 μ m $\leq z \leq 0$	1k Ω .cm	11.9	1
Air	$-\infty \leq z \leq -400\mu$ m	0	1	1

¹resistivity value of the silicon wafer has been chosen the higher possible to limit eddy currents. Four point resistivity measurements have been performed on wafer surface (0.5 – 4k Ω .cm) and averaged to find the theoretical value.

Fig. 4.18 - Theoretical geometrical and electrical parameters of the layers of T8 prototype

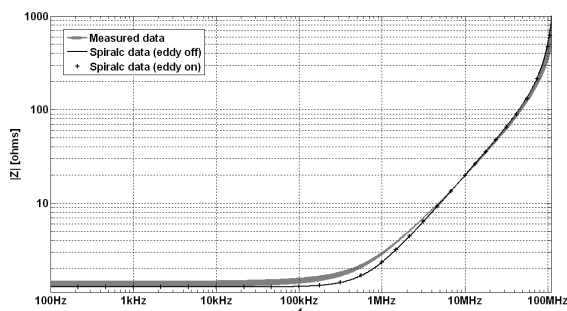
The results are shown in Fig. 4.19. The two PEEC methods, without and with eddy effects, are tested.

The first one consists in computing only one inductance matrix and one capacitance matrix in DC. This method takes every effect into account except skin, proximity and eddy effects which are

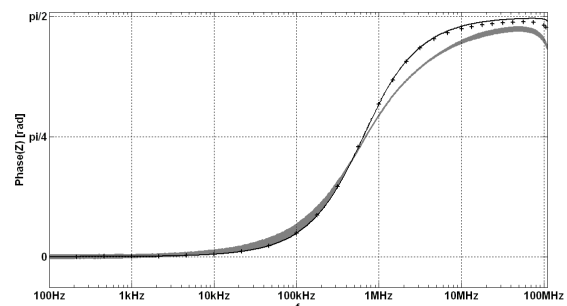
related to induced currents at higher frequency. This is a very fast computing method to determine the general parameters: DC inductance L_{sd} , DC resistance R_{sd} and serial resonance frequency SRF. We can see that this method gives good results in regard to those goals.

The second method aims at also modeling the induced currents effects. It is quite more time consuming since the computation of the admittance matrix is needed at each frequency point. Anyway, the comparison of the curve of this method with the measurement curve shows that general parameters R_{sd} , L_{sd} and SRF are still correctly found out, while, in addition, the equivalent resistance increases more with frequency and equivalent inductance decreases. These phenomena are clearly due to the non uniform distribution of current in conductors and the apparition of induced currents in conductive layers surrounding the conductors. This tends to model the real behavior of the component.

However, some part of the full PEEC model curve is out of the precision domain of the measurement curve, especially at highest frequency points before the resonance. On one hand, this could be imputed to measurement errors, due to a lack of precision in the compensation technique of bond wires and component package. On the other hand, some error can come from the modelization which does not take the exact geometry into account. The rings approximation of the spiral may not be the origin of this imprecision as the DC values are correctly modeled. Several sets of parameters data have been tried to estimate the influence of specific parts of the design on the frequency response, but none has allowed to explain the strong decrease of the equivalent inductance, which can also be viewed as an exaggerated increase of the equivalent resistance, or in the same manner, as a “delay” in the phase “becoming inductive” on measurements. Further measurements will thus provide evidences of the quality of the present ones. Ceramic packages are going to be used, not to induce additional inductive losses in the metallic parts, double bond wires will provide a better contact resistance and short patterns will be bonded as components to in order to make more precise measurements about the parasitic resistance due to packaging.



(a)



(b)

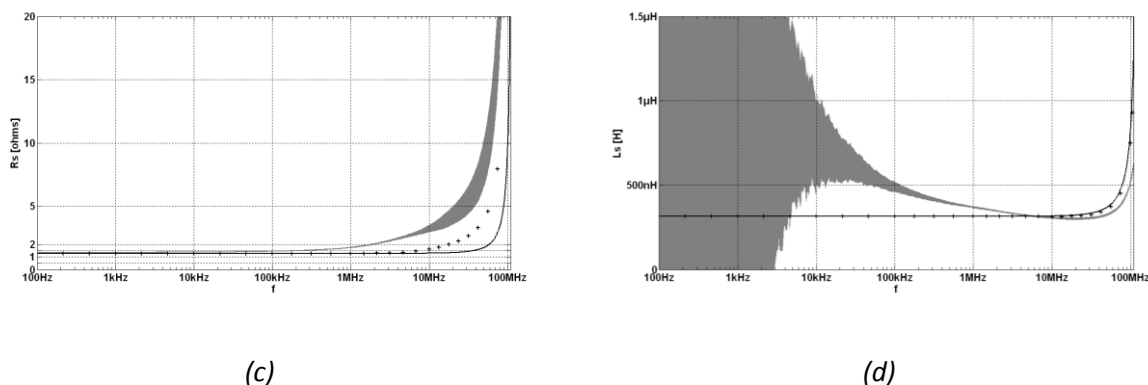


Fig. 4.19 - Measurement of T8 inductor prototype with uncertainty zone in grey compared to simulated values with the PEEC model (with and without eddy effect taken into account). (a) Impedance magnitude. (b) Impedance phase. (c) Equivalent resistance. (d) Equivalent inductance.

5 - Conclusion

In this chapter, we have proposed both a realization process and a measurement methodology for integrated power inductors. Each process step has been developed and shown to be optimized by specific measurements and improvements of the technology. Several measurement methods have also been confronted leading to a good methodology for measurements from very low frequency to 110MHz. Beyond this limit, high frequency measurement method seems not to be appropriate for power inductors which present numerous turns made of large conductors. Further developments may lead to higher frequency measurement ability. The performed measurements, however, provide an encouraging experimental validation of the analytical model proposed in previous chapter for planar circular spiral inductors of many kinds.

Furthermore, the improvements in process technology and measurement techniques will probably allow the realization and characterization of many other passive components like electroplated magnetic core inductors, integrated capacitors, special topology of inductors, LF filters coupling an integrated inductor with an integrated capacitor, etc. These perspectives of applications will be developed in next chapter.

Chapter 5 Applications and perspectives

1 - Introduction

Modeling inductive components is useful for both phenomenon understanding and design optimization. Analytical models are then the most computing time efficient compared to simulations. Unfortunately, specific models must be developed for each application.

In the following study, first, we present an application of the PEEC model developed in previous chapter: multiconductor coils dimensioning for losses reduction in high frequency. We propose a qualitative explanation of the principle of multiconductor windings, as well as a prototype realization.

Another application where electromagnetic modeling has been successfully proposed is the realization of magnetic actuators for microfluidics application. Actually, we propose a full method for modeling the magnetic field generated by any topology of planar coil and, again, we show the realization of effective prototype microfluidic device using such actuators.

2 - Multiconductor

The reduction of equivalent serial resistance of integrated power inductors is the first challenge for designers. As seen in Chapter 2, many kinds of losses are responsible for active losses at low and high frequency. Low frequency losses can be reduced by increasing the cross section of conductors: increasing width of conductors implying a footprint surface increase, thickness of electro-deposits must be increased (*cf. Chapter 4*). This augmentation, however, has consequences on the high

frequency behavior of the component: in addition to substrate and magnetic core losses, skin and proximity effects are enhanced and non homogeneous current distribution in conductors results in greater power dissipation (=losses). This can be easily understood by comparing the power dissipation in

- one conductor with homogeneous current distribution of total dissipated power P (cf. Fig. 5.1.a)
- the same total current split in two conductors of total dissipated power P_1+P_2 (cf. Fig. 5.1.b)

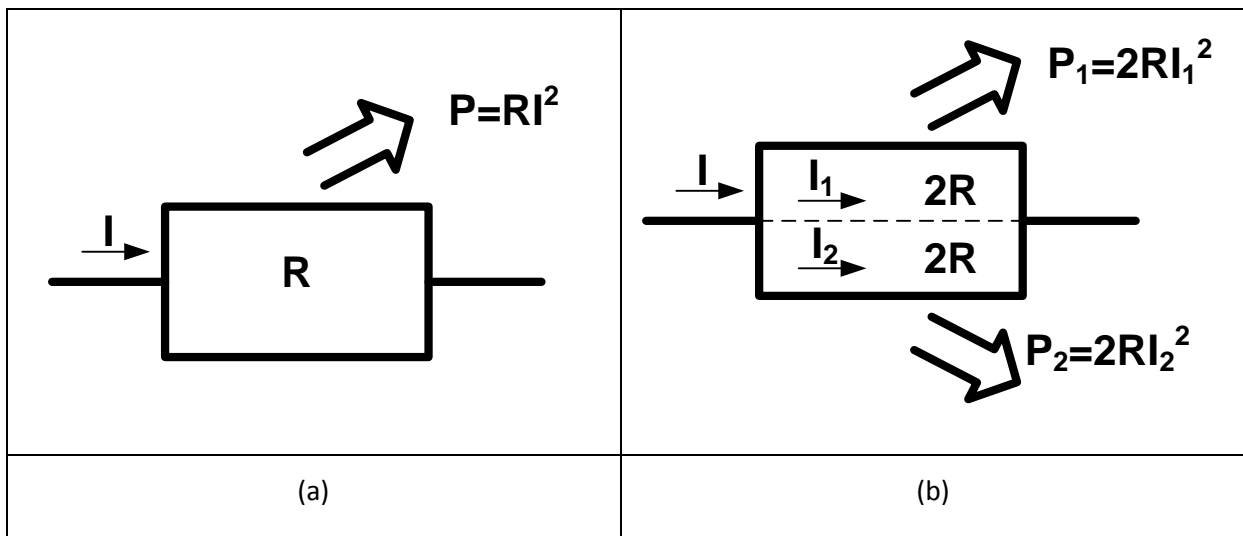


Fig. 5.1 Theoretical study of the influence of current distribution in a conductor on dissipated power

Assuming that the total current is the same in the two cases and defining α , the ratio between the two currents in the split conductor:

$$I = I_1 + I_2 \quad (5.1)$$

$$\alpha = I_1/I_2 \quad (5.2)$$

One can give the expression of the ratio of dissipated powers of inhomogeneous current distribution over homogeneous current distribution:

$$\frac{P_1 + P_2}{P} = \frac{2(1 + \alpha^2)}{(1 + \alpha)^2} \quad (5.3)$$

This ratio is minimum (*lower power dissipation*) when $\alpha = 1$, i.e. when the current distribution is homogeneous. This rule can be generalized to any current distribution and, to the designer's point of view, reducing conductor losses is equivalent to make the current distribution inside homogeneous. In high frequency, inhomogeneity of current is due to skin and proximity effects. These phenomena can be avoided by splitting conductors into several smaller strands electrically insulated. This is

achieved by Litz wire in discrete inductors. Integrated components design can also take benefit from this technique by splitting conductors, under the condition that the total size of the component remains acceptable. Furthermore, stranded conductors can be realized by crossing the two parallel conductors at the center of the inductor as shown on Fig. 5.2.

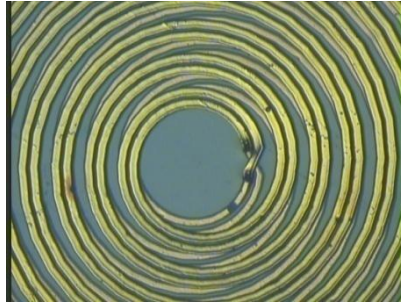


Fig. 5.2 - Zoom top view of crossed multiconductor inductor prototype

Further developments about this technique must be achieved to optimize the compromises between DC resistance value which requires largest conductor cross section and AC resistances which is also depending on the splitting and stranding techniques. These design considerations will be entered as constraints in a design tool implemented in Matlab using SPRIALC engine (*cf. Chapter 4*).

3 - Paramagnetic microbeads actuator

A - Magnetic actuators for microbeads handling in microfluidics devices

The magnetic separation technique in microfluidic analytical applications provides easy handling of biomolecules or biological cells and organelles, which are immobilized on magnetic particles like paramagnetic microbeads. Standard microbeads diameter is generally about 1 to 10 μm depending on the size of the biological element to characterize. There is a wide range of available industrial products proposing various physical properties, *i.e.* mass density (0.1 to 5 g.cm^3), magnetic susceptibility (*depending on material*), magnetic saturation field (*less than 1 Tesla excitation is generally considered as linear zone*), *etc.* The biological elements can then be separated and transported by controlling magnetic fields produced by any magnetic actuator.

First, biologists used to employ external permanent magnets or electromagnets, which now tend to be replaced, in most cases, by integrated actuators [Choi2001]. Literature gives numerous examples of magnetic microsources based on coils [Smistrup2005, Smistrup2006, Liu2005 & Ramadan2006] or various shaped actuators that make use of the magnetic induction effects generated by electric conductors using the induction phenomenon, like serpentine, Y-shape wires...

A wide range of elementary functions can be achieved by combining the microfluidic processes and the inducting actuators. Fig. 5.3 shows an example of a bead trapping system which is the most common application [Ramadan2006]. This can be combined with matrix addressing methods to make arrays of testing zones leading to very efficient labs-on-chip. The Giant Magneto-Resistance sensors are commonly associated to that kind of devices as they permit a reliable measurement of bead population. Fig. 5.4 presents a diverter: particles are diverted via an external uniform magnetic field perturbed at the micro scale by underlying current straps [Pekas2005]. The resulting magnetic force deflects particles across a flow stream into one of the two channels at a Y-shaped junction.

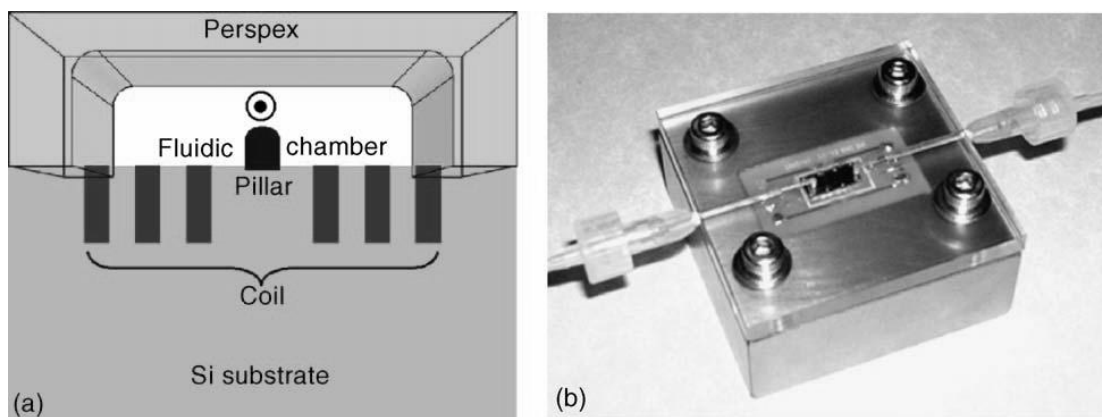


Fig. 5.3 - A bead trapping microfluidics device realized by the Institute of Microelectronics, the Institute of Bioengineering and Nanotechnology and Nanyang Technological University of Singapore. (a) Schematic drawing of the device with the fluidic chamber capping the coil connection block and (b) final fluidic block with chip inserted in it.

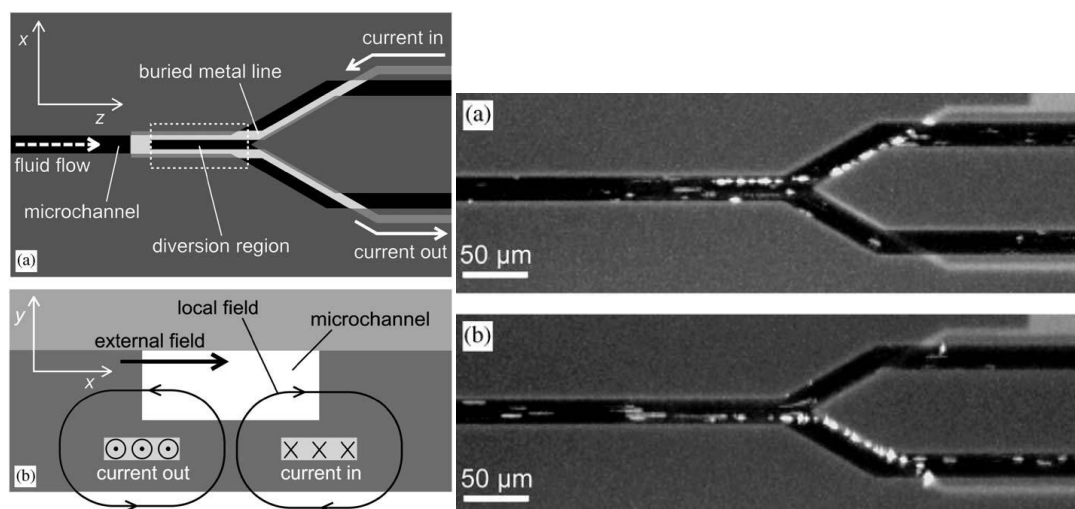


Fig. 5.4 - Magnetic particle diverter in an integrated microfluidic format realized at Institute for Combinatorial Discovery, Iowa, USA.

Depending on the application and the inductive actuator shape, the designer needs a specific and precise model for the magnetic field generated. Several modeling methods, including finite element

and analytical methods, are reported are available in literature and a general 3D field predicting analytical method has been developed for our applications. This issue will be developed in next part.

B - Magnetic field calculus in a spiral inductor actuator

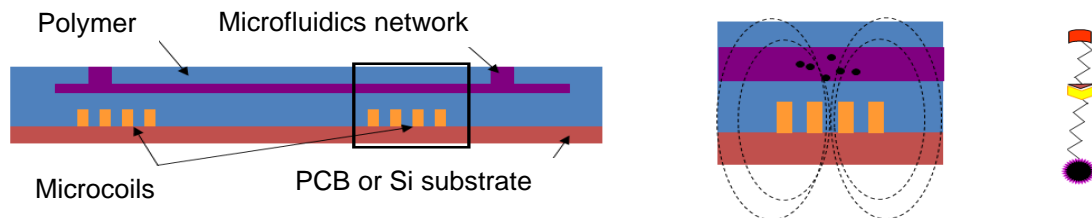


Fig. 5.5 - Microfluidic application of spiral inductor actuator

We have developed an analytic modeling method for the calculus, at any point of the space of the magnetic field created by the actuator excited by a DC current. This methodology is based on the geometrical description of actuators decomposed in approximated elementary structures so called segments. The magnetic field is then computed for each segment and, finally, the total magnetic field is obtained as the vector sum of the previously computed fields. The precise knowledge of this field at any point of the space allows a better understanding of actuators behavior and the computation of the magnetic force applied to a paramagnetic bead. The fundamental equation of the magnetic force applied to a magnetic bead is:

$$\mathbf{F} = K \cdot (\mathbf{B} \cdot \nabla) \mathbf{B} \quad (5.4)$$

where \mathbf{F} is the force, K a constant depending on the magnetic particle properties and \mathbf{B} is the magnetic field. In this way, a better design can be performed for each application.

We present the methodology and provide an illustration of its possibilities through examples of various shapes of actuators (square spiral, circular spiral, serpentine and single spire). The efficiency and the validity domain of the method are also studied according to theoretical observations and also to a comparison with finite element method simulations.

The coil in the coordinate system \mathfrak{R} should be considered as a set of elementary segments. During a first work phase, the evaluation of the magnetic field \mathbf{B} at a given point is determined for each segment constituting the coil in a coordinate system \mathfrak{R}' using a translation and a transition matrix. Upon completion of the various calculations, the total field of the coil in the coordinate system \mathfrak{R} is evaluated by summing the set of each of the elementary fields (*associated with a yarn*) calculated in the coordinate system \mathfrak{R}' and reported into the coordinate system \mathfrak{R} .

a - Description of the coil

A segment of the coil is considered as a filament yarn. Each of the filament yarns is represented by a segment $[\alpha_i\omega_i]$ in which the associated current is supplied at the point α_i . It should be noted that the intensity of the current may be different from one yarn to another. The set of coordinates of points α_i and ω_i is defined in the same coordinate system \mathfrak{R} .

During this study, several primary algorithms were developed in order to generate the set of the N_{seg} segments representing various planar coils. For instance, a square and/or rectangular shape planar coil is represented by the segments defined on Fig. 5.6. The geometrical (*number of turns, inter-turn distance, etc.*) and electrical parameters (*common intensity of the segment set*) of the coil must be entirely defined.

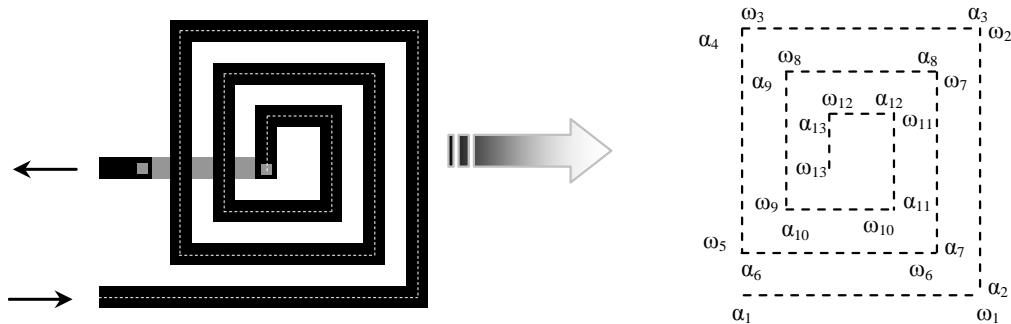


Fig. 5.6 - Equivalent topology of planar inductance

b - Expression of the magnetic field generated by a single segment in the coordinate system \mathfrak{R}'

Let the segment $[\alpha\omega]$ and the point M at which the field \mathbf{B} is calculated. An orthonormal coordinate system \mathfrak{R}' having an origin α is defined, in which the Ox axis bears the $[\alpha\omega]$ segment and in which the point M is included in the plane $(x'Oy')$.

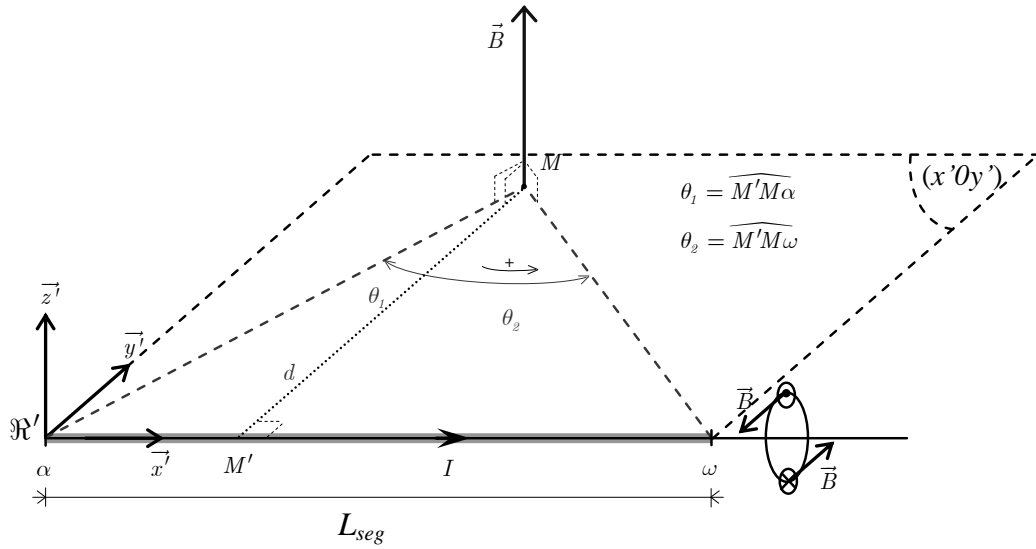


Fig. 5.7 - Magnetic field generated by a the segment $[\alpha\omega]$ at the point M

As the domain of the angles defined in Fig. 5.7 is $\theta_1, \theta_2 \in \left] -\frac{\pi}{2}; \frac{\pi}{2} \right[$, the following relations are checked:

$$\tan(\theta_1) = -\frac{x}{d} \Leftrightarrow \theta_1 = -\tan^{-1}\left(\frac{x}{d}\right) \quad (5.5)$$

$$\tan(\theta_2) = \frac{L_{seg} - x}{d} \Leftrightarrow \theta_2 = \tan^{-1}\left(\frac{L_{seg} - x}{d}\right) \quad (5.6)$$

with L_{seg} being the length of the segment $[\alpha\omega]$. Hence, the calculation of field $\mathbf{B}(x', y', z')$ of the form [Perez_book]:

$$\mathbf{B}(x', y', z') = \frac{\mu_0 I}{4\pi d} [\sin(\theta_1) - \sin(\theta_2)] \cdot \mathbf{x}' \quad (5.7)$$

✓ **Determination in the coordinate system \mathfrak{R} of the field \mathbf{B} generated by all the segments**

The following figure represents the coordinate system \mathfrak{R} in which the segment $[\alpha\omega]$, and the point M are defined as well as the associated coordinate system \mathfrak{R}' . Note that in the diagram the representation of the translation vector \mathbf{T} and the application of the transition matrix \mathbf{P} are defined in the following part.

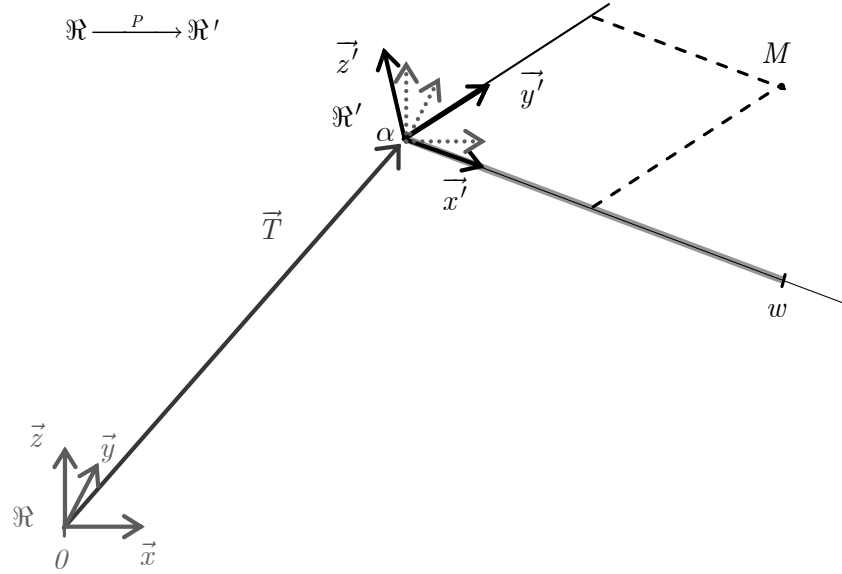


Fig. 5.8 - Change of coordinate system between \mathfrak{R} and \mathfrak{R}' for a segment

✓ **Mathematical tools for a change of coordinate system between \mathfrak{R} and \mathfrak{R}'**

The coordinate system \mathfrak{R}' is obtained from the coordinate system \mathfrak{R} using a \mathbf{T} vector translation and a linear transformation represented by the unit transition matrix \mathbf{P} . Accordingly, the relation for the transition of the co-ordinates of the point M in \mathfrak{R}' to the coordinates of the point M in \mathfrak{R} is expressed as follows:

$$\overrightarrow{OM}|_{\mathfrak{R}} = \mathbf{T}|_{\mathfrak{R}} + \mathbf{P} \cdot \overrightarrow{\alpha M}|_{\mathfrak{R}'}, \quad (5.8)$$

The translation vector \mathbf{T} and the transition matrix \mathbf{P} are obtained from the following vector relations:

$$\mathbf{T} = \overrightarrow{O\alpha} \quad (5.9)$$

$$\mathbf{x}' = \frac{\overrightarrow{\alpha\omega}}{\|\overrightarrow{\alpha\omega}\|} \quad (5.10)$$

$$\mathbf{z}' = \frac{\overrightarrow{\alpha\omega} \times \overrightarrow{\alpha M}}{\|\overrightarrow{\alpha\omega} \times \overrightarrow{\alpha M}\|} \quad (5.11)$$

$$\mathbf{y}' = \overrightarrow{\mathbf{z}'} \times \overrightarrow{\mathbf{x}'} \quad (5.12)$$

Knowing the coordinates of the points M , α and ω , it is possible to determine the coordinates of the vector \mathbf{T} (equal to those of the point α) and the coefficients of the matrix \mathbf{P} by concatenation of \mathbf{x}' , \mathbf{y}' and \mathbf{z}' :

$$\mathbf{P} = [\mathbf{x}'|\mathbf{y}'|\mathbf{z}'] \quad (5.13)$$

c - Application of the method for changing coordinate systems to the evaluation of the total magnetic field.

The total magnetic field is obtained by summing each of the components \mathbf{B}_i generated by the associated segment $[\alpha_i \omega_i]$:

$$\mathbf{B}_{\text{tot}}|_{\mathfrak{R}} = \sum_{i=1}^{N_{\text{seg}}} \mathbf{B}_i |_{\mathfrak{R}} \quad (5.14)$$

The method for calculating the components \mathbf{B}_i described above provides said components in the coordinate system \mathfrak{R}'_i relative to the segment $[\alpha_i \omega_i]$. The coordinates of \mathbf{B}_i in \mathfrak{R} are expressed as follows:

$$\mathbf{B}_i |_{\mathfrak{R}} = \mathbf{P} \cdot \mathbf{B}_i |_{\mathfrak{R}'_i} \quad (5.15)$$

The coordinates of point M are expressed in the coordinate system \mathfrak{R} of the coil. In order to calculate each of the components \mathbf{B}_i , it is necessary to report these coordinates into \mathfrak{R}'_i according to the expression:

$$\overline{\alpha_i \mathbf{M}} |_{\mathfrak{R}'_i} = \mathbf{P}^T \cdot (\overline{\mathbf{OM}} |_{\mathfrak{R}} - \mathbf{T} |_{\mathfrak{R}}) \quad (5.16)$$

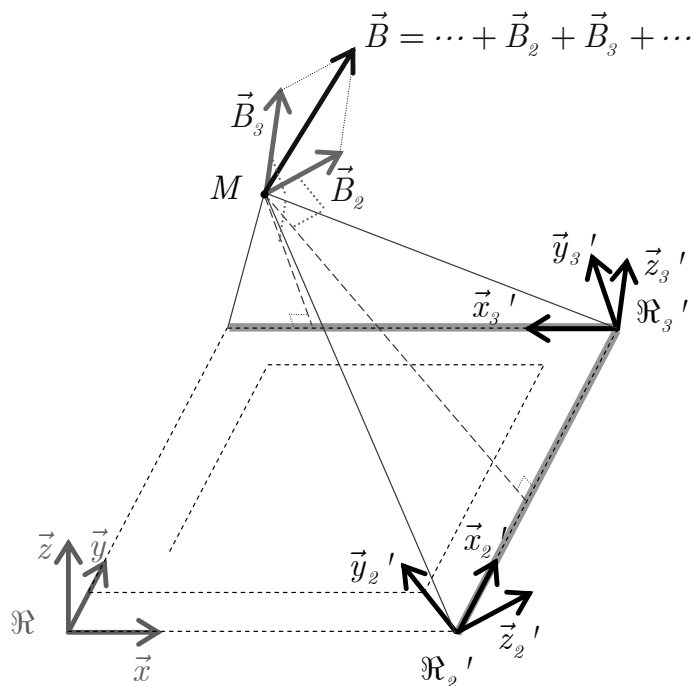


Fig. 5.9 - Graphic representation of the evaluation of the total B field

d - Comparison of the computed magnetic fields using the analytic calculation and the finite element method

The following figure (Fig. 5.10) represents the layout of four models of coils that have been realized for the MAGIMICS project hold in LAAS-CNRS. The analytic evaluation of the magnetic field generated by the coil at different heights z of the plane thereof is represented in the following diagrams. The following diagrams represent the comparison results (analytic/FEM) of the magnitude of the field \mathbf{B} along a longitudinal axis at different heights z from the coil. These results validate our analytical approach.

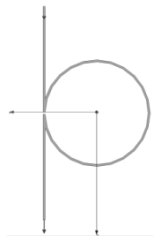
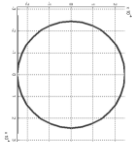
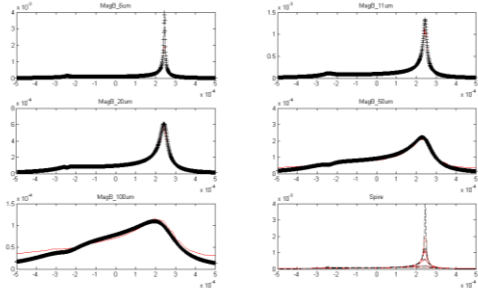
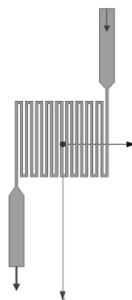
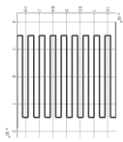
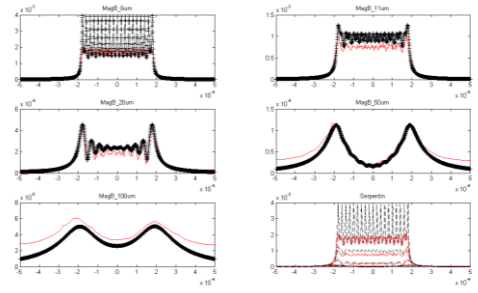
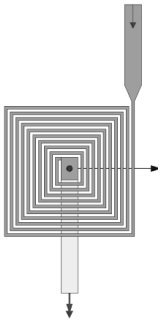
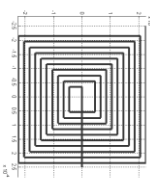
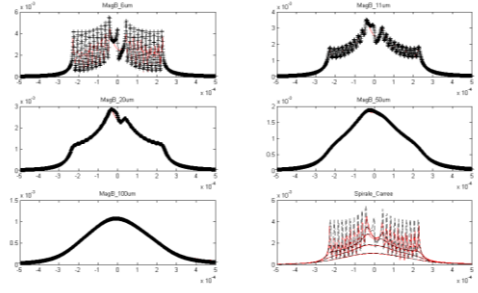
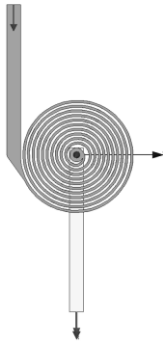
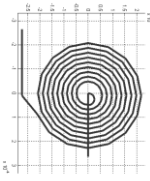
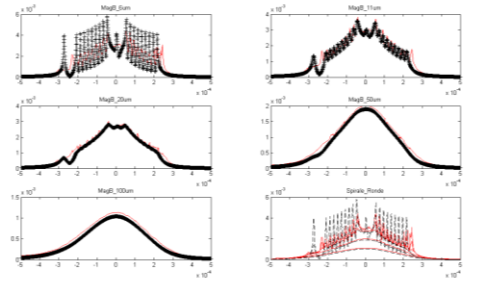
	<p>FEA method Implemented in Maxwell3D</p>	<p>Analytic method Implemented in Matlab</p>	<p>Analytic vs FEA results In terms of B along y-axis at different height on z-axis: $z = \begin{bmatrix} 6\mu\text{m} & 11\mu\text{m} \\ 20\mu\text{m} & 50\mu\text{m} \\ 100\mu\text{m} & \text{ALL} \end{bmatrix}$</p>
<p>Omega</p>			
<p>Serpentine</p>			
<p>Square Coil</p>			 <p style="text-align: center;">(zoom: cf. Fig. 5.11)</p>
<p>Circular Coil</p>			

Fig. 5.10 - Comparison (analytic/FEM) of the fields Bds depending on the height Z

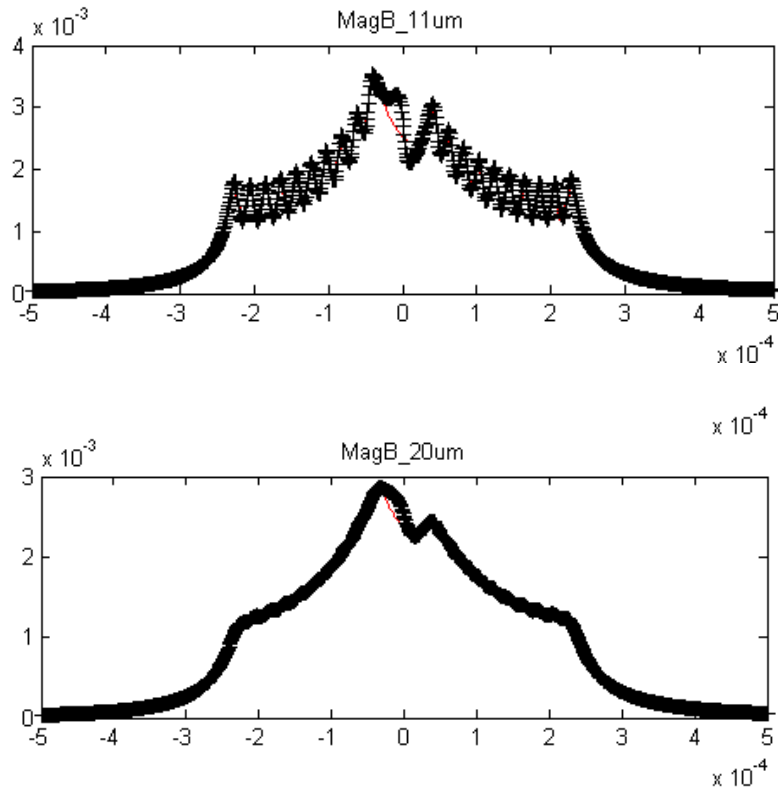


Fig. 5.11 – Magnetic field created by a square coil along a horizontal axis at 11 and 20 μm from the center computed both with analytical model (*black crosses curve*) and FEA method (*red curve*)

The above study essentially relates to the description of the modeling of a magnetic field generated by a coil having a planar winding. In this view, an analytical modeling was used and a specific topology was studied. At the end of this study, a similar topology was treated using the finite element method. Finally, the analytical model presented was validated by the comparison of the two approaches. As the objective of the whole project is the handling of paramagnetic beads in fluid micro-systems, the forces generated by the coil field necessary for magnetic actuation will be particularly examined in the future.

C - Prototypes of microfluidics device with magnetic actuator and perspectives

The dimensioning of components has been enabled both by simulation and analytical study. Even if further developments to precisely compute the force applied on beads, including the influence of beads on themselves, are needed, a first prototype has been realized according to preliminary calculus presented above.

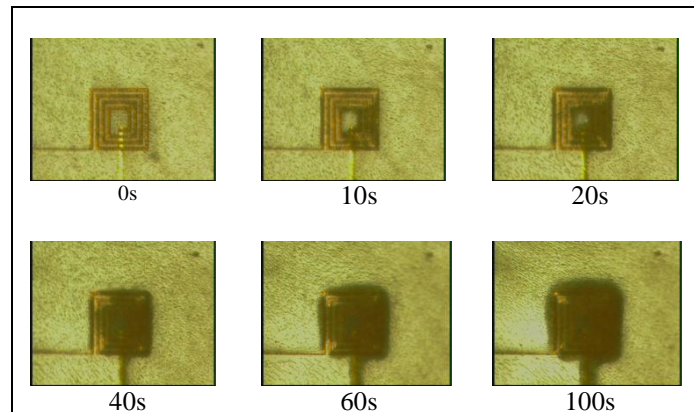


Fig. 5.12 - Images taken from a movie and showing beads stopped by the coil under an intensité $I = 50 \text{ mA}$

By imposing a current with intensity $I = 50 \text{ mA}$, we observed the trapping of Dynal® microbeads (*Dynabeads® M-500 Subcellular and M-270 Carboxylic Acid with diameter $5.0\mu\text{m}$ and $2.7\mu\text{m}$*) flowing through a channel. One can see on Fig. 5.12 that during the actuation, microbeads are attracted by the coil. These results are very encouraging for the following developments of magnetic actuators. Actually, technological improvements in conductor thickness, magnetic cores, *etc.* can be used for those devices. To the theoretical point of view, modelization of force is kind of easy as numerical gradient calculus functions are already implemented in Matlab. Magnetic core implementation and bead over bead influence are considered as challenges at present. Thermal and fluidic simulations would also be interesting for a complete optimization of the device.

4 - Conclusion

In this chapter, we presented prototypes of integrated coils for power conversion application as well as microfluidic magnetic actuation. The good knowledge of the electromagnetic behavior of such components acquired by the previous study has been adapted to specific needs.

First, multiconductor realizations of circular spiral inductors has been presented as a possible design of inductive components leading to the reduction of skin and proximity effect in conductors and thus to a further reduction of active losses in the component. This topology optimization is a typical example of the use of the analytical model developed in previous chapter: compromises about size, DC and AC losses, *etc.* can be entered as constraints and systematic study can be performed.

In a second time, a model has been presented of the magnetic field created by any topology of planar inductor. This model has been applied to the case of magnetic actuation for microfluidic

Conclusion

devices and validated by comparison with Finite Element Analysis computation. This method is very precise and optimization can be performed again. Further developments will lead to a good model of the total force applied to the paramagnetic beads.



Conclusion

The objective of this work was the systematic study of power integrated inductors for embedded system power supplies. As we discussed in chapter 1, planar circular spiral inductors, with or without magnetic core, are very likely to allow the full integration of switching mode power converters. The miniaturization induced by integration, however, implies that every kind of electrical losses (*described in chapter 2*) must be taken into account to provide a reliable model of those inductive components. We thus developed a fast computing software tool, called SPIRALC, which implements the Partial Element Equivalent Circuit (*PEEC*) method adapted to any rotational symmetry problem. This tool is general enough to allow the description of any circular component and its frequency response computation, including skin and proximity effects in conductors, eddy current in substrate layers and magnetic core and capacitive effects between conductors. Magnetic cores can also be simulated since relative permeability can be entered for each layer, under the condition that their design respects rotational symmetry (*vertically laminated cores cannot be modeled by this method*). Hysteretic losses could be approximated by linearized complex permeability, although this feature remains to be tested. Actually, many methods have been tested and compared to compute the frequency response of our circular spiral components, from full analytical study to global Finite Element Method (FEM) simulations, also including hybrid methods, and the proposed modeling method is the best compromise we found between computing time and model precision (*cf. Chapter 3*).

The validity of our model has been checked by comparison with FEM simulations and experimental measurements on inductor prototypes. The theoretical simulations are in excellent agreement with our simulations, which means that every standard electromagnetic phenomena mentioned above are well taken into account by the model. Experimental validation is acceptable since equivalent serial inductance and resistance (*ESR*), and serial resonance frequency (*SRF*), are precisely determined. However, the frequency behavior of real components still encounters undecided questions: active losses seem to be much more increasing than the models prediction and/or phase determination of the impedance frequency response is quite imprecise with the

measurement methods. The process and the characterization method are fully described in chapter 4. Technological process allows the realization of quality devices with simple, reliable and reproducible techniques. We suppose that bonded components characterization did not provide precise enough measurement data because of the additional AC resistance due the packaging, but this hypothesis needs to be further investigated. Either measurement technique or model precision could be further ameliorated by answering this question.

By the way, prototypes have demonstrated the feasibility of high inductance integrated components and the integration of several electrical functions, or even micro electromechanical system (*MEMS*), are from now onwards possible. The opportunity of collaborations in the lab has lead to the study of inductors for magnetic actuators applications which is presented in chapter 5. Microfluidic systems using paramagnetic bead actuation are more and more encountered, especially in biological analysis domain. The model of the magnetic field generated by inductive actuators will be completed by the full modelization of the forces applied to microbeads in these applications, thus allowing the dimensioning of actuators. Another collaboration has begun for the development of a full process combining the realization of inductors and capacitors in order to achieve a second order LC filter for power applications. At LAAS-CNRS, capacitors are made by Deep Reactive Ion Etching (*DRIE*) of trenches in the doped substrate with a $\text{SiO}_2(5\text{nm})/\text{Si}_3\text{N}_4(20\text{nm})$ dielectric layer deposit and another polysilicon deposit is used to make the second electrode. The surface capacitance is about $60\text{nF}/\text{mm}^2$, the equivalent serial resistance is about 1Ω and the resonance frequency is about 30MHz [Benazzi2007]. These performances are good compared to what can be found in literature [Roozeboom2006], however, improvements are still to be made to integrate a sufficient LC filter working in a converter of switching frequency 1MHz . The equivalent serial resistance must be reduced (*as for inductors*) by further doping of silicon or replacing the top electrode by other materials, and increasing the shape factor of the trenches would provide higher values of capacitance. Last mask sets of capacitor and inductor prototypes have been designed to be compatible with each other. Processes have been developed separately and they will be done successively on the same substrate. Performances of separate components are well known now, but the influence of one over another, especially, the presence of the magnetic field generated by the inductor inside the capacitor still have to be studied. LC filters with separate inductor and capacitor have also been designed in order to observe the impact of components over one another.

References

Publications

- [Abedinpour2006] S. Abedinpour, B. Bakkaloglu & S. Kiaei, "A 65MHz switching rate, two-stage interleaved synchronous buck converter with fully integrated output filter", IEEE International Symposium on Circuits and Systems (ISCAS'06), pp.5315-5318, 2006.
- [Aime2008] J. Aime, E. Clavel, J. Roudet, Ph. Baudesson, "Magnetic field computation of a common mode filter using Finite Element, PEEC methods and their coupling", IEEE International Symposium on Industrial Electronics (ISIE'08), Cambridge, United Kingdom, pp.7-12, July 2008.
- [Artillan2007] Ph. Artillan, B. Estibals, A. Salles, J. Abboud, P. Aloïsi & C. Alonso, "A PEEC approach for circular spiral inductive components modeling", IEEE International Symposium on Circuits and Systems (ISCAS'07), pp. 301-304, 2007.
- [Artillan2008] Ph. Artillan, B. Estibals, C. Alonso, "A new modeling approach for circular spiral inductors", 12th European Conference on Power Electronics and Applications (EPE 2007), Aalborg, pp. 1-8, 2007.
- [Artillan2008a] Ph. Artillan, B. Estibals & C. Alonso, "A very fast computing and accurate formula for the mutual inductance of two circular wire loops", submitted to IEEE International Conference on Industrial Technology (ICIT'09), 2009.
- [Benazzi2007] A. Benazzi, M. Brunet, P. Dubreuil, N. Mauran, L. Bary, J.-P. Laur, J.-L. Sanchez, K. Isoird, "Performance of 3D capacitors integrated on silicon for DC-DC converter applications", European Conference on Power Electronics and Applications (EPE'07), pp. 1-9, 2-5 Sept. 2007 .
- [Burghartz2003] J.N. Burghartz & B. Rejaei, "On the Design of RF Spiral Inductors on Silicon", IEEE transactions on electron devices, vol. 50, no 3, pp. 718-729, 2003.
- [Boggetto2002] J.M. Bogetto, Y. Lembeye, J.P. Ferrieux, Y. Avenas, "Microfabricated power inductors on silicon", IEEE 33rd Annual Power Electronics Specialists Conference (PESC), vol. 3, pp. 1225-1229, 23-27 June 2002.
- [Chan2003] H. Chan, K. Cheng & D. Sutanto, "Calculation of inductances of high frequency air-core transformers with superconductor windings for DC-DC converters", IEEE Proceedings on Electronics: Power Applications, vol. 150, pp. 447-454, 2003.
- [Choi2001] J.-W. Choi, T. M. Liakopoulos, C. H. Ahn, "An on-chip magnetic bead separator using spiral electromagnets with semi-encapsulated permalloy", Biosensors and Bioelectronics Journal, vol. 16, pp; 409-416, 2001.

References

- [Greenhouse1974] H. Greenhouse, "Design of planar rectangular microelectronic inductors", IEEE Transactions on Parts, Hybrids, and Packaging, vol. 10, pp. 101-109, 1974.
- [Helie2004] J.-F. Helie, "Les convertisseurs DC-DC de proximité", Revue électronique n°147, May 2004.
- [Hurley1999] W. G. Hurley, M. C. Duffy, S. O'Reilly & S. C. O'Mathuna, "Impedance formulas for planar magnetic structures with spiral windings", IEEE transactions on industrial electronics, vol. 46, no. 2, pp. 271-278, Apr. 1999.
- [Kamon1994] M. Kamon, M. J. Tsuk & J. White, "FastHenry: a multipole-accelerated 3-D inductance extraction program", IEEE transactions on microwave theory and techniques, vol. 42, no. 9, Sept. 1994.
- [Kamon1998] M. Kamon, N.A. Marques, L.M. Silveira, & J. White, "Automatic Generation of Accurate Circuit Models of 3-D Interconnect", IEEE Transactions on components, packaging and manufacturing technology, vol. 21, pp. 225-240, 1998.
- [Leplus1986] F. Leplus, "Bobine à noyau de fer en régime variable", Techniques de l'ingénieur art. D3010, post 1986.
- [Lim2007] M.H.F. Lim, Z. Liang, J.D. van Wyk, "Low profile integratable inductor fabricated based on LTCC technology for microprocessor power delivery applications", IEEE transactions on components and packaging technologies, vol. 30, issue 1, pp. 170-177, March 2007.
- [Liu2000] M. Liu, W. W.-M. Dai, "Modeling and Analysis of Integrated Spiral Inductors for RF System-in-Package", Proceedings of the ASP-DAC Design Automation Conference, Asia and South Pacific, pp. 211 – 216, 2000.
- [Liu2005] Y. Liu, H. Lee, R. M. Westervelt & D. Ham, "IC/Microfluidic hybrid system for biology: review", proceedings of the IEEE Bipolar/BiCMOS Circuits and Technology (BCTM) meeting, pp. 174 – 179, 9-11 Oct. 2005.
- [Mei2003] S. Mei & Y. Ismail, "Modeling skin effect with reduced decoupled R-L circuits", proceedings of the 2003 International Symposium on Circuits and Systems (ISCAS '03), vol. 4, pp. 588-591, 2003.
- [Munusuri2005] S. Musunuri, P.L. Chapman, Jun Zou, Chang Liu, "Design issues for monolithic DC-DC converters", IEEE Transactions on Power Electronics, vol. 20, issue 3, pp. 639 – 649, May 2005.
- [Munusuri2005a] S. Musunuri, P.L. Chapman, "Design of Low Power Monolithic DC-DC Buck Converter with Integrated Inductor", IEEE 36th Power Electronics Specialists Conference (PESC), pp. 1773 - 1779, 2005.
- [Nastos2006] N. Nastos & Y. Papananos, "RF Operation of MOSFETs Under Integrated Inductors", IEEE transactions on microwave theory and techniques, vol. 54, pp. 2106-2116, May 2006.
- [Niknejad1998] A.M. Niknejad & R.G. Meyer, "Analysis, Design, and Optimization of Spiral Inductors and Transformers for Si RF IC's", IEEE Journal of solid state circuits, vol. 33, pp. 1470-1481, 1998.
- [Pan2005] T. Pan, A. Baldi, E. Davies-Venn, R. F. Drayton & B. Ziaie, "Fabrication and modeling of silicon embedded high-Q inductors", Journal of Micromechanics and Microengineering, vol. 15, pp. 849-854, 2005.
- [Park2003] J.-W. Park, M. G. Allen, "Ultralow-profile micromachined power inductors with highly laminated Ni/Fe cores: application to low-megahertz DC-DC converters", ; IEEE

- Transactions on magnetics, vol. 39, issue 5, part 2, pp. 3184-3186, Sept. 2003.
- [Park2004] J.-W. Park, F. Cros, M. G. Allen, "*Planar spiral inductors with multilayer micrometer-scale laminated cores for compact-packaging power converter applications*", IEEE transactions on Magnetics, vol. 40, issue 4, part 2, pp. 2020-2022, July 2004.
- [Pekas2005] N. Pekas, M. Granger, M. Tondra, A. Popple & M. D. Porter, "*Magnetic particle diverter in an integrated microfluidic format*", Journal of Magnetism and Magnetic Materials, vol. 293, pp. 584–588, 2005
- [Putot1999] S. Putot, F. Charlet, & P. Witomski, "*A new algorithm for interconnect capacitance extraction based on a fictitious domain method International*", Conference on Simulation of Semiconductor Processes and Devices SISPAD'99, pp.79 – 82, LETI (CEA-Technologies Avancées), LMC-IMAG, Silvaco, 1999.
- [Putot1999a] S. Putot, F.Charlet, & P. Witomski, "*A Fast and Accurate Computation of Interconnect Capacitance*", technical report given by Silvaco, LETI and LMC-IMAG, 1999
- [Ramadan2006] Q. Ramadan, V. Samper, D. P. Poenar & C. Yu, "*An integrated microfluidics platform for magnetic microbeads separation and confinement*", Biosensors and Bioelectronics Journal, vol. 21, pp. 1693-1702, 2006.
- [Rejaei1998] B. Rejaei, J. Tauritz & P. Snoeij, "*A predictive model for Si-based circular spiral inductors*", Topical Meeting on Silicon Monolithic Integrated Circuits in RF Systems (Digest of Papers), pp. 148 – 154, 1998.
- [Rejaei2004] B. Rejaei, "*Mixed-Potential Volume Integral-Equation Approach for Circular Spiral Inductors*", IEEE transactions on microwave theory and techniques, vol. 52, pp. 1820-1829, 2004.
- [Roozeboom2006] F. Roozeboom, A.L.A.M. Kemmeren, J.F.C. Verhoeven, F.C. van den Heuvel, J. Klootwijk, H. Kretschman et al., "*Passive and heterogeneous integration towards a Si-based System in Package concept*", Journal of Thin Solid Films, vol. 504, pp. 391-396, 2006.
- [Ruehli1972] A. E. Ruehli, "*Inductance calculations in a complex integrated circuit environment*", IBM journal of research & development, vol. 16, pp. 470-481, Sept. 1972.
- [Ruehli1974] A. E. Ruehli, "*Equivalent circuit models for three-dimensional multiconductor systems*", IEEE Transactions on microwave theory and techniques, WIT-22, pp. 216-221, 1974.
- [Ruehli1996] A. E. Ruehli, "*Partial Element Equivalent Circuit (PEEC) method and its application in the frequency and time domain*", IEEE International Symposium on Electromagnetic Compatibility, pp. 128 – 133, 19-23 Aug. 1996.
- [Saidani2003] M. Saidani, M.A.M. Gijs, "*Cubic millimeter power inductor fabricated in batch-type wafer technology*", Journal of Microelectromechanical Systems, vol. 12, issue 2, pp. :172 – 178, April 2003.
- [Smistrup2005] K. Smistrup, O. Hansen, H. Bruus & M. F. Hansen, "*Magnetic separation in microfluidics systems using microfabricated electromagnets – experiments and simulations*", Journal of Magnetism and Magnetic Materials vol. 293, pp. 597-604, 2005.
- [Smistrup2006] K. Smistrup, O. Hansen, H. Bruus & M. F. Hansen, "*Microelectromagnet for magnetic manipulation in lab-on-a-chip systems*", Journal of Magnetism and Magnetic Materials, vol. 300, pp. 418-426, 2006.
- [Yue2000] C. P. Yue & S. S. Wong, "*Physical Modeling of Spiral Inductors on Silicon*", IEEE transactions

on electronic devices, vol. 47, no. 3, pp. 560-568, March 2000

- [Wang2007] M. Wang, I. Batarseh, K. D. T. Ngo & H. Xie, "*Design and Fabrication of Integrated Power Inductor Based on Silicon Molding Technology*", IEEE Power Electronics Specialists Conference (PESC), pp. 1612 – 1618, 17-21 June 2007.

PhD Thesis

- [Boggetto_thesis] J.-M. Boggetto, "*Contribution à l'intégration d'une inductance sur silicium et étude de son convertisseur synchrone associé*", PhD Thesis, Laboratoire d'Electronique de Grenoble (LEG), Oct 2003.
- [Escovar_thesis] R. Escovar, "*Tools for impedance extraction in integrated circuits (IC)*", PhD Thesis at Université Joseph Fourier, Grenoble, 2006.
- [Kamon_thesis] M. Kamon, "*Fast Parasitic Extraction and Simulation of Three-dimensional Interconnect via Quasistatic Analysis*", PhD Thesis at Massachusetts Institute of Technology, 1998.
- [Niknejad_thesis] A.M. Niknejad, "*Analysis, Simulation, and Applications of Passive Devices on Conductive Substrates*", PhD Thesis at University of California at Berkeley, 2000.
- [Salles_thesis] A. Salles, "*Conception d'éléments passifs magnétiques pour convertisseurs de faible puissance*", PhD Thesis, Laboratoire d'Analyse et d'Architecture des Systèmes (LAAS-CNRS), pp. 197, 26 Sept. 2008.

Technical reports/datasheets

- [Artillan_tech] Ph. Artillan, C. Alonso, B. Estibals, A. Salles, N. Mauran, H. Tranduc, S. Assie-Souleille, "*Conception et réalisation d'un banc de caractérisation d'éléments inductifs pour la conversion de puissance*", Rapport LAAS-CNRS 05663, 67p. , 2005.
- [Agilent_tech] Agilent Technologies, Inc., "*8 Hints for Successful Impedance Measurements - Application note 346-4*", Agilent reference: 5968-1947E, 2000.
- [Agilent2_tech] Agilent Technologies, Inc., "*Understanding the Fundamental Principles of Vector Network Analysis - Application note 1287-1*", Agilent reference: 5965-7707E, 2000.
- [Agilent3_tech] Agilent Technologies, Inc., "*Agilent 4294A Precision Impedance Analyzer - Datasheet*", Agilent reference: 5968-3809E, jan. 2003.
- [Agilent4_tech] Agilent Technologies, Inc., "*Impedance Measurement Handbook*", Agilent reference: 5950-3000, dec. 2003.
- [Agilent5_tech] Agilent Technologies, Inc., "*Agilent 4284A/4285A Precision LCR Meter Family – Technical overview*", Agilent reference: 5952-1431, may 2004.
- [Agilent6_tech] Agilent Technologies, Inc., "*Agilent E4991A RF Impedance-Material Analyzer – Technical overview*", Agilent reference: 5980-1234E, oct. 2004.
- [Brunet_tech] Magali Brunet, "*Matériaux et technologies pour composants passifs intégrés sur Silicium dans les applications de conversion de l'énergie*", Présentation Vishay, LAAS-CNRS, 18 Apr. 2008.

- [Cascade_tech] Cascade Microtech, "Layout Rules for GHz-Probing", Cascade Microtech application note, url: <http://www.cmicro.com/>, 1987.
- [Clavel_tech] E. Clavel, J.-M. Guichon, "*INCA – Modélisation des caractéristiques électriques de câblage à l'aide de la méthode PEEC*", Laboratoire d'Electrotechnique de Grenoble, Manuel d'utilisation, Dec. 2001.
- [Silvaco_tech] Silvaco, "Quest user manual", 2005.

Books

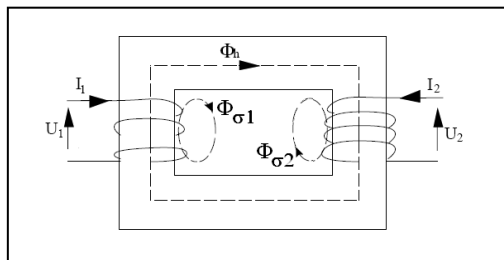
- [Combes_book] P.F. Combes, "Micro-ondes vol. 1– Lignes, guides et cavités", Ed. Dunod, ISBN 2100028405
- [Combes2_book] P.F. Combes, "Micro-ondes vol. 2– Circuits passifs, propagation, antennes", Ed. Dunod, ISBN 2100027530
- [Ferrieux_book] J.-P. Ferrieux & F. Forest, "*Alimentations à découpage, convertisseurs à résonance – Principes, composants, modélisation*", Dunod, 3^e édition, 13 juin 2001.
- [Griffiths_book] D. Griffiths, "*Introduction to electrodynamics*", Prentice Hall (3rd ed.), 1998.
- [Grover_book] F.W. Grover, "*Inductance Calculations: Working Formulas and Tables*", New York, Dover publications, 1946.
- [Mattheij_book] R. M. M. Mattheij, S. W. Rienstra, J. H. M. ten Thije Boonkamp, "*Monographs on Mathematical Modeling and Computation*", ISBN 0-89871-594-6, Siam Edition, 2005.
- [Perez_book] J.-Ph. Pérez, R. Carles, R. Fleckinger, "*Electromagnétisme, Fondements et applications*", Ed. Dunod, ISBN 2 10 0055747, 2002.

Web addresses

- [Ansoft_url] Ansoft software tools website, url: <http://www.ansoft.com/>
- [Comsol_url] Comsol Multiphysics software tool website, url: <http://www.comsol.fr/>
- [Enpirion_url] Enpirion website, url: <http://www.enpirion.com/>
- [Guerin_url] Louis J. Guerin, "*The SU8 homepage*", url: <http://www.geocities.com/guerinlj/>
- [Mapple_url] Mapple software tool website, url: <http://www.maplesoft.com/>
- [Matlab_url] Matlab software tool website, url: <http://www.mathworks.fr/products/matlab/>
- [Mirotznik_url] M. S. Mirotznik, D. Prather, "How to choose an EM software?", The practical engineer, url: <http://ingfi9.die.unifi.it/femcorner/software/sw.html>
- [Silvaco_url] Silvaco software tools website, url: <http://www.silvaco.com/>

Appendix

Appendix - Real transformer



A representation of a real transformer

Physical quantities of the real transformer are defined in the next table:

	Primary	Secondary
Input voltage	U_1	U_2
Input intensity	I_1	I_2
Serial resistance	R_1	R_2
Proper flux	ϕ_{h11}	ϕ_{h22}
Induced flux	ϕ_{h12}	ϕ_{h21}
Leakage flux	$\phi_{\sigma 1}$	$\phi_{\sigma 2}$
Proper inductance	L_{1h}	L_{2h}
Leakage inductance	$L_{1\sigma}$	$L_{2\sigma}$
Total inductance	$L_{1T} = L_{1h} + L_{1\sigma}$	$L_{2T} = L_{2h} + L_{2\sigma}$
Mutual inductance M	$M = \sqrt{L_{1h} \cdot L_{2h}} = k \sqrt{L_{1T} \cdot L_{2T}}$	

The common flux ϕ_h is defined for each coil as the sum of the proper flux and the induced flux:

$$\phi_h = \phi_{h11} + \phi_{h12} = \phi_{h21} + \phi_{h22}$$

Each elementary flux defined above is proportional to its intensity source. Inductances of the system are proportionality coefficients between those quantities:

$$L_{1h} = \frac{\phi_{h11}}{I_1} \quad ; \quad L_{2h} = \frac{\phi_{h22}}{I_2}$$

$$L_{1\sigma} = \frac{\phi_{\sigma 1}}{I_1} \quad ; \quad L_{2\sigma} = \frac{\phi_{\sigma 2}}{I_2}$$

$$M = \frac{\phi_{h12}}{I_2} = \frac{\phi_{h21}}{I_1}$$

Equations of the real transformer are :

$$\begin{cases} U_1 = R_1 \cdot I_1 + p(\phi_{h11} + \phi_{h12} + \phi_{\sigma 1}) \\ U_2 = R_2 \cdot I_2 + p(\phi_{h22} + \phi_{h21} + \phi_{\sigma 2}) \end{cases}$$

$$(or) \quad \begin{cases} U_1 = R_1 \cdot I_1 + L_{1h} p \cdot I_1 + Mp \cdot I_2 + L_{1\sigma} p \cdot I_1 \\ U_2 = R_2 \cdot I_2 + L_{2h} p \cdot I_2 + Mp \cdot I_1 + L_{2\sigma} p \cdot I_2 \end{cases}$$

$$(or) \quad \begin{cases} U_1 = (R_1 + L_{1T} p) I_1 + Mp \cdot I_2 \\ U_2 = Mp \cdot I_1 + (R_2 + L_{2T} p) I_2 \end{cases}$$

One can make a real transformer appear in those equations by writing:

$$\begin{cases} U_1 = (R_1 + L_{1\sigma} p) I_1 + \tilde{U}_1 \\ U_2 = (R_2 + L_{2\sigma} p) I_2 + \tilde{U}_2 \\ \tilde{U}_1 = L_{1h} p \cdot I_1 + Mp \cdot I_2 \\ \tilde{U}_2 = L_{2h} p \cdot I_2 + Mp \cdot I_1 \end{cases}$$

Voltages \tilde{U}_1 et \tilde{U}_2 verify equation of turn ratio :

$$\frac{\tilde{U}_1}{\tilde{U}_2} = \frac{p \cdot \left(L_{1h} \cdot I_1 + \sqrt{L_{1h} \cdot L_{2h}} \cdot I_2 \right)}{p \cdot \left(L_{1h} \cdot L_{2h} \cdot I_1 + L_{2h} \cdot I_2 \right)} \sqrt{\frac{L_{1h}}{L_{2h}}} = \ddot{u}$$

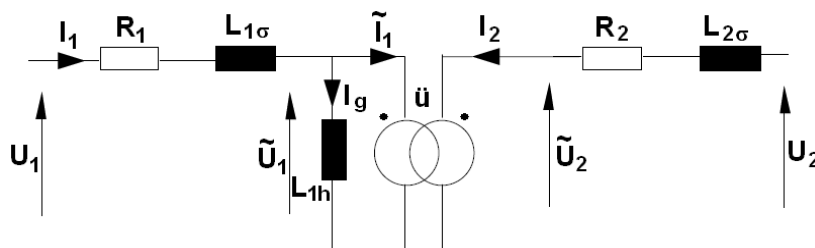
One can build $(\tilde{U}_1, \tilde{U}_2, \tilde{I}_1, I_2)$ so that the equations of ideal transformer are checked:

$$\tilde{I}_1 = -\frac{1}{\ddot{u}} \cdot I_2 = -\sqrt{\frac{L_{2h}}{L_{1h}}} \cdot I_2$$

The difference current between real input current I_1 and the input current of the ideal transformer \tilde{I}_1 is called magnetizing current $I_g = I_1 - \tilde{I}_1$. This magnetizing current corresponds to the current going through the proper inductance of primary coil L_{1h} when it is under voltage \tilde{U}_1 . Indeed, if Z_g is the impedance so that $\tilde{U}_1 = Z_g \cdot I_g$, one can find that it only depends on L_{1h} :

$$Z_g = \frac{\tilde{U}_1}{I_g} = \frac{p \cdot \left(L_{1h} \cdot I_1 + \sqrt{L_{1h} \cdot L_{2h}} \cdot I_2 \right)}{I_1 + \sqrt{\frac{L_{2h}}{L_{1h}}} \cdot I_2} = L_{1h} \cdot p$$

The real transformer can then be represented by :



The equivalent circuit to the real transformer